Hawke's Bay 3D Aquifer Mapping Project:
3D hydrogeological models from SkyTEM data in the Heretaunga Plains

HAWKE'S BAY
REGIONAL COUNCIL
TE KAUNIHERA Ā-ROHE O TE MATAU-A-MĀUI

Environmental Science

Hawke's Bay 3D Aquifer Mapping Project:
3D hydrogeological models from SkyTEM data in the Heretaunga Plains

Prepared By:

GNS Science

ZJ Rawlinson

For: Hawke's Bay Regional Council

Reviewed by:
S Harper, Hawke's Bay Regional Council
B Hemmings, GNS Science
RL Kellett, GNS Science
C Tschritter, GNS Science

.

Hawke's Bay 3D Aquifer Mapping Project:
3D hydrogeological models from SkyTEM data
in the Heretaunga Plains

ZJ Rawlinson

BIBLIOGRAPHIC REFERENCE

Rawlinson ZJ. 2023. Hawke's Bay 3D Aquifer Mapping Project: 3D hydrogeological models from SkyTEM data in the Heretaunga Plains. Wairakei (NZ): GNS Science. 69 p. Consultancy Report 2023/57.

CONTENTS

FIGURES

TABLES

EXECUTIVE SUMMARY

This report synthesises and analyses information from the previous Heretaunga Plains reports produced by the Hawke's Bay 3D Aquifer Mapping Project (3DAMP). The primary objective is to provide detailed 3D models and hydrogeological interpretations suitable to be utilised by subsequent numerical modelling and online visualisation tools. A further objective is to develop a refined understanding of near-surface permeability, which is relevant to groundwater-surface water interaction and aquifer confinement/vulnerability.

Previous information that this report synthesises includes: SkyTEM data, resistivity models, datasets collected during the drilling of 3DAMP_Well2, a data and model inventory report, a high-quality/deep borehole interpretation report, manual delineation of major hydrogeological units and automated hydrostratigraphic modelling. It is beyond the scope of this report to inspect small subsets of these data at the local scale. Here, the entire volume of data was assessed at the catchment scale, which necessitated a methodology that could handle the inspection of a large amount of data. In the future, local studies could refine models through closer interrogation and refinement of datasets for specific local applications.

A series of 3D models were developed using the same horizontal regular grid as the existing Heretaunga numerical groundwater model (that will be revised in a subsequent piece of work). The 3D models utilise 100 x 100 m grid cells horizontally and 2-m-thick grid cells vertically. The 3D models developed are as follows:

- An interpolated resistivity (res) model.
- A major Hydrogeological Unit (HU) model.
- A deterministic Hydrostratigraphic (HS) model.
- A resistivity facies (facies) model.
- An Aquifer Potential (AP) model.
- A Coarse fraction Classification model (CC).
- Horizontal Hydraulic Conductivity models (KH).

2D maps/models were also derived, primarily using the CC model:

- Aquifer thickness, separated into surficial, deep, total, and total as a percentage of unconsolidated thickness.
- Aquitard thickness, classified into unconfined, semi-confined and confined.
- Near-surface properties (res, CC and KH) for the upper 5 m, 10 m, 15 m, 20 m, 30 m and 50 m using the geometric and harmonic mean.
- Geometric and harmonic mean of horizontal hydraulic conductivity (KH) through the full vertical column of unconsolidated sediments and consolidated sediments where these outcrop at the surface.

3D model datasets were created and saved in an accessible .csv format, with x,y,z defining the centre of each grid cell. This format enables rapid model visualisation in an interactive online webmap and as 3D block models within a Leapfrog viewer file. A selection of these models was also converted to multi-band raster format, enabling further accessibility such as visualisation of elevation slices within GIS software. 2D models were developed in raster format, with some simplified to polygon shapefiles where appropriate. Due to the influence of salinity in the upper ~30 m near the coast, caution is needed when interpreting model data in this area. Datasets outlining the spatial extent of this area were also developed.

Simplifications of the 3D models to 2D maps assisted with investigating various aspects of the Heretaunga Plains aquifer system and with comparisons to previous investigations, highlighting the benefits of these datasets. Overall, the maps and models developed provide useful information to improve the understanding of the hydrogeological system in the Heretaunga Plains, support a greater understanding of other datasets (e.g. groundwater age and stream-flow gauging data) and could be used to guide additional data collection with greater precision.

The value of this information will be explored further through numerical groundwater model experiments in a subsequent piece of work in 3DAMP. These experiments aim to explore methods for utilisation of SkyTEM data to refine numerical groundwater models and consequences for predictive uncertainty.

This page left intentionally blank.

1.0   INTRODUCTION

This report synthesises and analyses information from the previous Heretaunga Plains reports produced by the Hawke's Bay 3D Aquifer Mapping Project (3DAMP). The primary objective is to provide detailed 3D models and hydrogeological interpretations suitable to be utilised by subsequent numerical modelling and online visualisation tools. A further objective is to develop a refined understanding of near-surface permeability, relevant to groundwater-surface water interaction and aquifer confinement/vulnerability.

3DAMP is a four-year initiative (2019–2023) jointly funded by the Provincial Growth Fund (PGF), Hawke's Bay Regional Council (HBRC) and GNS Science's (GNS) Groundwater Strategic Science Investment Fund (SSIF) research programme. The project applies SkyTEM technology to improve mapping and modelling of groundwater resources within the Heretaunga Plains, Ruataniwha Plains and Poukawa and Ōtāne basins. 3DAMP involves collaboration between HBRC, GNS and the Aarhus University HydroGeophysics Group (HGG).

Previous information that this report synthesises includes:

- SkyTEM data (SkyTEM Australia [2020]).
- SkyTEM-derived resistivity models (Rawlinson et al. 2021).
- Datasets collected during the drilling of 3DAMP_Well2 (Lawrence et al. 2021).
- A data and model inventory report (Tschritter et al. 2022).
- A high-quality/deep borehole interpretation report (Kellett et al. 2022).
- Manual delineation of major hydrogeological units (Sahoo et al. 2023).
- Automated hydrostratigraphic modelling (Foged 2022).

The final phase of the 3DAMP project will update the Heretaunga Plains groundwater numerical model (Heretaunga GW model) and the smaller Bridge Pa groundwater model (Bridge Pa GW model) that were developed as part of the GNS-led Te Whakaheke o Te Wai (TWOTW) Ministry of Business, Innovation & Employment (MBIE) Endeavour Programme.

1.1   Objectives

Hydrogeological interpretation of resistivity models is a process of translating resistivity values (typically represented by the unit ohm.m or Ω·m) to categorical or numerical values of more immediate use to a hydrogeologist. The numerical values present in a resistivity model are a function of complex relationships between porosity, permeability, grain size and sorting, mineralogical content such as clay, and fluid properties. Supporting local information is therefore required to interpret the resistivity models. The objectives of this report include both dataset creation and assessments related to hydrogeological interpretation within the Heretaunga model area (Figure 1.1) as follows:

- Develop datasets suitable for display within an online 3D model visualisation tool.
- Develop datasets suitable for use within numerical groundwater models.
- Develop datasets that describe near-surface permeability, which is relevant to groundwater–surface water interaction and aquifer confinement/vulnerability.
- Develop hydraulic property information relevant for numerical groundwater modelling implementation.
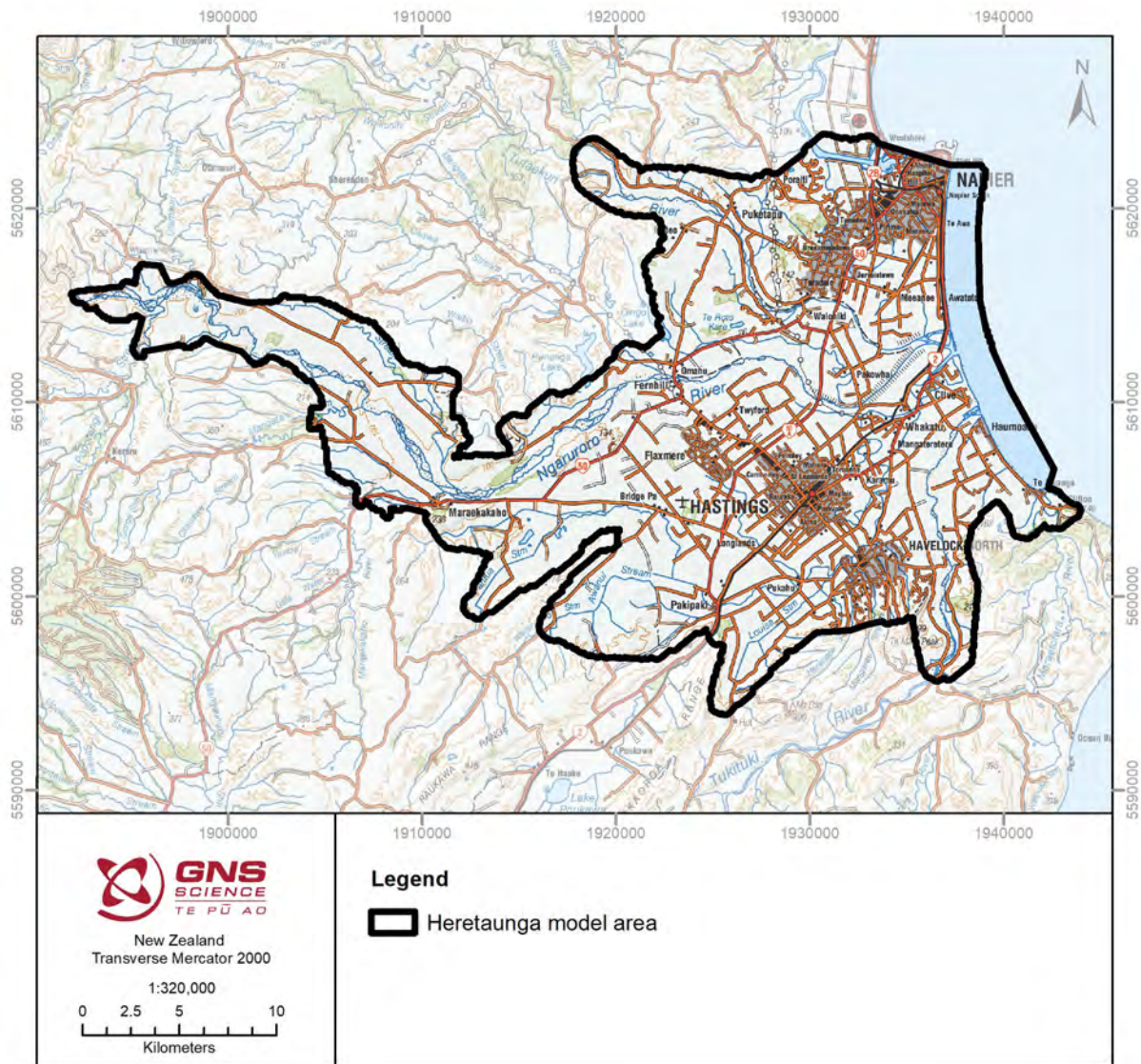
Figure 1.1   Location map of the Heretaunga Plains showing the extent of the Heretaunga model area (combined extent of the current Heretaunga Plains numerical groundwater model [Rakowski and Knowling 2018] and 300 m buffers around each SkyTEM-derived 1D resistivity model).

2.0   METHOD

The resistivity models (Rawlinson et al. 2021) consist of a large amount of data: greater than 1.5 million data points in each resistivity model. It is beyond the scope of this report to inspect small subsets of these data at the local scale. Here, the entire volume of data is assessed at the catchment scale, which necessitates a methodology that can handle the inspection of a large amount of data.

To manage the assessment of this amount of data, as well as the relatively sparse supporting datasets, a combined approach of manual and automated methods for interpretation was utilised. In previous work, Kellett et al. (2022) and Sahoo et al. (2023) largely utilised manual methodologies of interpretation, while Foged (2022) utilised a largely automated approach. This section describes how these previous pieces of work have been combined into 3D and 2D datasets that can then be used in various hydrogeological applications.

2.1   3D-Gridded Model Development

In this section, 3D models suitable for numerical groundwater modelling and online visualisation were developed.

The resistivity model datasets developed by Rawlinson et al. (2021) are 1D models at SkyTEM data locations (Figure 2.1). These datasets are essentially point datasets that include gaps where electromagnetic noise was removed and where the helicopter was unable to fly due to flight path restrictions.

The TWOTW Heretaunga GW model has a bottom left node location of 1891460 Easting, 5594000 Northing (the same as the previous Heretaunga numerical groundwater model developed by Rakowski and Knowling [2018]) and a horizontal grid cell resolution of 100 m. Cell centres are used to store data properties. 3D-gridded datasets were developed to map directly to these cell centre locations (Figure 2.2).

Throughout the below methodology, the previous data and model inventory report and associated datasets (Tschritter et al. 2022), e.g. borehole lithological information, water levels and previous conceptual understanding and models, were used extensively to guide 3D and 2D model development. In Section 3, results are displayed along cross-sections also utilised by Kellett et al. (2022) and Sahoo et al. (2023) (Figure 2.1).
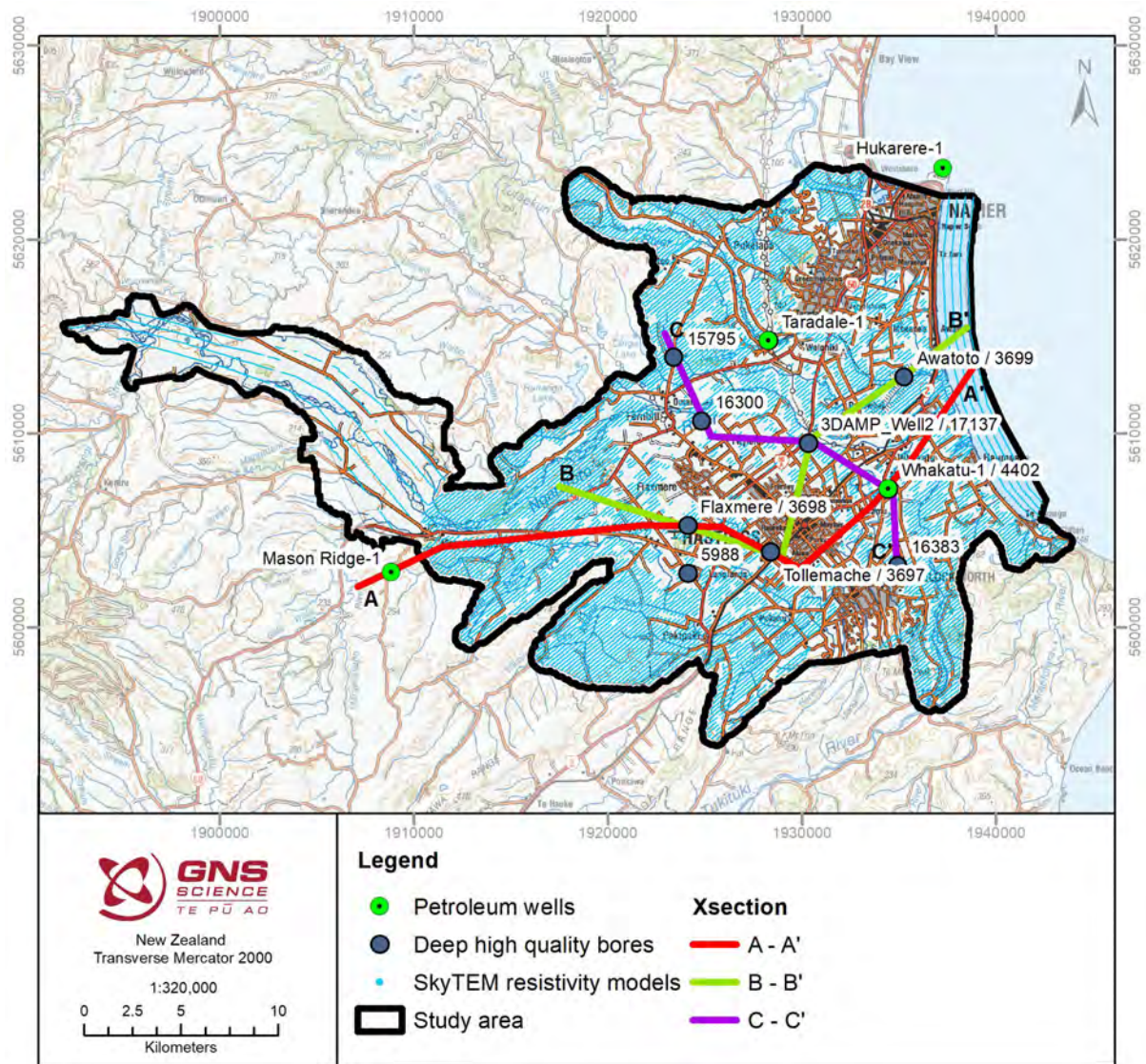
Figure 2.1   Location of SkyTEM-derived 1D resistivity models in the Heretaunga Plains. Also shown are deep wells with high-quality lithological logs through which cross-sections were prepared to display results. Cross-section locations match those utilised by Kellett et al. (2022) and Sahoo et al. (2023).
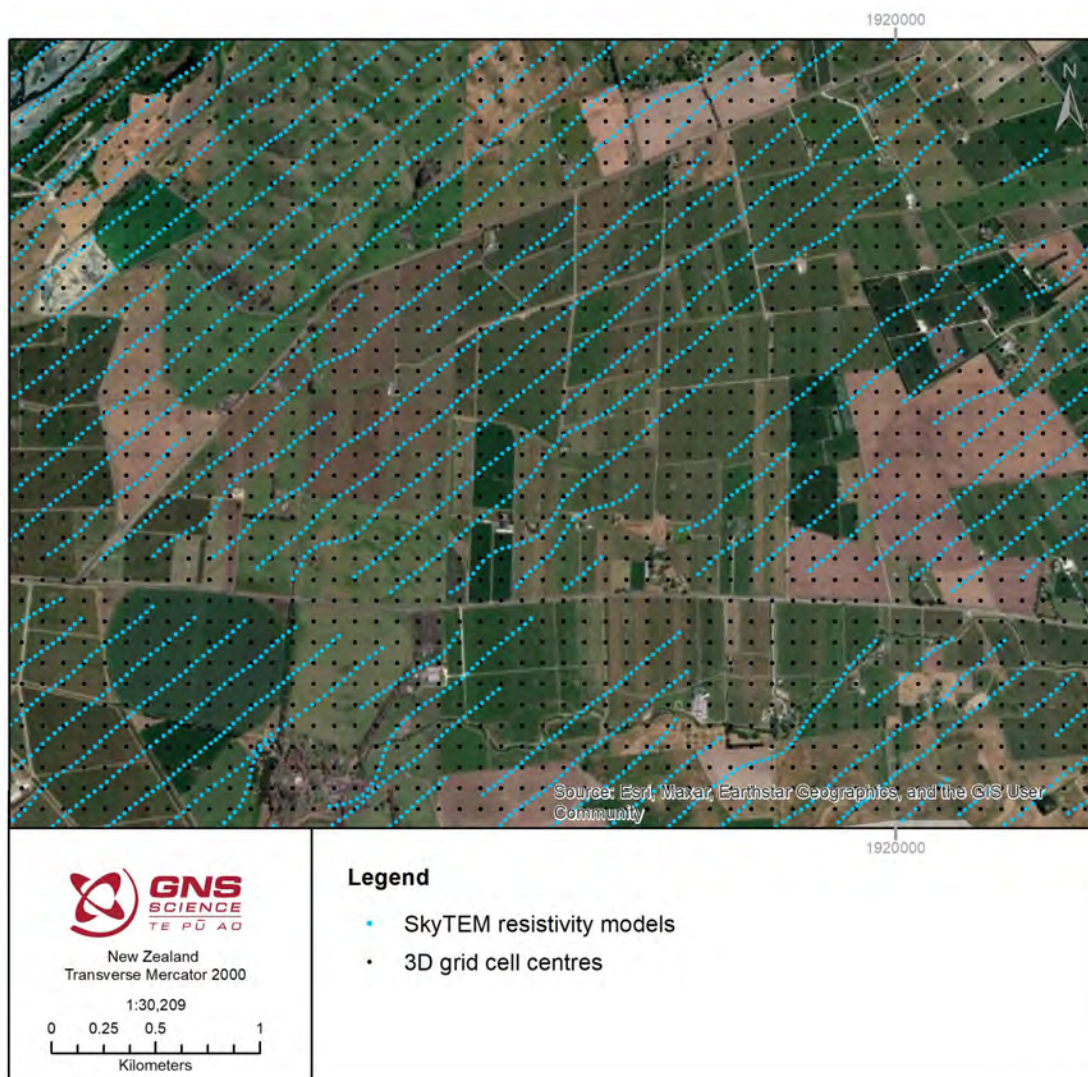
Figure 2.2   Small section of the Heretaunga model area showing the difference between the original SkyTEM resistivity model locations along flight lines and the 3D uniformly gridded model locations (100 m horizontal resolution).

2.1.1   Interpolated Resistivity (res) Model

To develop a more continuous 3D dataset, interpolation of the resistivity values to a uniform 3D grid was undertaken using Geoscene3D software (https://geoscene3d.com/).

Historical resistivity data provided valuable information in some of the gaps within the SkyTEM data (Figure 2.3; Tschritter et al. 2022). Additionally, the offshore and onshore portions of the SkyTEM survey were inverted separately and generated as independent datasets (Rawlinson et al. 2021).

As multiple datasets are not able to be combined during interpolation within Geoscene3D software, the 1D layered resistivity model datasets were combined by re-sampling them a x,y,z locations with a maximum of 5 m vertical separation between x,y,z points (i.e. re-sampling thicker layers) and exporting the combined dataset as a single *.csv* file. Where depth of investigation (DOI[1]) calculations were available (e.g. Figure 2.4), data below 'DOI_Standard'

---

1   For each resistivity model, DOI was previously estimated. The DOI calculation takes into account the SkyTEM system transfer function, the number of data points, the data uncertainty and the resistivity model. Resistivity structures below the DOI standard value are very weakly determined by the data (Rawlinson et al. 2021).

were not included in this combined dataset. This ensures that resistivity data with higher uncertainty values are not used for the interpolation. The following datasets were combined (described further within Tschritter et al. [2022]):

- SkyTEM (airborne Time-domain ElectroMagnetic) data:
    - *Heretaunga_smooth_resistivitymodel_V1_2021_inv.xyz*
    - *Heretaunga_offshore_smooth_resistivitymodel_V1_2021_inv.xyz*

- GroundTEM (Ground-based Time-domain ElectroMagnetic) data. Where both were present, the NanoTEM and TEM results were merged into a single 1D sounding, preferentially using the NanoTEM results in the upper 50 m.
    - *Heretaunga_TEM_Sites_Smooth.xyz*
    - *Heretaunga_NTEM_Sites_Smooth.xyz*

- Direct current (DC) resistivity data (no DOI calculations available):
    - *Risk_1974_Models.xyz*
    - *Borgesius_1975_Models.xyz*
    - *Hawkins_1978_Models.xyz*

- Electrical resistivity tomography (ERT) data:
    - *Bridge_Pa_ERT_Model_1_inv.xyz*
    - *Morton_Estate_ERT_Model_2_inv.xyz*
    - *Paritua_Estate_ERT_Model_3_inv.xyz*

Smooth models were chosen for this combination, as they were available for the majority of the datasets (only SkyTEM and GroundTEM datasets have sharp resistivity models) and provide finer detail than the sharp models.[2]

These data were imported as a point dataset into Geoscene3D. This point dataset shows a roughly Gaussian distribution when transformed into $\log_{10}$ space (Figure 2.5), so Kriging was selected as appropriate for interpolation. Kriging also provides a corresponding 3D grid with an interpolation uncertainty estimate (the kriging variance), which could be utilised within subsequent applications such as numerical groundwater modelling.

A uniform 3D grid was defined with 100 x 100 m horizontal resolution and 2 m vertical resolution (cell thickness), matching the extents of the resistivity data and the Heretaunga GW model (Table 2.1). The large memory footprint of the dataset prevented generation of a finer-resolution 3D grid at this full extent.

Geoscene3D software uses the GSLIB kriging library. Interpolation was undertaken on the $\log_{10}$ transformed resistivity data. A number of tests were performed on various smaller selections of data to check for the most appropriate kriging variables. Point Kriging was

---

2 A smooth model is a many-layered model that uses a fixed layer structure (logarithmically increasing layer thicknesses), and the resistivity of each layer is solved for. The smooth regularisation scheme penalises the resistivity changes, resulting in the smoothest resistivity transitions both vertically and horizontally. A sharp model uses the same model discretisation as the smooth model, but the model regularisation scheme is different. The sharp model regularisation scheme penalises the number of resistivity changes above a certain size, instead of the absolute resistivity changes (as in the smooth model regularisation scheme). The sharp model regularisation scheme therefore results in a model with few, but relatively sharp, resistivity transitions. This allows for relative abrupt changes in resistivities, while using the fixed layer thicknesses of the smooth model (e.g. Rawlinson et al. 2021).

undertaken using a spherical function, sill of 0.1 and range of 2000 m. A 500 m horizontal search radius, 25 m vertical search radius and maximum of six data points in each octant were used. The horizontal and vertical search radii used impact the final coverage of the dataset.

Once interpolation was completed, null values were assigned to grid nodes outside the Heretaunga model area and above the Digital Elevation Model (DEM) (25 m resolution, as utilised within Sahoo et al. [2023]). The gridded resistivity model was exported as a *.csv* file, which consists of resistivity values mapped to cell nodes *X, Y, Z* and *res*. The kriging variance gridded model was similarly exported to a *.csv* file, including the following: *X, Y, Z, resvar*.
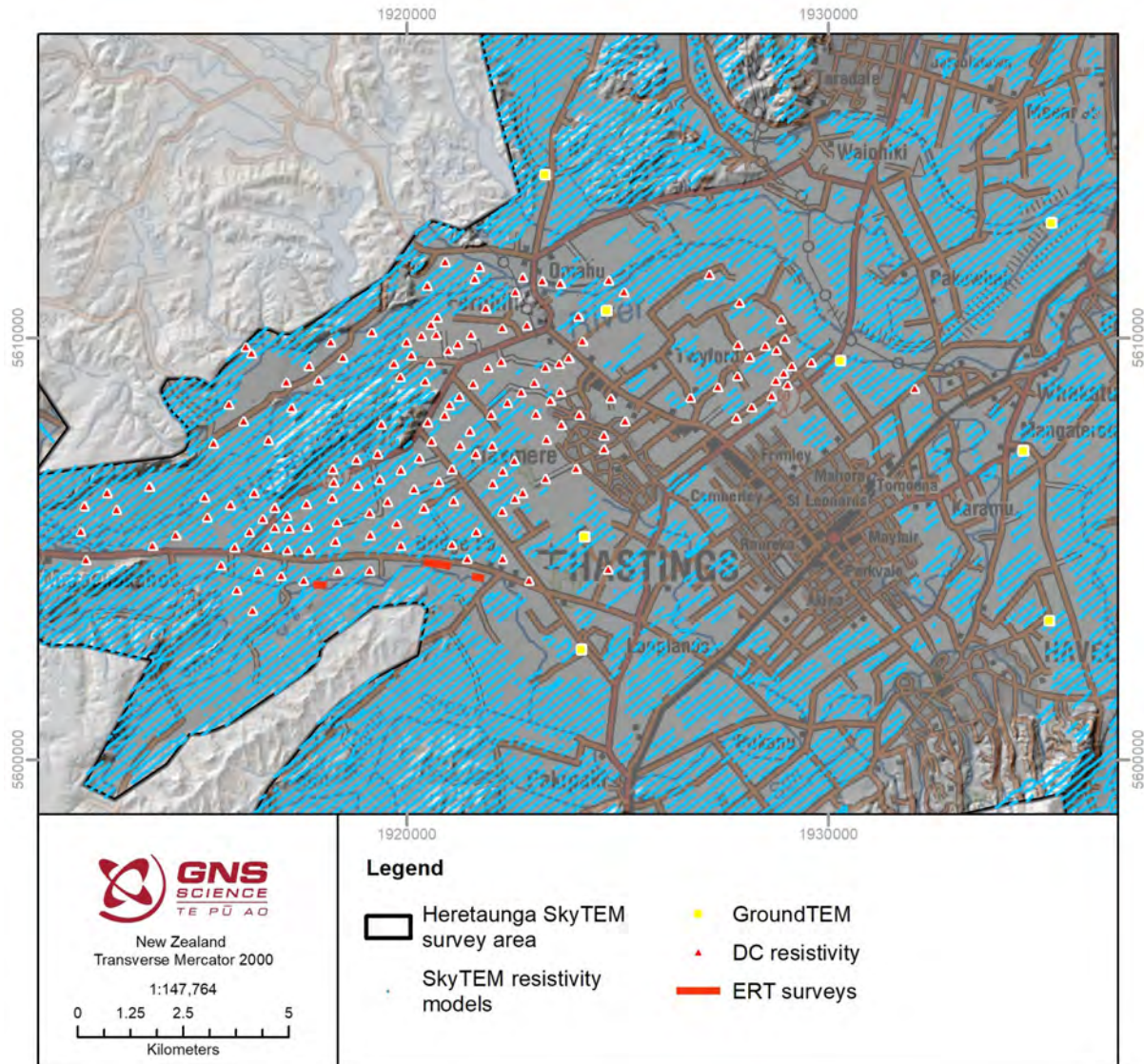
Figure 2.3   Ground-based resistivity data included within the combined resistivity dataset – some historic data is available within SkyTEM data gaps.
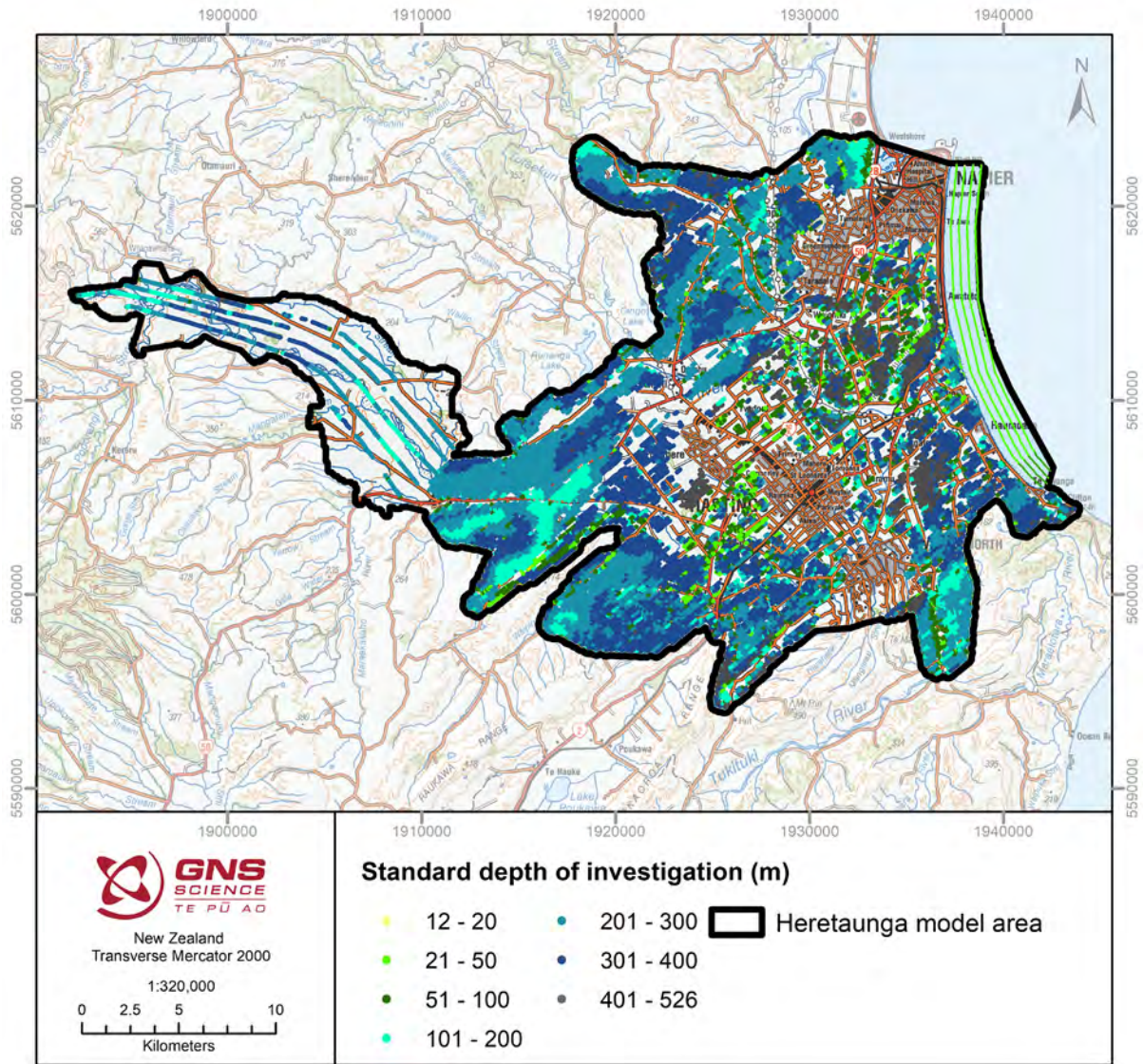
Figure 2.4   Standard depth of investigation for the SkyTEM-derived smooth resistivity models.

Table 2.1   Three-dimensional grid generated in Geoscene3D Software (data mapped to cell nodes) to match the Heretaunga GW model extents (data mapped to cell centres).

Corner Node Coordinates	Minimum	Maximum	Node Count	Width (m)	Node Spacing (m)
X	1891510	1944110	527	52,600	100
Y	5594050	5624550	306	30,500	100
Z	-594	286	441	880	2
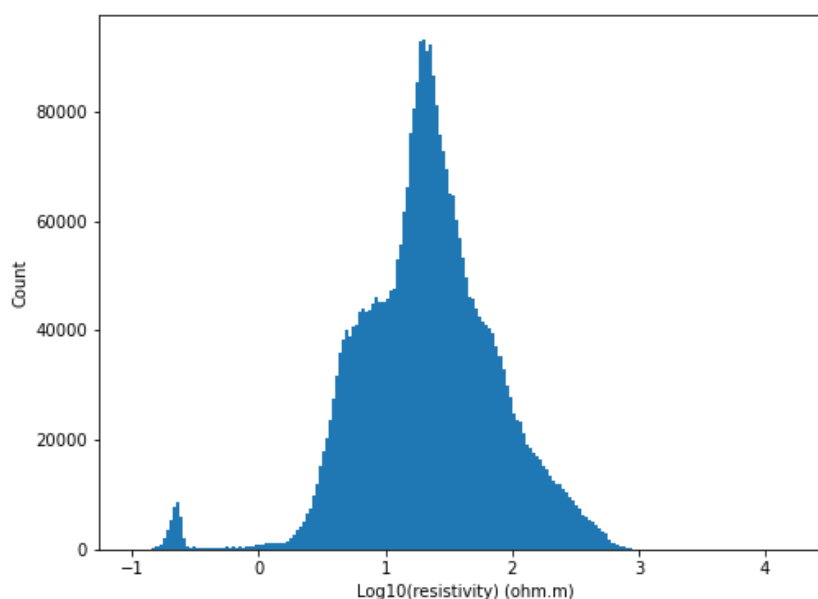
Figure 2.5   Histogram with 200 bins showing the $\log_{10}$(resistivity) values from the point dataset. The distribution approximates a Gaussian distribution.

2.1.2   Major Hydrogeological Unit (HU) Model

Manually delineated major hydrogeological unit (HU) surfaces from Sahoo et al. (2023) were imported into Geoscene3D software (see Sahoo et al. [2023] for further details about these). To create a matching grid to the resistivity grid in Section 2.1.1, the 'Single Floating Point Type' 3D grid created in Section 2.1 was adjusted to a 'Word Discrete Value' type grid using the 'Convert Grid Value Type' in the Toolbox in Geoscene3D software, and four material categories were defined: HU1, HU2, HU3 and HU4. Geoscene3D stores information at cell node locations.

Hydrogeological units were assigned to the 3D grid (Table 2.2) using the manually delineated surfaces via the following steps:

- Assign null to all nodes.
- Assign HU4 to all nodes below HU4 top surface.
- Assign HU3 to all nodes above HU4 top surface and below HU2 bottom surface.
- Assign HU2 to all nodes above HU2 bottom surface and below DEM.
- Assign HU1 to all nodes above HU1 bottom surface and below DEM.
- Assign null to all nodes outside the Heretaunga model boundary.

The gridded HU model was exported as a *.csv* file where values are mapped to cell nodes *x, y, z* and *HU*. Due to some discrepancies between cell resolution and surface resolutions, a few isolated single cells of HU2 were mapped at the surface within other unit areas. To remove these, an additional Python script was utilised to re-map cells classified as HU2 to the underlying unit where a single cell of HU2 was located at the maximum *Z* value and surrounded by HU3 or HU4.

The exported hydrogeological unit and resistivity 3D grid files were combined into a single dataset (combined dataset), and, to assist with later calculations, the elevation (*Z*) of the top model cell mapped with HU values was also determined (top_elev_HU). The dataset now has the columns *X, Y, Z, top_elev_HU, res, resvar* and *HU*. Due to the defined 3D grid (Table 2.1), this combined dataset has information mapped to the equivalent x,y locations

as the Heretaunga GW model cell centres. Because the HU model utilised continuous surfaces throughout the entire model area, some locations that have gaps in the res model have values for the HU model (Table 2.2).

Table 2.2   Definition of the Hydrogeological Unit (HU) model.

Hydrogeological Unit (from Sahoo et al. [2023])	HU Model	Description
HU1	1	Confining unit
HU2	2	Shallow aquifer unit
HU3	3	Deep aquifer unit
HU4	4	Basement unit

2.1.3   Deterministic Hydrostratigraphic (HS) Model

Accumulated clay thickness (ACT) models were previously developed (Foged 2022) at locations of SkyTEM-derived resistivity models and borehole lithological information. The methodology combines information from lithological logs with the SkyTEM-derived resistivity models and allows for a variable spatial relationship between these. Because the methodology utilised is only valid within unconsolidated sediments, the base was set at the shallower of either -360 mASL (metres above sea level) or a preliminary basement surface minus 60 m (Sahoo et al. 2023). The additional 60 m depth was added to account for uncertainty due to a preliminary basement surface (preliminary top HU4) being utilised for the work. The method is also not valid where groundwater is too saline, so a selection of resistivity models considered to be saltwater-influenced were excluded from the modelling (Figure 2.6). The ACT modelling (Foged 2022) used the sharp resistivity model and so captures relevant information from that resistivity model for sharp boundary changes.

Clustering of the ACT results (Figure 2.7) was used to create a training image, after which direct sampling multi-point statistical methods were used to generate 500 hydrostratigraphic model realisations filling a 3D model grid, with the most variability observed within resistivity data gaps (Foged 2022). The direct sampling realisations were generated based on conditional geostatistical information that was obtained by scanning the training image. The 500 realisations were generated on a uniform 3D grid with a bottom left node 1891850 Easting, 5593750 Northing, cell size 100 m and cell thickness 10 m (different horizontal cell centre locations compared to the Heretaunga GW model, and different cell thickness to the 3D models developed in this report). Each cell node was assigned a cluster number of 0, 1, 2, 3 or 4. Here, 0 is the most permeable material and 4 is the least permeable material. Clusters 0 and 1 correspond to <30% clay fraction; clusters 3 and 4 correspond to >70% clay fraction; and cluster 2 is a broad transitional group, ranging from 30 to 70% clay fraction (Figure 2.7). Only 10% of the input data fall into the transitional cluster 2 group (Figure 2.7).

To generate a deterministic hydrostratigraphic (HS) model from these 500 realisations, all 500 values within each grid cell were assessed and classified based on the values of 95% of the models (≥475 values; Table 2.3) to create classes 0–6, where now: 0 is unknown (0–100% clay), 1–3 are >50% clay and 4–6 are <50% clay. Clay-fraction percentage estimates above and in Table 2.3 were made using the clay-fraction graphs relevant to the data selected for the training image (Figure 2.7; Foged 2022). Figure 2.7b supports the assumption made in the HS model (e.g. Table 2.3) that cluster 2 can effectively be split into two, providing groups representing >50% clay fraction and <50% clay fraction. These classes 0–6 were exported to a *.csv* file with values mapped to the Foged (2022) cell nodes: *X, Y, Z, HS_unclipped.*

To map these data from the Foged (2022) cell nodes to the combined model cell centres (Sections 2.1.1 and 2.1.2), a block model was created in Geoscience Analyst (which exports data from cell centres) with the same dimensions as the Heretaunga GW model (Table 2.4). The *X*, *Y*, *Z*, *HS_unclipped* node dataset was imported as a point dataset and transferred to the block model using the nearest neighbour function from Scipy.spatial.cKDTree (Maneewongvatana and Mount 2002; Virtanen et al. 2020). This method works for categorical (referenced) data such as these. This block model was exported as a *.csv* file with columns *X*, *Y*, *Z* and *HS_unclipped*, where *X*, *Y*, *Z* now corresponds to the same cell centres as the combined dataset.

This dataset was joined at *X*, *Y* and *Z* locations to the combined dataset. Because the ACT methodology is only valid within the unconsolidated sediments, an additional join was made to the combined dataset where HU is not basement (HU <4) to create the HS model. The combined dataset now has columns *X*, *Y*, *Z*, *top_elev_HU*, *res*, *resvar*, *HU*, *HS_unclipped* and *HS*.
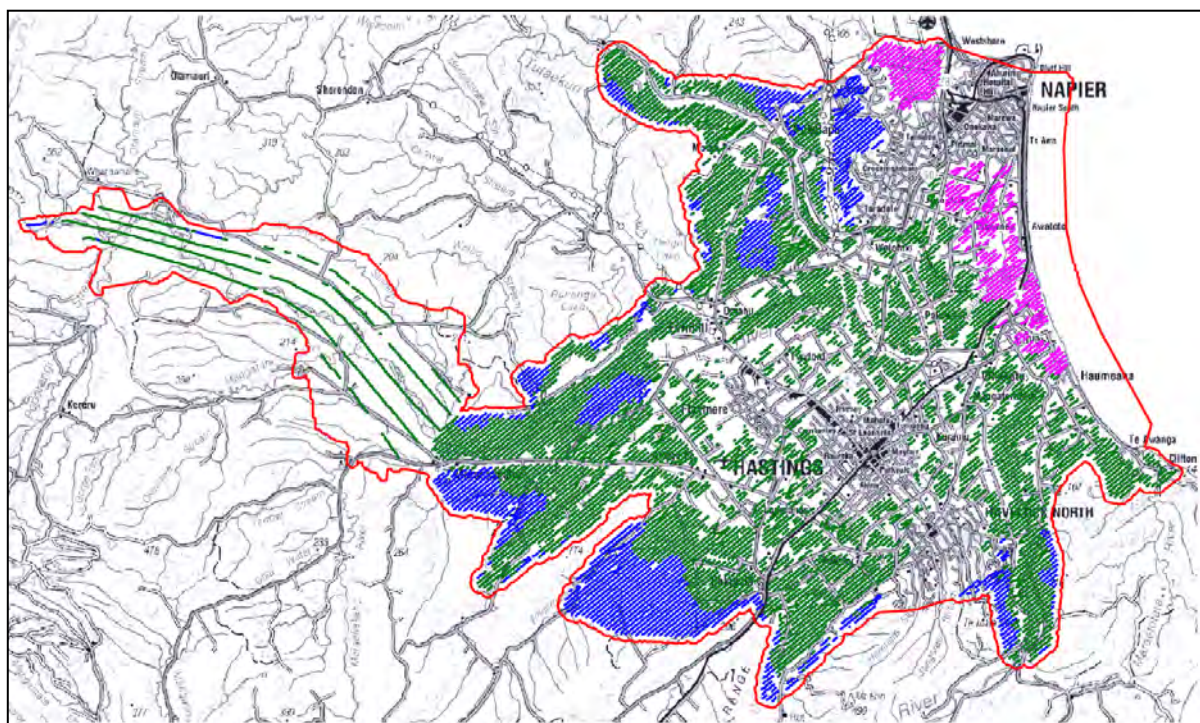
Figure 2.6   Accumulated clay thickness (ACT) model area (red line). Green dots mark the SkyTEM resistivity model locations utilised within the ACT; magenta dots mark resistivity model locations excluded from the ACT due to significant saltwater influence; blue dots mark resistivity model locations excluded from the ACT due to basement influence. Figure and caption from Foged (2022).

Table 2.3   Conversion of Foged (2022) cluster numbers 0–4 from 500 realisations into a unique (deterministic) Hydrostratigraphic (HS) model that represents the 95% likelihood model. Permeability is estimated from Figure 2.7.

Cluster Number(s) (Count of ≥475)	HS Model	Permeability	Percentage of HS Cells (%)
0	6	High: <20% clay	14.111
0 and 1	5	High: <30% clay	23.160
0 and 1 and 2 (and not 4 and 3 and 2)	4	High to medium: <50% clay	14.833
4 and 3 and 2 (and not 0 and 1 and 2)	3	Low to medium: >50% clay	20.835
4 and 3	2	Low: >70% clay	25.940
4	1	Low: >80% clay	1.120
(0 and 1 and 2 and 3) or (1 and 2 and 3 and 4) or (0 and 1 and 2 and 3 and 4)	0	Unknown: 0–100% clay	0.001
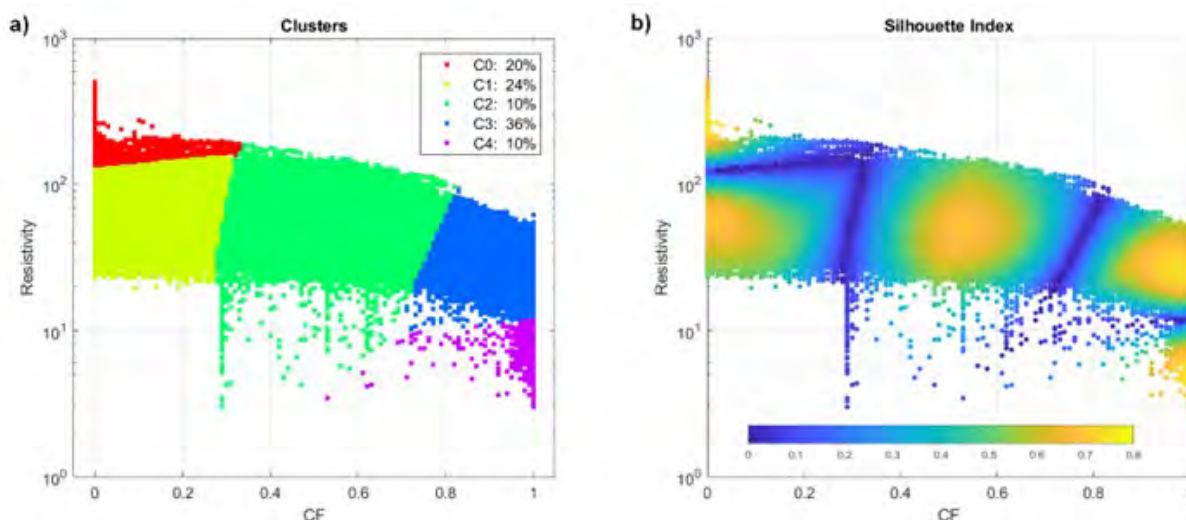
Figure 2.7   Five accumulated clay thickness (ACT) clusters. (a) input clay fraction (CF) and resistivity data (x,y axis) and the resulting cluster group (dot colour); (b) corresponding silhouette index. The silhouette index is a measure of how similar an object is to its own cluster (cohesion) compared to other clusters (separation). Only data with a silhouette index >0.58 were used as hard data to generate a training image for the direct sampling (geostatistical) simulations. Figure from Foged (2022).

Table 2.4   Three-dimensional grid generated in Geoscience Analyst software (data mapped to cell centres) to match the Heretaunga GW model extents (data mapped to cell centres).

Corner Node Coordinates	Minimum	Maximum	Number of Cells	Grid Size (m)	Cell Size (m)
X	1891460	1944160	527	52,700	100
Y	5594000	5624600	306	30,600	100
Z	-361	287	324	648	2

2.1.4 Resistivity Facies (facies) Model

As significant changes within resistivity are best assessed on a logarithmic scale, resistivity facies were defined by separating the res model into 14 resistivity facies classes (facies) uniformly separated on a log scale (Table 2.5; for example, Minsley et al. [2021]). These facies group materials are expected to have similar hydrologic and geologic properties based on their resistivity to assist with easier discrimination of significant variability and similarity.

Log_{10}-transformed res model values were classified into uniform bins with a width of 0.15 between 0.9 and 2.7 (Table 2.5). These values were chosen based on detailed assessments of resistivity values against relevant datasets described within Tschritter et al. (2022), such as lithological logs, as well as assessments provided in Kellett et al. (2022), Sahoo et al. (2023) and Foged (2022).

Resistivity values in the *res* column (interpolated resistivity model from Section 2.1.1) were converted to resistivity facies classes using the combined dataset, which now has columns *X, Y, Z, top_elev_HU, res, resvar, HU, HS_unclipped, HS* and *facies*.

Table 2.5   Resistivity facies (facies) model definition, using resistivity values within the res model.

Facies	Lower-Bound Log_{10}(res)	Upper-Bound Log_{10}(res)	Lower-Bound res Model (ohm.m)	Upper-Bound res Model (ohm.m)
1	N/A	0.90	N/A	8
2	0.90	1.05	8	11
3	1.05	1.20	11	16
4	1.20	1.35	16	22
5	1.35	1.50	22	32
6	1.50	1.65	32	45
7	1.65	1.80	45	63
8	1.80	1.95	63	89
9	1.95	2.10	89	126
10	2.10	2.25	126	178
11	2.25	2.40	178	251
12	2.40	2.55	251	355
13	2.55	2.70	355	501
14	2.70	N/A	501	N/A

2.1.5 Aquifer Potential (AP) Model

An Aquifer Potential (AP) model was developed to separate the facies model into consolidated and unconsolidated sediments, while providing an indicator of the likelihood of each model cell to host aquifer-bearing material. AP classes were defined by establishing rules within the major hydrogeological units as to how each resistivity facies class maps to aquifer potential. The naming 'aquifer potential' refers to the likelihood that a particular cell may host aquifer-bearing material.

The primary mapping of facies to aquifer potential was undertaken by first defining resistivity thresholds upon which low, medium and high aquifer potential were defined. This separates the dataset into a simplified text category with six classes 'aq', mapping values to consolidated low, medium and high aquifer potential and unconsolidated low, medium and high aquifer potential. Threshold values were chosen based on detailed assessments of resistivity against relevant datasets described within Tschritter et al. (2022), such as lithological logs and QMAP main rock type, as well as assessments provided in Kellett et al. (2022), Sahoo et al. (2023) and Foged (2022).

The unconsolidated sediments (HU=1–3) were observed to follow a linear relationship between resistivity and aquifer potential (as expected). Unconsolidated medium and high aquifer potential thresholds were set at 45 and 89 ohm.m, respectively, which coincide with the facies upper boundaries of classes 6 and 8. Therefore, for unconsolidated sediments, facies classes 1–6 are defined as low aquifer potential, classes 7–8 are defined as medium aquifer potential and classes 9–14 are classified as high aquifer potential. Due to the linear relationship observed, aquifer potential in the unconsolidated sediments is expected to gradually increase as the facies classes increase in value. To develop unique aquifer potential classes, these 14 facies classes within unconsolidated sediments (HU = 1 − 3) were mapped to the aquifer potential numbers 15–28 (Table 2.6).

For consolidated sediments (HU = 4; corresponding in this area to mudstone/siltstone, sandstone and limestone), the relationship is not completely linear due to the relationship between resistivity and types of limestone, from a more massive limestone to a more sandstone- and mudstone-dominated limestone. Limestone is assumed to have a mostly linear relationship with resistivity, with more massive (consolidated) limestone having higher resistivity and more permeable limestone having lower resistivity. However, there is a complication in that lower resistivity corresponds to more porous and/or more silt, while higher resistivity corresponds to more massive and/or less silt, as well as to outcropping limestone. Due to this relationship, three threshold values were required – two threshold values for splitting into medium and high potential and an additional threshold at a high resistivity value for splitting into low potential again. Thresholds for splitting into low, medium and high aquifer potential were defined at values of 22 and 45 ohm.m, and then an upper threshold of 126 ohm.m was selected above which limestone becomes too tight and aquifer potential drops. Therefore, for consolidated sediments, facies classes 1–4 and 10–14 are defined as low aquifer potential, classes 5–6 are defined as medium aquifer potential and classes 7–9 are classified as high aquifer potential. These were mapped in order from low to high to the aquifer potential numbers 1–14 (Table 2.6).

These consolidated threshold values are consistent with the values for limestone utilised within the Poukawa SkyTEM interpretation report (Rawlinson et al., in prep.), which had a higher volume of limestone material available for analysis. These threshold values also considered the comparison of available mudstone and sandstone information against resistivity values in the area, with low aquifer potential being consistent with containing <10% limestone and high aquifer potential being consistent with containing <10% mudstone. Information on sandstone is somewhat limited and variable between QMAP and borehole information. QMAP information places sandstone in the low to medium aquifer potential range, while borehole information spans the full low to high aquifer potential range.

Using the above approach, aquifer potential classes 1–28 were defined using the combined columns *facies* and *HU*. This calculation was made on the combined dataset, which now has columns *X, Y, Z, top_elev_HU, res, resvar, HU, HS_unclipped, HS, facies, AP* and *aq*.

Table 2.6   Aquifer Potential (AP) model definition, which uses the defined resistivity facies (facies) classes from Table 2.5 and the major hydrogeological unit (HU) classes from Table 2.2. Also defined is a simplified aquifer potential model with only six classes 'aq' and 'aqname'.

AP	HU	Facies	aq	aqname	Lower-Bound Resistivity (ohm.m)	Upper-Bound Resistivity (ohm.m)
1	4	1	cl	Consolidated-low	N/A	8
2	4	2	cl	Consolidated-low	8	11
3	4	3	cl	Consolidated-low	11	16
4	4	4	cl	Consolidated-low	16	22
5	4	10	cl	Consolidated-low	126	178
6	4	11	cl	Consolidated-low	178	251
7	4	12	cl	Consolidated-low	251	355
8	4	13	cl	Consolidated-low	355	501
9	4	14	cl	Consolidated-low	501	5000
10	4	5	cm	Consolidated-med	22	32
11	4	6	cm	Consolidated-med	32	45
12	4	7	ch	Consolidated-high	45	63
13	4	8	ch	Consolidated-high	63	89
14	4	9	ch	Consolidated-high	89	126
15	1–3	1	ul	Unconsolidated-low	1	8
16	1–3	2	ul	Unconsolidated-low	8	11
17	1–3	3	ul	Unconsolidated-low	11	16
18	1–3	4	ul	Unconsolidated-low	16	22
19	1–3	5	ul	Unconsolidated-low	22	32
20	1–3	6	ul	Unconsolidated-low	32	45
21	1–3	7	um	Unconsolidated-med	45	63
22	1–3	8	um	Unconsolidated-med	63	89
23	1–3	9	uh	Unconsolidated-high	89	126
24	1–3	10	uh	Unconsolidated-high	126	178
25	1–3	11	uh	Unconsolidated-high	178	251
26	1–3	12	uh	Unconsolidated-high	251	355
27	1–3	13	uh	Unconsolidated-high	355	501
28	1–3	14	uh	Unconsolidated-high	501	N/A

2.1.6 Coarse-Fraction Classification (CC) Model

A coarse-fraction classification (CC) model was developed for the following three reasons:

1. **Subtle borehole variations are not effectively picked up by the HS model.**

   Upon assessment of the HS model against borehole lithological log data and during exploration of the 2D map products (see Section 2.2), it was ascertained that, although the HS model provides good estimates of mean properties as intended, the 10 m vertical resolution results in some smaller pathways being masked that are identified by the AP model. Additionally, the HS model utilised the sharp resistivity model, which may neglect some more subtle variations, particularly in the near surface. This was particularly notable in a few select areas where, for example, the depositional environment results in highly re-worked material and small-scale heterogeneity (explored further in the 2D maps in Section 2.2). In these areas, lithological logs identify thin permeable material surrounded by more impermeable material: for example, gravel <5 m thick, surrounded above and below by clay, or thicker mixtures of silt and sand with thin gravel lenses. Manual inspections demonstrated that these locations were typically corresponding to an AP model class of 21 (medium aquifer potential; facies class of 7 within unconsolidated material) and an HS model class of 3 (>50% clay). Additionally, an AP model class of 21 has a lower bound of 45 ohm.m, and sample resistivity measurements compared to grain-size analyses from 3DAMP_Well2 (Lawrence et al. 2021) confirmed that all samples with >50% fine-grained material have resistivity values less than 45 ohm.m (Figure 2.8). The resistivity of water samples taken at 3DAMP_Well2 had a mean value of 48 ohm.m, which is also the mean resistivity from all water samples available in the study area (Tschritter et al. 2022; range of 14–85 ohm.m), so resistivity values <48 ohm.m indicate that clay is influencing the bulk resistivity.

2. **Different spatial-coverage limitations of the HS and AP models.**

   The HS model utilises borehole information and a spatially varying function that maps the relationship between resistivity and permeability (clay fraction). The AP model is a more simplistic model that does not provide a spatially varying translator function; however, it is also able to provide some more information on consolidated sediments and some locations of ambiguity (such as the offshore dataset, which was excluded from the HS model). Meanwhile, the AP model has gaps over towns such as Hastings, whereas the geostatistical simulations forming the HS model were able to fill these data gaps.

   The Heretaunga GW model being developed requires information to be provided even within basement areas of the model to, for example, better consider flux from limestone. As the HS model does not provide information on the consolidated geology, while the AP model does not provide information beneath towns, a combination between the AP and HS models is required to provide best information to the Heretaunga GW model. The Heretaunga GW model may utilise the separate AP model for the consolidated sediments and the 500 original hydrostratigraphic realisations for the unconsolidated area (Foged 2022); however, as different methodological inclusions of SkyTEM-derived models to refine the Heretaunga GW model are being explored, a deterministic combination of the AP and HS models is also desirable.

3. Different resistivity models used by the HS and facies/AP models.

Because the HS model utilised the sharp resistivity model and the facies utilised the smooth resistivity model (apart from the basement clipping, which utilised manual interpretation of both models), comparison between the two can provide greater certainty on locations of high versus low resistivity.

To combine the strengths of the AP and HS models and assist with eliminating weaknesses, a final dataset was created – the CC model – that combines these models (Equation 2.1). In order to generate a model that highlighted the mixed areas (identified above in reason 1), where properties may vary between those of aquitard and aquifer, a weighting function was applied. Due to the nature of the AP model numbers (unconsolidated sediments in classes 15–28), the facies class numbers (1–14) were used for the calculation of Equation 2.1, but only within the unconsolidated sediments (HU <4). The weighting function was designed to promote any areas that had a HS of 3 and an aquifer potential of 21 ($facies = 7$) to a higher permeability than HS 3. As such, the HS model was normalised ($\frac{HS}{6}$) and the facies model divided by six ($\frac{facies}{6}$), effectively upweighting $facies \geq 7$.

For example, where $facies = 7$, this changes HS 3, normalised to 0.5, now weighted by the AP model to 0.58 (Table 2.7; Equation 2.1). Values >0.5 are considered to be the equivalent of >50% coarse material. In the HS model, classes 4–6 are high permeability, 1–3 are low permeability, and 0 has unknown permeability. In the AP model, classes 23–28 have high aquifer potential, 21–22 have medium aquifer potential and 15–20 have low aquifer potential. In the CC model, higher values correspond to those with both a higher permeability class in the HS model and a higher aquifer potential in the AP model.

$$CC = \frac{HS}{6} * \frac{facies}{6}$$

Equation 2.1

To provide the CC model as a coarse-fraction classification, if CC was evaluated at greater than 1, then it was set to a max value of 1. Where facies do not exist (e.g. beneath Hastings), CC = HS/6. Like the HS model, the CC model is clipped at -360 mASL. In the basement area, the HS model does not exist. Other than 0, the lowest value possible for the CC model is 0.028 (HS = 1, facies = 1). Therefore, basement values from the AP model (1–14) were normalised by 1000 and mapped directly into the CC model as a discrete range of classes 0.001–0.014. Where basement was defined (HU = 4), and there was no AP model, but the HS_unclipped model existed, CC was set to 0.001, 0.003, 0.006, 0.009, 0.011 and 0.014 for HS_unclipped = 1–6. Where basement was defined (HU = 4), but the AP or HS_unclipped models were not present, CC was set to 0.001.

It can be seen in Table 2.7 that the normalised HS model and CC model values roughly correspond to the fraction of coarse material based on the cluster definitions underlying the HS model. This assumption of correspondence to coarse fraction was checked against lab-based coarse-fraction estimates at 3DAMP_Well2 (Table 2.8; Lawrence et al. 2021), with positive results for 84% of the available values (Table 2.8). In fact, the HS and CC models performed better than geologist assessments of coarse fraction based on lithological log descriptions (Kellett et al. 2022) where this coarse fraction was <0.6 (Table 2.8). The intervals that do not match in Table 2.8 correspond to relatively thin packages of material surrounded by larger packages of material with different properties (e.g. ~1.5 m sand and pumice layer surrounded above and below by 5 m of clay) where the CC model is not able to overcome the vertical model averaging to discriminate these differences.

Additionally, the assessment in Table 2.8 highlighted that the CC model does indeed perform better than the HS model for HS = 3, particularly where the coarse material is dominated by sand rather than gravel. Although still under-estimating the coarse fraction, the CC model successfully moved intervals into the aquifer rather than aquitard definition (taking 50% coarse material as the threshold value between aquifer and aquitard).

3DAMP_Well2 is the only location to have detailed lab-based grain-size analysis in the area. The comparison in Table 2.8 between lab-based measurements versus estimates made on lithological log descriptions should be kept in mind when assessing the results versus other lithological logs compared to the CC model. For this reason, no other detailed comparisons are presented.

Although the CC model results in less discrimination in the higher permeability classes (due to the truncation at 1, more values are mapped to a higher coarse fraction), it provides more discrimination at the mid-range of values than the HS model.

The CC model calculation was made on the combined dataset, which now has columns *X*, *Y*, *Z*, *top_elev_HU*, *res*, *resvar*, *HU*, *HS_unclipped*, *HS, facies*, *AP*, *aq* and *CC*.
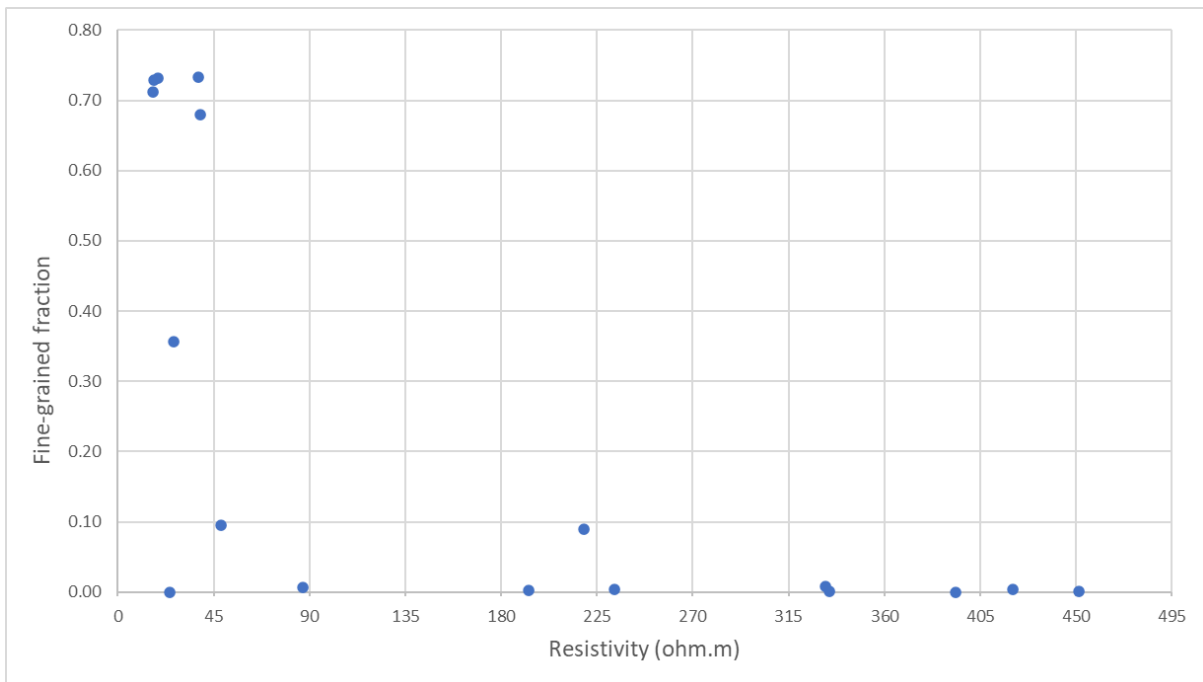
Figure 2.8   Fine-grained fraction of material samples from lab-based grain-size analysis versus resistivity of samples from resistivity cells. All samples with >0.5 fine-grained fraction have resistivity values less than 45 ohm.m. Data is from 3DAMP_Well2 (Lawrence et al. 2021) and was additionally cleaned to remove values with higher uncertainty (preferentially used resistivity values measured during drilling and ignored values as outliers that plotted too far off the contact resistance versus bulk resistivity linear trend). Fine-grained material corresponds to clay and silt.

Table 2.7   Hydrostratigraphic (HS) and Coarse-fraction Classification (CC) model comparison, showing the approximate correspondence to coarse fraction. AP = Aquifer Potential model.

HS Model	HS Model Permeability	HS/6 and CC where Facies = 6 (AP = 20) ~Coarse Fraction	CC where Facies = 7 (AP = 21)
6	High: <20% clay	1	1
5	High: <30% clay	0.83	0.97
4	High to medium: <50% clay	0.67	0.78
3	Low to medium: >50% clay	0.5	0.58
2	Low: >70% clay	0.33	0.39
1	Low: >80% clay	0.17	0.20
0	Unknown: 0–100% clay	0	0

Table 2.8   Comparison between Hydrostratigraphic (HS) model, Coarse-fraction Classification (CC) model and 3DAMP_Well2 grain-size analyses (Lawrence et al. 2021). A threshold of 0.5 is chosen for colouring – where models match the grain-size analysis (above or below 0.5), they are coloured green, and, where they mismatch, they are coloured red. This indicates whether the material has been correctly categorised as an aquifer (>0.5) or an aquitard (≤0.5). All values are rounded to one decimal place. Prior to lab-based grain-size analysis being carried out, grain-size estimates were made by geologists based on both hand samples (Lawrence et al. 2021) and lithological log descriptions alone (Kellett et al. 2022).

Sample Depth (m)	Coarse Fraction (Lab Grain-Size Analysis)	Coarse Fraction (Geologist Estimate on Hand Sample)	Coarse Fraction (Geologist Estimate on Lithological Log)	CC (Closest 2 m Interval)	HS/6 (Closest 2 m Interval)	HS Definition in Coarse Fraction (c.f. Permeability in Table 2.7)	Comment
2	0.3	0.4	0.0	0.4	0.3	<0.3	HS matches better. ~1.5 m of sand immediately above. (HS = 2, facies = 7).
4	0.3	0.2	0.0	0.2	0.3	<0.3	HS matches better. ~6 m clay package. (HS = 2, facies = 4)
6	0.3	0.2	0.1	0.2	0.3	<0.3	HS matches better. ~6 m clay package. (HS = 2, facies = 4)
7	0.3	0.2	0.1	0.2	0.3	<0.3	HS matches better. ~6 m clay package. (HS = 2, facies = 4)
9.8	0.8	0.8	0.8	0.2	0.3	<0.3	Both mismatch: ~1.5 m sand and pumice layer surrounded above and below by 5 m of clay.
10	0.8	0.8	0.8	0.4	0.5	<0.5	Both mismatch: ~1.5 m sand and pumice layer surrounded above and below by 5 m of clay.
20	0.9	0.9	0.9	0.7	0.5	<0.5	Both slightly low, but CC a better match: ~6 m interval 20–26 m depth with sandy shell dominance and clay above and below. (HS = 3, facies = 8).
25	1.0	1.0	1.0	0.7	0.5	<0.5	Both slightly low, but CC a better match: ~6 m interval 20–26 m depth with sandy shell dominance and clay above and below. (HS = 3, facies = 8).

Sample Depth (m)	Coarse Fraction (Lab Grain-Size Analysis)	Coarse Fraction (Geologist Estimate on Hand Sample)	Coarse Fraction (Geologist Estimate on Lithological Log)	CC (Closest 2 m Interval)	HS/6 (Closest 2 m Interval)	HS Definition in Coarse Fraction (c.f. Permeability in Table 2.7)	Comment
27.8	0.6	0.4	0.3	0.7	0.5	<0.5	CC matches better. Sandy shell dominance within a clay package. (HS = 3, facies = 8).
30	0.3	0.3	0.3	0.7	0.5	<0.5	HS matches better. ~2.5 m clay surrounded by gravel/sand – lower, more clayey part of the sandy shell package. (HS = 3, facies = 8).
35	1.0	1.0	1.0	0.9	0.7	>0.5	CC matches better
40	1.0	1.0	1.0	1.0	0.7	>0.5	CC matches better
50	1.0	0.9	1.0	1.0	1.0	>0.8	Both match
54.4	0.9	0.9	0.9	1.0	1.0	>0.8	Both match
54.7	1.0	0.6	0.2	1.0	1.0	>0.8	Both match (for the purpose of the geologist estimates, 'organic' is not here considered as coarse material)
67.8	1.0	1.0	1.0	1.0	0.8	>0.7	CC matches better
70	1.0	1.0	1.0	1.0	0.8	>0.7	CC matches better
84.4	1.0	0.9	1.0	1.0	0.8	>0.7	CC matches better
93.4	0.9	1.0	1.0	1.0	0.8	>0.7	CC matches better
100	1.0	1.0	1.0	1.0	0.8	>0.7	CC matches better
114	1.0	1.0	1.0	1.0	0.8	>0.7	CC matches better

2.1.7   Horizontal Hydraulic Conductivity (K_H)

In this section, the relationship between the previously developed 3D models and estimates of horizontal hydraulic conductivity K_H from aquifer tests is explored.

The link between geoelectric properties and hydraulic conductivity is complex, as both the porosity and geometry of pore spaces cannot be uniquely determined using electrical resistivity. A large number of studies have been performed, with seemingly contradictory empirical relationships between resistivity and hydraulic conductivity being determined: both direct and inverse relationships (e.g. Niwas and Celik [2012] and references therein). This is because the Archie's law assumption that all electrical conduction is through fluid-filled pore space is erroneous. In support of this, it has been theoretically derived by Purvance and Andricevic (2000) that an inverse relationship is obtained when interconnected pore *volumes* dominate electrical current flow and a direct relationship obtained when the interconnected pore *surface areas* dominate electrical current flow (Slater 2007). This results in the commonly empirically determined linear log-log relationship between horizontal hydraulic conductivity K_H and resistivity ρ:

$$K_H = b\rho^c$$

or

$$log_{10} K_H = c \, log_{10} \, \rho + d$$

where the constant values *b*, *c* and *d* are empirically determined. When pore volume conduction dominates, *c* is negative, while when pore surface area conduction dominates, *c* is positive (Purvance and Andricevic 2000). To satisfy theoretical constraints, there must only be small variations in water conductivity, anisotropy (of pore size distributions impacting hydraulic conductivity), cementation and porosity over the volume investigated (Purvance and Andricevic 2000). Hydraulic data must also be scaled so that equal-scale hydraulic conductivity and electrical conductivity values are being compared (Purvance and Andricevic 2000). The applicability of this correlation will therefore depend on the particular properties of the aquifer under investigation.

Pore surface area conduction dominates in freshwater-clay environments, such as the Heretaunga Plains, due to the increased resistivity of freshwater (compared to saline water) and the fine-grained nature of clay increasing the internal surface area (Purvance and Andricevic 2000). This results in an increase in electrical resistivity associated with an increase in permeability.

As Figure 2.9 displays, there is substantial variance that has previously been found through different empirical estimates from studies of different aquifers. As discussed by Purvance and Andricevic (2000), these large variances are likely to do with the local depositional environment and anisotropy of the aquifer properties. A brief exploration into this correlation in Hawke's Bay was previously performed by Meilhac et al. (2009), where an empirical relationship was derived between resistivity from NanoTEM measurements and hydraulic conductivity estimates from slug tests (Figure 2.10) and used to construct a hydraulic conductivity profile along the Waipawa River in the Ruataniwha Plains.

In many sedimentary and glacial deposition environments, clay content can be considered as inversely proportional to hydraulic conductivity. Previous studies have also empirically determined a relationship between the fraction of coarse material (F_c) and horizontal hydraulic conductivity K_H, e.g. this linear equation from Faunt (2009): $K_H = F_c K_c + F_f K_f$. Here, F_f is defined as $1 - F_c$, K_c is set as the maximum hydraulic conductivity for a cell composed of 100% coarse material, and K_f is set as the minimum hydraulic conductivity for a cell composed of 100% firm clay.
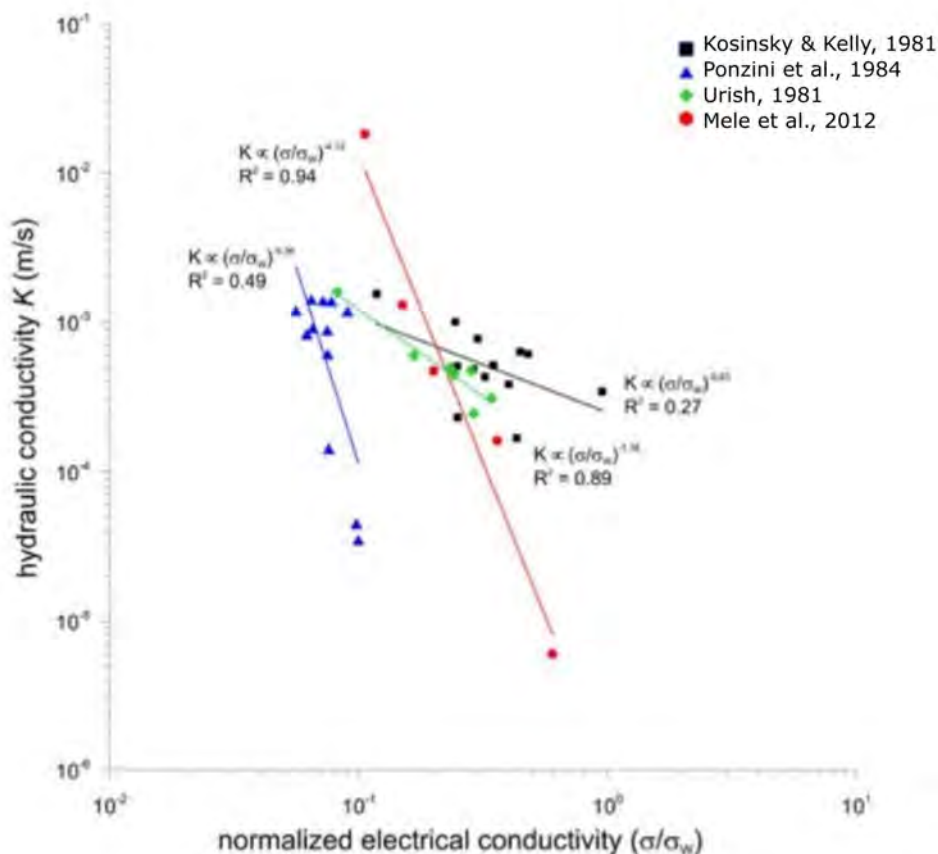
Figure 2.9   Correlation between average hydraulic conductivity (K) and normalised electrical conductivity (inverse of resistivity) of freshwater-saturated hydrofacies (σ_w: average electrical conductivity of pore water) and comparison with negative field-scale correlations cited in the literature (Kosinski and Kelly 1981; Ponzini et al. 1984; Urish 1981). Figure and caption adapted from Mele et al. (2012). The relationships shown are equivalent to an increase in electrical resistivity corresponding to an increase in permeability. Normalisation was performed for a more direct comparison between the different study areas.
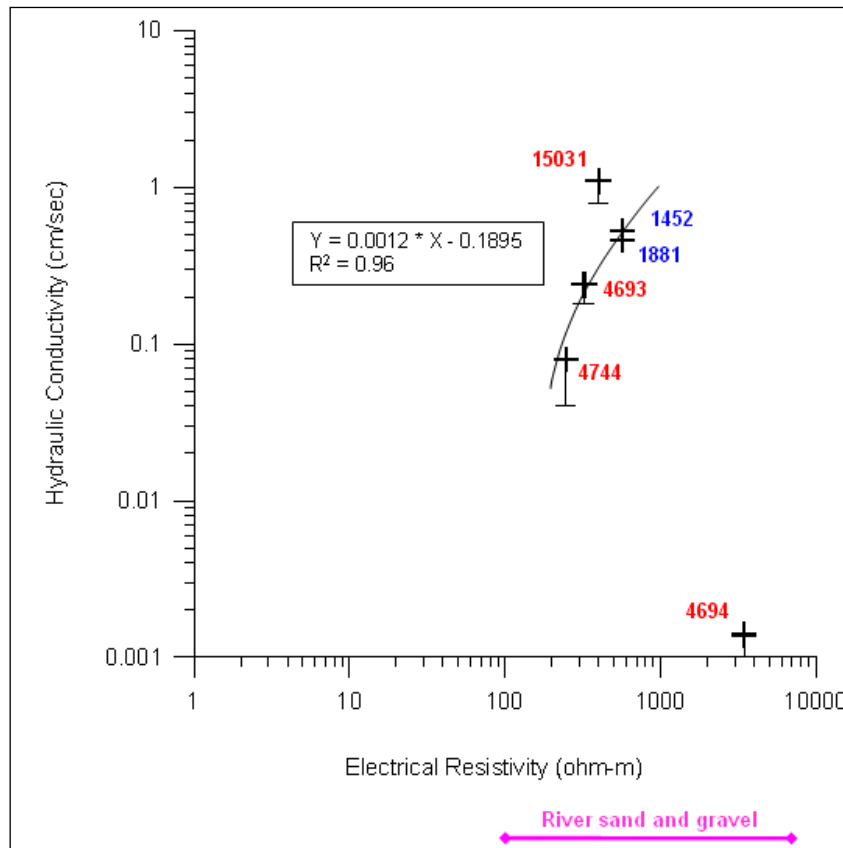
Figure 2.10   Correlation between hydraulic conductivity obtained from aquifer tests and electrical resistivity obtained from NanoTEM in the Ruataniwha Plains, Hawke's Bay. Figure from Meilhac et al. (2009).

2.1.7.1   Hydraulic Conductivity Dataset

The previously compiled hydraulic conductivity (K_H) dataset for the Heretaunga Plains from Tschritter et al. (2022) was utilised for this assessment. However, based on noted unusually high values (>7000 m/day; Moore 2023), a further manual quality check was performed. The high values (>7000 m/day) were observed to be a consequence of very short intervals (screen length) used for the conversion from transmissivity to hydraulic conductivity. This conversion factor is often not consistently handled. To ensure all hydraulic conductivity values were consistently obtained, new K_H estimates were calculated from available transmissivity values.

Estimates of hydraulic conductivity were made by dividing the transmissivity obtained from the pumping tests by the screen length (water supply interval determined in Tschritter et al. [2022]) with an additional 4 m added – corresponding to an additional 2 m above and 2 m below the top and bottom of the screen. This is where the influence of pumping is assumed to be most significant (extrapolating from isolines for pumping shown in Bouwer and Rice [1976]; Perwick and Woodhouse 2014; Moore 2023). Pumping tests given a confidence rating of low by Perwick and Woodhouse (2014) were removed and not assessed further. Where there was no water supply interval defined by Tschritter et al. (2022), the Perwick and Woodhouse (2014) dataset was checked for any screen information. The comment section of the HBRC borehole construction information file (Tschritter et al. 2022) was also checked for any comments on screen length, and this length was preferentially chosen if there was a discrepancy between the datasets. Where the construction information file contained ambiguous information and multiple screen information, the lithological log was cross-checked to assist with appropriate value selection. If none of the three datasets contained information on screen length, the transmissivity value was removed and not utilised.

Figure 2.11 shows the resulting new K_H estimates, which largely display an expected pattern of lows and highs across the aquifer system. As some of the K_H values were still considered higher than physically reasonable for numerical groundwater modelling purposes (Moore 2023), the 90th percentile value was calculated (not including K_H values obtained from sandstone and limestone as determined in the water supply intervals) and used as a maximum threshold value. This results in all values above 2455 m/day being set to 2455 m/day in the below assessments.

Of note for assessing the validity of using this pumping dataset as the primary source to compare to the 3D models is that the dataset source is, by its nature, biased toward higher K_H values. Slug and pumping tests are difficult to obtain in low permeability sediments due to the long wait times for the water levels to return to equilibrium. Additionally, pumping tests are usually only performed within sediments with enough permeability that they are desirable to be used for a water supply.

Information on expected K_H values for lower permeability unconsolidated sediments are available from slug tests performed in the Ruataniwha Plains at 3DAMP_Well1 and 3DAMP_Well3 (Lawrence et al. 2022a; 2022b): silty clay (40% coarse fraction) with K_H = 0.001 m/day and clay (20–40% coarse fraction) with K_H = 0.25 m/day. Literature values provide $K_H = 10^{-4} - 10^{-7}$ m/day for clay, $K_H = 1 - 10^{-3}$ for silt and $K_H = 10^{-1} - 10$ m/day for silty sand (Heath 1983). Rakowski and Knowling (2018) found a lowest value in their calibrated Heretaunga groundwater flow model of $K_H = 0.01$ m/day.
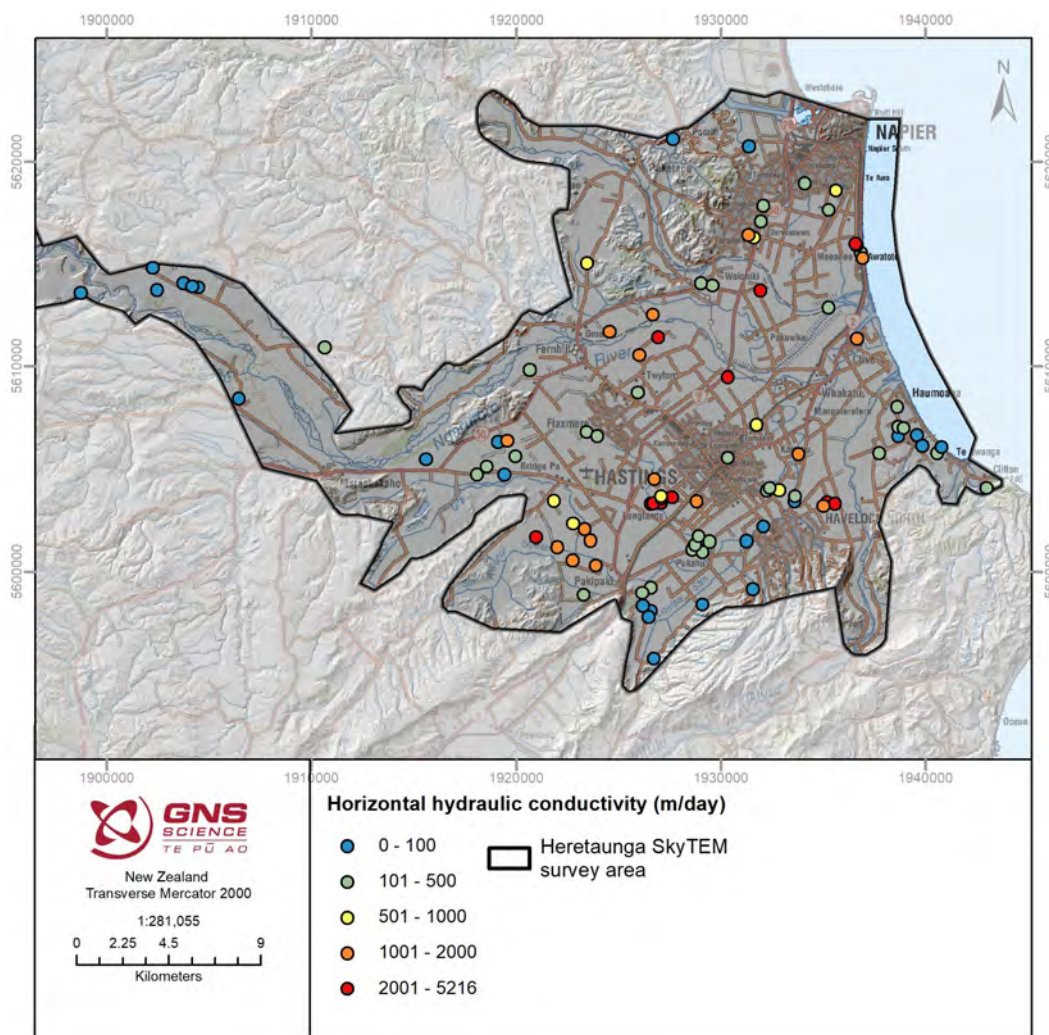
Figure 2.11   Quality-checked and corrected horizontal hydraulic conductivity (K_H) values used for comparison to the SkyTEM-derived 3D models.

2.1.7.2 Comparison of K_H Dataset to 3D Models

Three-dimensional model data were selected within the same horizontal cell as the pumping bore, and vertical cells were selected covering the screen interval, +2 m above the screen and -2 m below the screen (the same interval considered most influential during pumping and used for the transmissivity to K_H conversion in Section 2.1.7.1). As the 3D models have a 2 m vertical cell resolution, multiple cells with potentially different model values were thus selected. From these selected cells, for each different 3D model, the geometric mean was calculated.

Graphs depicting the results of this comparison are shown below for the res model (Figure 2.11), the AP model (Figure 2.12), the HS model (Figure 2.14) and the CC model (Figure 2.15). For the continuous res and CC models, linear regression equations were determined and the associated residual standard error (RSE) calculated.

As expected for the Heretaunga Plains aquifer environment, direct (rather than inverse) equations were empirically determined – where an increase in resistivity corresponds to an increase in permeability and where clay content is inversely proportional to hydraulic conductivity:

$$Log_{10}(K_H) = 1.2588 * Log_{10}(res) + 0.2768 \qquad (RSE = 0.54) \qquad \text{Equation 2.2}$$

$$Log_{10}(K_H) = 1.5173 * CC + 1.3864 \qquad (RSE = 0.57) \qquad \text{Equation 2.3}$$

For interest, the relationship for the AP model is also shown without the log scale for K_H. Without the log axis, the graph highlights consistency with the previously determined aquifer potential classes and the weighting function applied to generate the CC model – that aquifer potential increases at AP = 21 (K_H values greater than 1000 m/day estimated). This graph also highlights that K_H decreases for AP = 27. Due to the limited data points, it is unclear whether this is an observation of significance.

$$Log_{10}(K_H) = 1.2588 Log_{10}(res) + 0.2768$$
$$RSE = 0.54$$

Figure 2.12   Horizontal hydraulic conductivity (K_H) versus res model linear regression equation, as well as +/-2.5*RSE. RSE is an estimate of the variance of the error term for the equation fit to data, and 95% of values are expected to be found within 2*RSE. Blue points are the estimates of K_H made from pumping test data (Section 2.1.7.1).
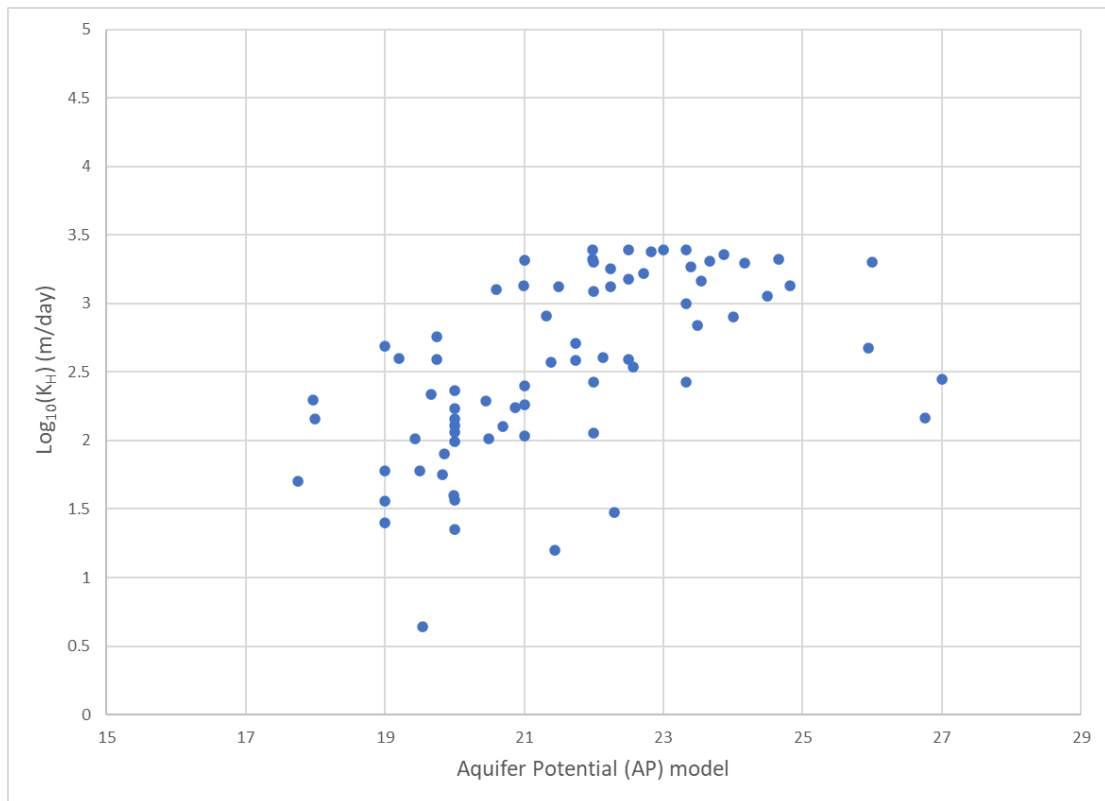
Figure 2.13   Horizontal hydraulic conductivity (K_H) versus the Aquifer Potential (AP) model. Blue points are the estimates of K_H made from pumping test data (Section 2.1.7.1).
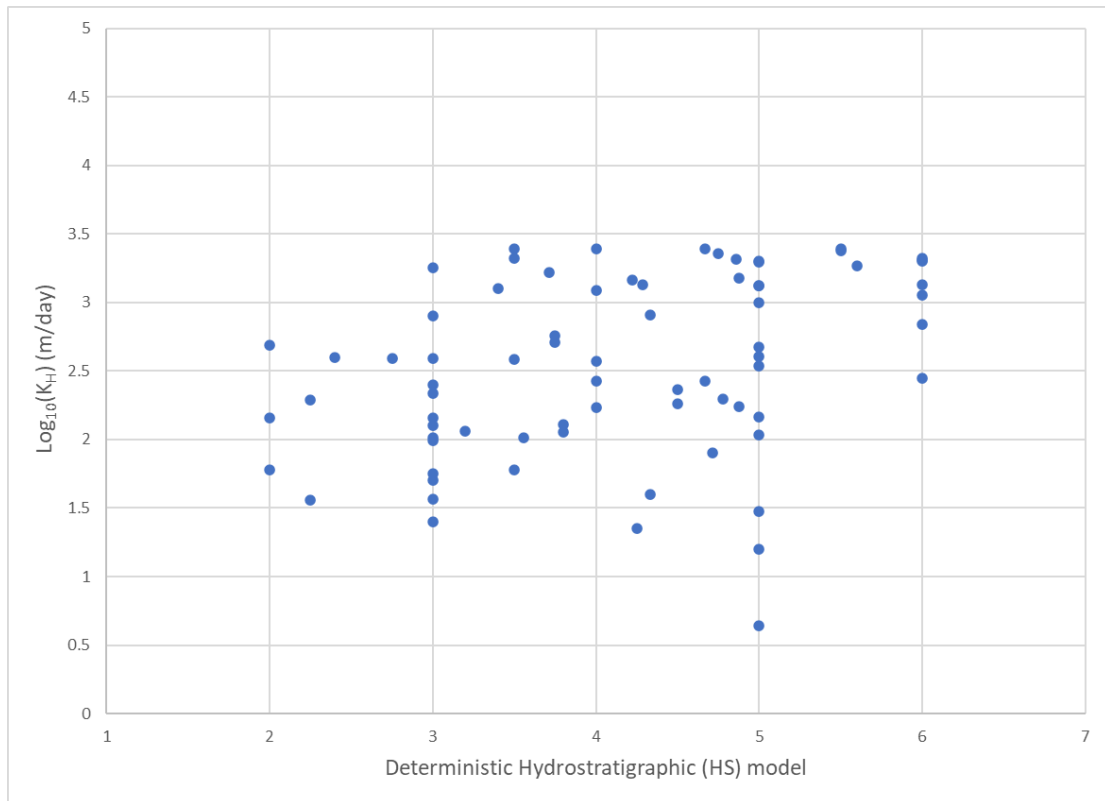
Figure 2.14   Horizontal hydraulic conductivity (K_H) versus the Hydrostratigraphic (HS) model. Blue points are the estimates of K_H made from pumping test data (Section 2.1.7.1).
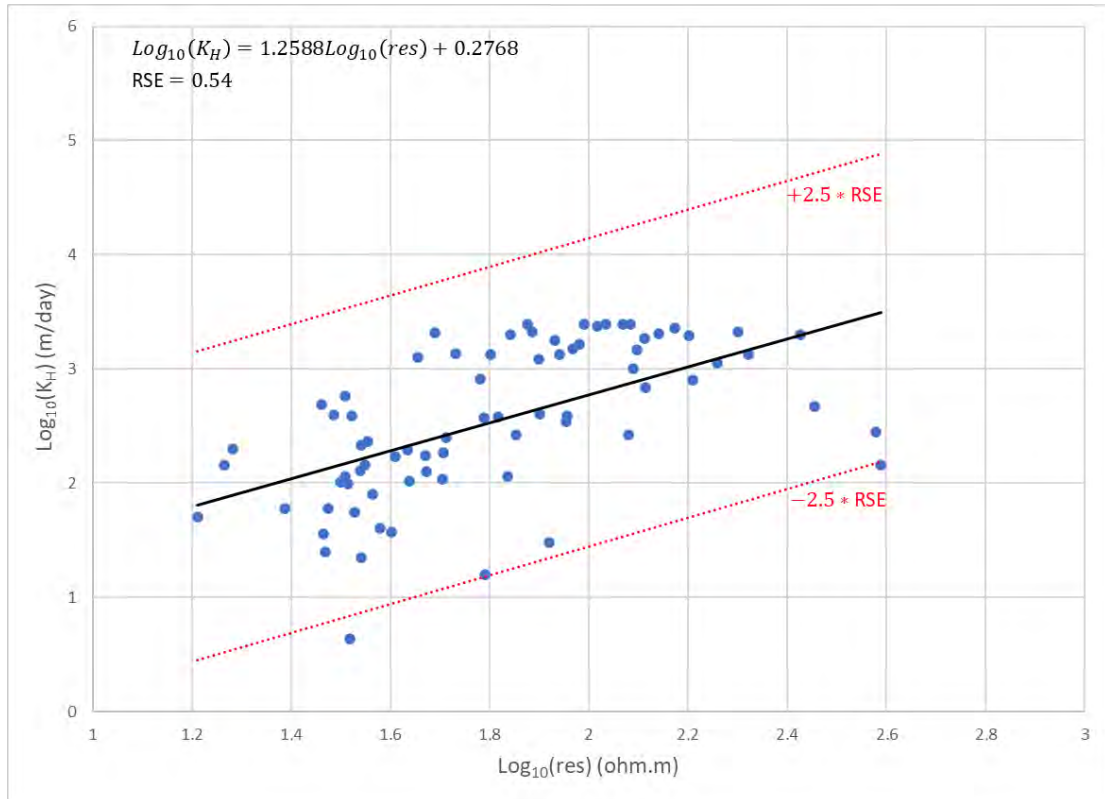

Figure 2.15   Horizontal hydraulic conductivity (K_H) versus CC model linear regression equation, as well as +/-2.5*RSE. RSE is an estimate of the variance of the error term for the equation fit to data, and 95% of values are expected to be found within 2*RSE. Blue points are the estimates of K_H made from pumping test data (Section 2.1.7.1).

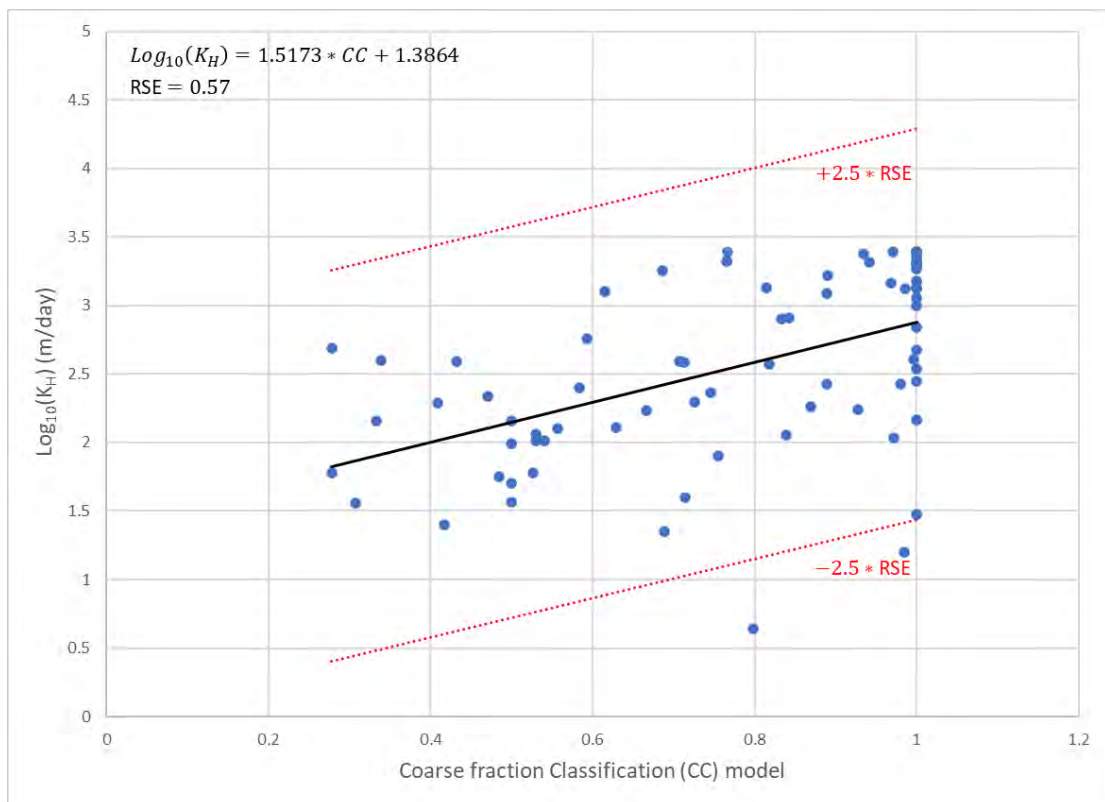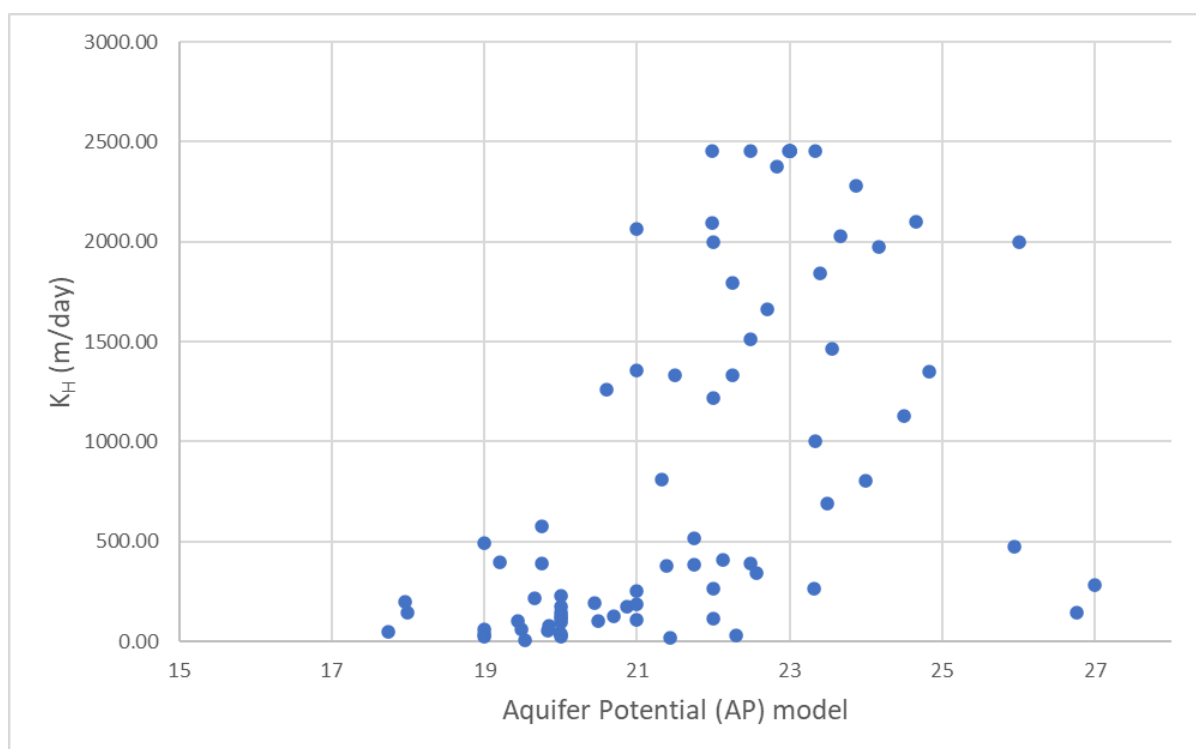Figure 2.16 Aquifer potential model shown versus horizontal hydraulic conductivity (K_H). The same data as Figure 2.11 is shown, but, without the log axis, the graph highlights consistency with the previously determined aquifer potential classes – that aquifer potential increases at AP = 21 (K_H values greater than 1000 m/day estimated).

2.1.7.3 Implementation

Although methods for optimal utilisation of these 3D models for informing numerical groundwater models will be explored in more depth using numerical experiments in a subsequent piece of work in 3DAMP, a demonstration is provided here of using these 3D models for generating estimates of initial horizontal hydraulic conductivity (K_H). The numerical Heretaunga GW model was used for some preliminary testing of the derived K_H values, as well as expert knowledge.

Initially, K_H estimates were made using the mean of the res and CC model relationships derived in Section 2.1.7.2. However, when these values were checked using expert knowledge and the Heretaunga GW model (Hemmings 2023; Moore 2023), it was determined that low K_H values were not adequately represented. This is not surprising considering the bias of the pumping test data toward high values (see Section 2.1.7.1).

To overcome this dataset limitation, a synthetic data relationship was developed for the CC model. This is achievable for the CC model, as it is directly related to a physical property; however, it is not possible to do the same for the res model. As such, a high value was set at CC = 1 of K_H = 2455 m/day and a low value at CC = 0.1 of K_H = 0.01 m/day. This low value is consistent with literature values for silt (Section 2.1.7.1), as well as with Rakowski and Knowling (2018), who found a lowest value in their calibrated Heretaunga groundwater flow model of K_H = 0.01 m/day. Additionally, for K_H values to be useful for numerical models, it is important to consider upscaling impacts (e.g. although literature values for clay are much lower, it is unlikely that a 100 x 100 m grid cell will be fully composed of such low K_H material). A linear trend was fitted to these points (Figure 2.17):

$$Log_{10}(K_H) = 5.9889 * CC - 2.5989$$

<div style="text-align: right">Equation 2.4</div>

Testing using the Heretaunga GW model with K_H values derived from this relationship highlighted that K_H values in the high range were still coming out too high (unable to maintain river flows in the Heretaunga GW model; Hemmings 2023). As the CC model has less discrimination within the high value range (CC >0.9) than the res model, a combined approach was used to overcome this limitation, taking the minimum value calculated from either Equations 2.2 or 2.4. Where only one model exists (e.g. where the CC model fills gaps in the res model), only that model was utilised to calculate K_H. Testing of these K_H values in the Heretaunga GW model and against expert knowledge provided suitable results (Hemmings 2023; Moore 2023).

The relationships utilised assume that electromagnetic conduction in the area is primarily controlled by the amount of clay material present and so follow the same limitations as the hydrostratigraphic modelling – that this assumption is not valid in basement (consolidated) rock or where pore water is heavily influenced by saltwater. As such, these areas are required to be dealt with in a different manner (see below).

It is possible that there is saline influence within facies ≤4. For these areas, only the CC model was used for the calculation (Equation 2.4). For basement (HU = 4), assumed values were set directly rather than being calculated from the 3D models (see section on consolidated K_H below). Three different sets of basement values were used to address different numerical model requirements (*KH_initial*, *H_initial_basehigh* and *KH_initial_base1*). To deal with the locations likely heavily influenced by saltwater, and where there is data from only one model, a Boolean operator model (*KH_unc*) was developed: 0 corresponds to model cells with both CC and resistivity model data and no influence of saltwater, and 1 corresponds to model cells with one or none of CC or resistivity model data or with a likely heavy influence of saltwater (facies = 1, resistivity <8 ohm.m). This model can be used to reflect the increase in uncertainty in these areas *(KH_unc* = 1).

The CC model is clipped at -360 mASL. The KH models were also clipped to -360 mASL.

As such, seven models were developed, enabling further numerical GW model utilisation to be easily explored:

1. $K\_res = 10^{1.2588*\mathrm{Log}_{10}(\mathrm{res})+0.2768}$

2. $K\_CC = 10^{5.9889*\mathrm{CC}-2.5989}$

3. $K\_min = \min(K_{\mathrm{res}}, K_{\mathrm{CC}})$; where facies ≤4, $KH\_min = K\_CC$.

4. *KH_initial* = *KH_min* (except where HU = 4, see below).

5. *KH_initial_basehigh* = *KH_min* (except where HU = 4, see below).

6. *KH_initial_base1* = *KH_min* (except where HU = 4, see below).

7. *KH_unc*: Boolean operator (0/1), where 1 identifies areas of higher uncertainty.

These calculations were made on the combined dataset, which now has columns *X, Y, Z, top_elev_HU, res, resvar, HU, HS_unclipped, HS, facies, AP, aq, CC, K_res, K_CC, K_min, KH_initial, KH_initial_basehigh, KH_initial_base1, KH_unc.*

The figure shows a scatter plot with the equation:
$$Log_{10}(K_H) = 5.9889 * CC - 2.5989$$

Y-axis: $Log_{10}(K_H)$ (m/day). X-axis: Coarse fraction Classification (CC) model.

Legend:
- Pumping test data
- Synthetic data
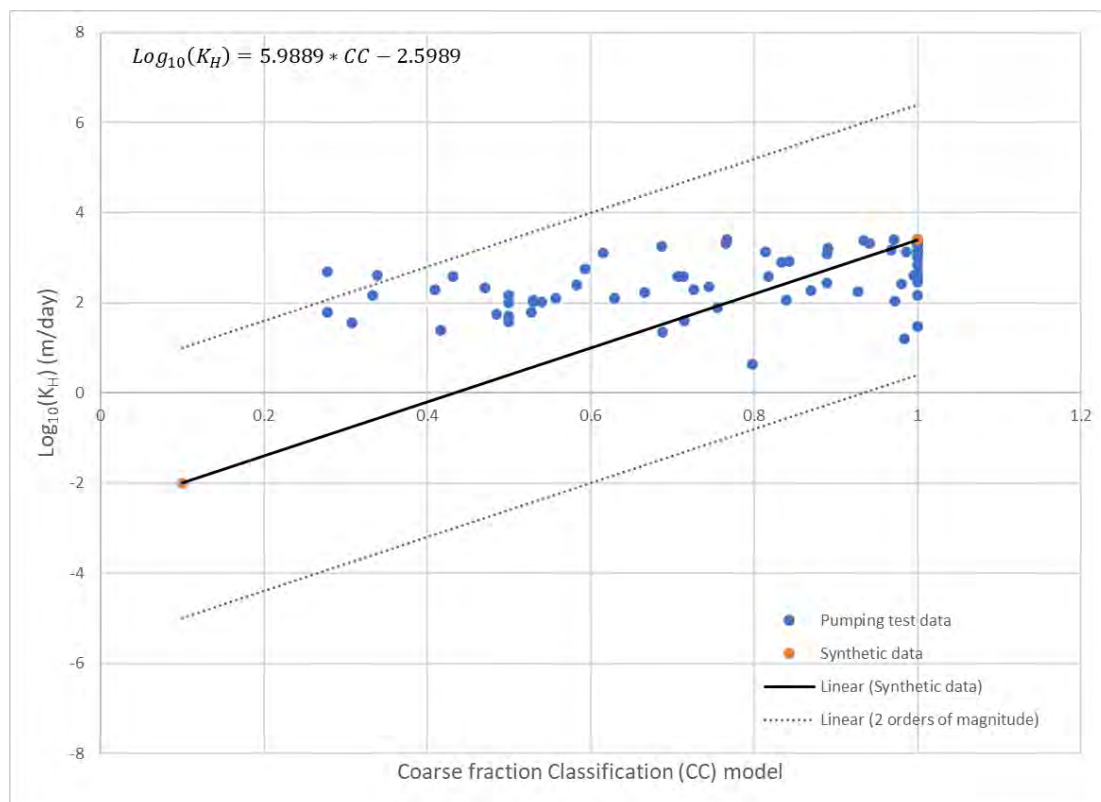- Linear (Synthetic data)
- Linear (2 orders of magnitude)

Figure 2.17   Horizontal hydraulic conductivity (K_H) versus CC model linear regression equation to synthetic data points developed from expert knowledge, as well as +/-2 orders of magnitude. Blue points are the estimates of K_H made from pumping test data (Section 2.1.7.1).

Consolidated K_H

As the relationships explored above are only relevant for the unconsolidated areas, for the consolidated material (HU = 4), literature values of K_H and information available from pumping tests in the areas were utilised (Section 2.1.7.1). Multiple models were developed to enable different use purposes.

Literature values (e.g. Freeze and Cherry 1979) were used to select a K_H value for consolidated material with low aquifer potential of 5×10^{-4} m/day. This could be suitable for a numerical groundwater model wishing to represent the basement as a no-flow boundary or for primarily assessing just K_H values relevant to unconsolidated sediments. As such, a *KH_initial* dataset was developed with all consolidated sediments mapped with $K_H = 5 \times 10^{-4}$ m/day.

To enable further explorations of potential connections with limestone and sandstone, a *KH_initial_basehigh* dataset was also developed with different values mapped for sandstone and limestone. Low aquifer potential was considered equivalent to mudstone/siltstone, medium aquifer potential equivalent to sandstone and high aquifer potential equivalent to limestone (Table 2.9). Where there was HU model information but no resistivity information, a low aquifer potential was assumed (Table 2.9).

Pumping test information in limestone provided K_H values between 0.4 and 60.6 m/day, with a mean of 28.5 m/day. As these values are from pumping tests performed on water-bearing limestone, they represent upper values for the limestone material with high aquifer potential. Pumping-test information in sandstone provided K_H values between 0.1 and 0.8 m/day, with a mean of 0.4 m/day. As these values are from pumping tests performed on water-bearing sandstone, they represent upper values for the sandstone material (e.g. medium to high aquifer potential).

Preliminary testing within the Bridge Pa GW model demonstrated that a higher K_H value was needed for basement here due to a large portion of the model consisting of basement represented by a relatively thin layer (Moore 2023). As such, an additional *KH_initial_base1* model was developed, providing higher values for basement for use in the Bridge Pa GW model (Table 2.9).

Table 2.9   Horizontal hydraulic conductivity (K_H) mapping for consolidated sediments. HU = hydrogeological unit; CC = coarse-fraction classification; AP = aquifer potential.

HU	CC	AP	Assumption	K_H_initial (m/day)	K_H_initial_basehigh (m/day)	K_H_initial_base1 (m/day)
4	0.001–0.009	1–9	Mudstone/ siltstone	5×10^{-4}	5×10^{-4}	1
4	0.010–0.011	10–11	Sandstone	5×10^{-4}	0.4	1
4	0.012–0.014	12–14	Limestone	5×10^{-4}	28.5	28.5
4	N/A	N/A	Basement	5×10^{-4}	5×10^{-4}	1

2.1.8   Data Formats

The 3D model datasets were combined within a point *.csv* file, with x,y,z defining the centre of each grid cell. Attribute columns relate to each of the different 3D models. This format was developed for serving the data on an online webmap. The format provides quick access to all datasets for cross-section and virtual borehole visualisations, as all datasets reference the same x,y,z locations. Additionally, a selection of the 3D models was exported to individual *x,y,z,value .csv* files to enable 3D visualisation as individual block models within a Leapfrog viewer file.

A selection of the 3D models was also converted into multi-band raster files, enabling further accessibility such as visualisation of elevation slices within GIS software and easy utilisation by numerical groundwater models. Each multi-band raster contains 441 bands in elevation order, where Band 1 = 286 mASL and Band 441 = -594 mASL, with each band consisting of a 2-m-thick vertical slice referenced to the cell centre (i.e. Band 1 = 285–287 mASL). This elevation information is included within the metadata of the files. The 500 hydrostratigraphic realisations underlying the deterministic hydrostratigraphic model (Foged 2022) were similarly converted to multi-band raster files for easy utilisation by numerical groundwater modelling.

Additionally, two further supporting datasets for the 500 hydrostratigraphic realisations were developed to support potential numerical model explorations. One file in *.csv* format contains the percentage of the 500 realisations for each cluster 0–4 within every model cell (original model grid used for the 500 hydrostratigraphic realisations): *X, Y, Z, perc0, perc1, perc2, perc3, perc4.* The second file contains the original point datasets underlying the 500 hydrostratigraphic realisations at the SkyTEM data locations: *X, Y, Z, clay_fraction, clay_fraction_STD, cluster, silhouette_index.*

2.2   2D Maps

2.2.1   Saline Influence in the Near Surface

The offshore resistivity models and the resistivity models in magenta in Figure 2.6 were excluded from the hydrostratigraphic modelling due to the significant influence of saltwater in the resistivity models (Foged 2022). The magenta models were selected based on areas containing resistivity values <8 Ωm (freshwater should result in resistivity values >8 Ωm;

e.g. Duque et al. 2022, Foged 2022, Madarasz-Smith et al. 2016, Wilson et al. 2006). Onshore, these magenta areas are consistent with the locations of bores with saline water in the upper ~30 m and saline-influenced water within estuaries and river mouths (e.g. Tschritter et al. 2022).

Deeper bores in this area draw from a freshwater source, and resistivity measurements from water samples have values between 27 and 67 ohm.m (Tschritter et al. 2022). Additionally, this area is where the fine-grained marine sediments of the Awatoto member have been mapped at the surface (Lee et al. 2020; Tschritter et al. 2022). These fine-grained marine sediments are expected to have a low resistivity character. This combination of saline-influence and fine-grained marine sediments makes this area challenging to interpret with certainty, as low resistivity may be a consequence of either the geology or the saline influence (or a combination of both).

As such, a polygon of potential near-surface saline-influence was created to indicate areas that may be influenced by salinity – the model results in these areas should be treated with additional caution, but the area was not removed in the assessments below.

To create this polygon, the minimum facies class in the upper 30 m was calculated and a raster created. This raster was converted to a polygon, and a selection made of facies classes between 1 and 4 that were continuous with the coastline (Figure 3.5). Up to facies 4 (resistivity less than 22 ohm.m) was selected, as this approach created continuity with the facies = 1 locations and resulted in an area roughly equivalent to the magenta areas selected for exclusion during the hydrostratigraphic modelling (Foged 2022; Figure 2.6). A simplified version of this polygon was also created that only corresponds to facies = 1.

2.2.2   Aquifer Thickness

As the CC model has near-complete data coverage (includes basement and fills resistivity data gaps) and has been shown to provide the best fit to lab-based grain-size analyses (Sections 2.1.6 and 2.1.7), as well as providing meaningful comparisons to pore-water electrical conductivity and lithological logs, it was selected for deriving 2D maps in this section.

In this section, a simplifying assumption is made that an aquifer corresponds to >50% coarse material (CC >0.5) and an aquitard corresponds to ≤50% coarse material (CC ≤0.5). This is similar to Hansen et al. (2016), who used a definition of at least 50% clay to define aquitard material. Due to depth limitations of the models, aquifer material is found at the base of the CC model in some areas, and the actual aquifer thickness may be greater than calculated here.

2.2.2.1 Total Aquifer Thickness Maps

All model cells with CC >0.5 were selected and the vertical thickness summed for each horizontal cell. This information was converted to a raster file to provide a total aquifer thickness map (Figure 3.6). This process ignores any complexity of multi-layered aquifers that may be separated by aquitards and highlights only the total thickness of aquifer material.

The total aquifer thickness raster file was converted to polygons of aquifer thickness and aquifer extents. To simplify the aquifer extent polygon, any polygon parts smaller than 1 km were eliminated.

The total aquifer thickness was divided by the full thickness of unconsolidated sediments within the CC model (clipped at -360 mASL) for each horizontal cell and multiplied by 100.

This information was converted to a raster file to provide a map of the percentage of unconsolidated sediments classified as an aquifer (Figure 3.6).

2.2.2.2 Surficial and Deep Aquifer Thickness Maps

Horizontal cells that had CC >0.5 at the land surface were selected and the vertical thickness directly beneath of CC >0.5 summed for each of these horizontal cells. If any two consecutive cells (total of 4 m thickness) with CC ≤0.5 was encountered, then the thickness summation ceased. This information was converted to a raster file to provide a surficial aquifer thickness map (Figure 3.6).

The difference between the total aquifer thickness and the surficial aquifer thickness was calculated. This information was converted to a raster file to provide a deep aquifer thickness map (Figure 3.6).

2.2.3 Near-Surface Properties

Near-surface property estimates are important for a number of purposes, including improving understanding of groundwater–surface water interaction and guiding riverbed conductance values for numerical groundwater modelling.

Both the harmonic mean and geometric mean were calculated for the upper 5 m, 10 m, 15 m, 20 m, 30 m and 50 m for the *res*, *resvar*, *CC*, *KH_initial*, *KH_initial_basehigh* and *KH_initial_base1* models. Each dataset was converted to a raster file that was clipped at the coastline to provide indicator maps of near-surface properties (Figure 3.7).

2.2.4 Aquifer Near-Surface Vulnerability and Confinement

Aquifer confinement status is one measure used to assess how well protected a water source is from surface contamination sources (aquifer vulnerability). Aquifer vulnerability assessments are a means to synthesise complex hydrogeological information into a form useable by planners, decision- and policy-makers, geoscientists and the public. For example, Schedule V of the Hawke's Bay Regional Resource Management Plan uses different approaches to aquifer vulnerability based on the existing confined and unconfined polygons in the Heretaunga Plains (HBRC 2006; Good Earth Matters 2019). Confinement status is typically determined by the location of artesian water pressures at boreholes; however, to create a higher-resolution map of confinement using the SkyTEM data, a different approach is needed.

Hydrogeological interpretations of SkyTEM data have previously been used by Hansen et al. (2016) to find a correlation between aquifer vulnerability to surface nitrate contamination in Denmark and the thickness of material with more than 50% clay in the upper 30 m (interpreted from the SkyTEM data) in the upper 30 m (and using combined geochemical, geological and numerical models). Within their study area, the clay thickness varied from <5 m to more than 30 m, and data synthesis showed that a protective clay-layer thickness of less than 5 m resulted in aquifers with a high nitrate vulnerability, a thickness of between 5 m and 30 m resulted in aquifers with medium nitrate vulnerability and a thickness of more than 30 m resulted in aquifers with a low nitrate vulnerability (compared to measured nitrate values). The high, medium and low categories were made to simplify complex information for decision- and policy-makers. It was not reported what travel times these thicknesses correspond to.

For the purpose of assessing drinking-water protection for groundwater sources, Lough et al. (2018) provide drinking-water security guidelines of a one-year travel time for Source Protection Zone 2 (intermediate zone for protection from microbial contamination and chemical discharges or spills; Moreau et al. 2014). Due to the potential policy and management link between aquifer vulnerability and confinement status, estimating aquitard thickness equivalent to a one-year travel time is a useful approach to further guide decision-making.

In this section, confinement status is estimated by assessing locations where an aquifer is protected by an overlying aquitard (>50% clay) with an estimated minimum one-year travel time. This requires estimates of both aquitard thickness across the study area and the aquitard thickness that corresponds to a one-year travel time. Confinement status validation is undertaken by comparing results to measured water-level data. As the CC model has near-complete data coverage (includes basement and fills resistivity data gaps) and has been shown to provide the best fit to lab-based grain-size analyses (Sections 2.1.6 and 2.1.7), as well as providing meaningful comparisons to pore-water electrical conductivity and lithological logs, it was selected for deriving 2D maps in this section.

2.2.4.1 Aquitard Thickness Corresponding to a One-Year Travel Time

Tonkin & Taylor (2018) investigated source protection at a number of bores in Hastings. Of the bores assessed, Frimley Park and Eastbourne Street had low permeability material in the near surface relating to an overlying confining layer. These bores are located in an area where the CC model has a value of 0.33 in the near surface (equivalent to an aquitard).

At these locations, Tonkin & Taylor (2018) estimated vertical hydraulic conductivity of 0.05 m/day, an effective porosity of 0.03 and a mean velocity of 0.065 m/day, using an assumed hydraulic gradient based on a 2 m head difference between ground surface and the reported top of the screen. On a review of supporting information, Tonkin & Taylor (2018) found that, in the area of the Hastings District Council borefields, the effective porosity range is 0.02–0.06, with 0.02 being the most conservative value.

Tonkin & Taylor (2016) also undertook a bacteriological contamination investigation in the Brookvale Road water supply bores, located in Brookvale Road, Havelock North (part of the Heretaunga Plains aquifer) to determine the source of the 2016 Havelock North gastroenteritis outbreak. They modelled travel times within the capture zone, using a two-layer aquifer model, and found that they needed to use effective porosity values in the range 0.01–0.15 to match travel times from tracer tests (using K derived from pumping tests). At these bore locations, the CC model has 0.89 at the surface (equivalent to an aquifer).

Changes in assumptions of effective porosity, vertical hydraulic conductivity and hydraulic gradient would all impact the velocity obtained and hence the vertical thickness corresponding to a one-year travel time. Groundwater velocity, *V*, can be estimated as:

$$V = Ki/neff$$

where *K* is the hydraulic conductivity (evaluated from pumping tests), *i* is the measured hydraulic gradient and *neff* is the effective porosity. Exploring the impact of varying all three parameters within reasonable parameter ranges results in a very wide band of potential one-year travel-time thickness values (e.g. 0.02–71 m). In this instance, as the vertical hydraulic conductivity and hydraulic gradient values come from field data, only the impact of changing effective porosity was explored further.

The effective porosity lower bound of 0.01 found at Brookvale Road is considered too small, due to CC = 0.89 at this location. Estimates of effective porosity at a location with CC = 0.33 vary between 0.02 and 0.06, corresponding to velocities of 0.03 and 0.1 m/day (Tonkin & Taylor 2018). For a one-year travel time, these are equivalent to thicknesses of 11 m and 37 m, with the 0.065 m/day estimate used by Tonkin & Taylor (2018) corresponding to a thickness of 24 m.

2.2.4.2 Aquitard Thickness Across the Study Area

From initial testing, it was determined that there is a portion of the CC model, especially in the range 0.5–0.6, that appears to correspond to semi-permeable material (equivalent to the highly re-worked material with small-scale heterogeneity mentioned previously in Section 2.1.6, where thin permeable material is surrounded by more impermeable material: for example, gravel <5 m thick, surrounded above and below by clay, or thicker mixtures of silt and sand with thin gravel lenses). As such, two assessments were made here, one classified aquitard material as CC ≤0.5 and the other classified aquitard material as CC ≤0.6. The differences between the two results highlight the zones of semi-permeable material.

The CC thresholds above were used to assess the continuous thickness of aquitard material in the unconsolidated sediments in the upper 50 m. Continuous aquitard units were considered important to assess confinement and protection. If a single cell (equivalent to a 2 m thickness) greater than the CC threshold was encountered, then continuity was considered broken and the cumulative thickness count was restarted. The greatest total cumulative thickness in the upper 50 m was saved as the aquitard thickness. Additionally, to remove the potential of including basement material (particularly relevant in shallow river valleys where the unconsolidated thickness is relatively shallow and there is a higher uncertainty on the basement clipping surface that was used), cumulative thickness was only calculated if there was at least one cell greater than the CC threshold encountered beneath the aquitard units (i.e. an aquitard was only defined where there is an underlying aquifer).

2.2.4.3 Aquifer Confinement/Vulnerability

The aquitard thicknesses developed in Section 2.2.4.2 were converted to raster files and compared to areas of known flowing artesian conditions (e.g. Tschritter et al. 2022). It was found that a thickness of 11 m (equivalent to an effective porosity of 0.06) was most consistent with these artesian conditions and thus to confinement.

The raster files of aquitard thickness were clipped at the coastline and converted into polygons with all thickness properties. These raster files were also re-classified into three categories and converted into categorical aquifer confinement polygons (Table 2.10).

Table 2.10   Aquifer confinement polygon classification.

Category	Thickness
Unconfined	0 m
Semi-confined	2–11 m
Confined	>11 m

2.2.5 Horizontal Hydraulic Conductivity through the Full Thickness of Unconsolidated Sediments

To provide an estimate of horizontal hydraulic conductivity through the full thickness of the model area, the KH models from Section 2.1.7 were used to calculate both the geometric mean and harmonic mean of horizontal hydraulic conductivity through the vertical column of unconsolidated sediments (HU <4) and through basement (HU = 4) where this was present at the surface. This information was converted to raster files (Figure 3.9). The geometric mean is useful to understand average horizontal flow properties, while the harmonic mean highlights the influence of lower permeable material and is related to vertical flow properties.

3.0 RESULTS AND DISCUSSION

3.1 Three-Dimensional Gridded Model Development

A series of 3D models was developed using the same horizontal regular grid as the Heretaunga numerical groundwater model (that will be revised in a subsequent piece of work in 3DAMP). Three-dimensional model datasets were combined within a *.csv* file, with x,y,z defining the centre of each grid cell and including the following parameters: *X, Y, Z, top_elev_HU, res, resvar, HU, HS_unclipped, HS, facies, AP, aq, CC, K_res, K_CC, K_min, KH_initial, KH_initial_basehigh, KH_initial_base1, KH_unc* (Table 3.1; Figures 3.1–3.4). A selection of these models was converted to multi-band raster format, enabling further accessibility such as visualisation of elevation slices within GIS software and easy utilisation by numerical groundwater modelling.

The 3D models utilise 100 x 100 m grid cells horizontally and 2-m-thick grid cells vertically using the same horizontal regular grid as the Heretaunga numerical groundwater model (Rakowski and Knowling 2018). Grid cells are defined in elevation (relative to mean sea level) rather than in depth (relative to the ground surface), so exact clipping at the surface varies based on the grid location versus the DEM location. A 25 m resolution DEM was used for surface clipping (Sahoo et al. 2023).

A summary of the developed models is provided below:

- An interpolated resistivity (res) model, which interpolated the SkyTEM-derived smooth resistivity model and available resistivity models from ground-based surveys to the regular grid. Model gaps remain at distances greater than 500 m from any resistivity data and below the calculated standard DOI.

- A major Hydrogeological Unit (HU) model, which utilised the previously developed manually delineated major hydrogeological unit surfaces to split the 3D grid into four units. The surfaces were developed using interpolation, which fills gaps in the resistivity data (e.g. beneath Hastings).

- A deterministic Hydrostratigraphic (HS) model, which utilised the previously developed 500 realisations of a five-cluster model (with 10 m vertical resolution) to develop a 95% likelihood model with seven classes and utilised the basement HU to restrict the model to only the unconsolidated sediments (where the hydrostratigraphic modelling assumptions are valid). The hydrostratigraphic modelling enabled a variable relationship between resistivity and permeability across the study area, using clay fraction as an indication of permeability. It also used the sharp resistivity model and geostatistical simulations to fill gaps in the resistivity data (e.g. beneath Hastings). The model is clipped at depth to -360 mASL, as the 500 realisations were (as this is a depth to which resistivity model data is still relatively continuous through the study area).

- A resistivity facies (facies) model, which separated the res model into 14 $\log_{10}$-based uniform intervals, grouping materials that are expected to have similar hydrologic and geologic properties based on their resistivity (to assist with easier discrimination of significant variability and similarity). Model gaps are the same as in the res model.

- An Aquifer Potential (AP) model, which has 28 classes and utilised the HU and facies models to separate the model into likely consolidated sediments (basement; 14 classes) and likely unconsolidated sediments (14 classes), while providing an indicator of the likelihood of each model cell to host aquifer-bearing material (after assessments against other datasets such as lithological logs). This model utilised the same relationships between resistivity and permeability across the entire study area. Model gaps are the same as in the res model.

- A Coarse fraction Classification model (CC), which combined the HS and AP models to remove some of the limitations and combine the strengths of each model, providing a 0–1 model of estimated coarse fraction. It was primarily developed due to inspections of lithological data against the HS model, which highlighted some resolution limitations of significance for hydrogeological understanding (most likely due to the underlying hydrostratigraphic model realisations having 10 m vertical resolution). Within the unconsolidated sediments, a weighting function was developed to combine the AP and HS models, while, within the consolidated sediments, available models were individually used. The CC model combines information from both the smooth and sharp resistivity models, as well as borehole information via the hydrostratigraphic modelling previously undertaken and through manual inspections to inform the weighting function. The coarse fraction estimates from the CC model performed well compared to lab-based coarse fraction measurements from a bore drilled as part of 3DAMP (3DAMP_Well2). The CC model also has the greatest spatial coverage, with resistivity data gaps filled by the HS model (a gap in the AP model), and also greatest information on consolidated sediments (a gap in the HS model). The model is clipped at depth to -360 mASL, as the HS model is.

- Horizontal Hydraulic Conductivity models (K_H), calculated for the unconsolidated sediments using empirical relationships between horizontal hydraulic conductivity estimates from pumping tests and the res and CC models, initially provided values that were too high. Some iterative testing was performed using the Heretaunga GW model and guided by expert knowledge to develop a linear relationship between CC and horizontal hydraulic conductivity values using synthetic data points. The empirical relationship with the res model and the expert-knowledge-guided relationship with the CC model enabled the calculation of initial parameter estimates of horizontal hydraulic conductivity that performed well in initial Heretaunga GW model testing. Literature values, expert knowledge and local pumping test information were used to assign discrete values for the consolidated sediments, with three different associated models developed.

The models developed are limited by the supporting datasets available, such as lithological logs, grain-size estimates and hydraulic conductivity estimates from pumping test data. Uncertainty increases with increased distance from such supporting datasets. There are limited supporting datasets deeper than 50 m depth (e.g. Tschritter et al. 2022; Kellett et al. 2022), and, as such, uncertainty increases with depth.

Note that, due to the uniform 3D gridding approach taken, resolution is lost along flight lines where the original SkyTEM-derived resistivity models have finer resolution. See Figure 2.2 for a zoomed-in example showing the difference in resolution between the original and gridded datasets. However, given the primary applications of groundwater modelling and online visualisation of the entire datasets, the approach taken is considered appropriate for these applications. The same methodology could be used to create finer-resolution small subsets of the data; otherwise, different gridding approaches could be tested, such as non-uniform gridding within different software or scripting.

The HU model utilised manually delineated surfaces, described within Sahoo et al. (2023). Although there are some resolution limitations of the HU model, which was generated through manual surfaces compared to the HS model, the HS model is not able to distinguish between the high resistivity from limestone rather than from unconsolidated gravel, for instance; hence clipping by the manual surface is required when working with the entire aquifer dataset. Subsequent studies in small, localised areas may wish to utilise the unclipped

HS model to assess basement resolution, which is why both the *HS_unclipped* and *HS* column are provided. It is important to be aware that, although the *HS_unclipped* model seems to map basement well where basement corresponds to low resistivity material such as mudstone and siltstone, where basement is high resistivity, such as limestone, it is misleading and should not be used.

The CC and res models were selected to derive the horizontal hydraulic conductivity datasets, The CC model combines information from the aquifer potential and hydrostratigraphic models, while the resistivity model retains the finest resolution, both spatially and numerically. Although there was a generally linear trend in the relationships found between the 3D models and horizontal hydraulic conductivity, there was a wide band of values around these, and the value of the pumping test dataset for this assessment was limited due to its bias towards high values. Likely the best methodology to utilise these data in a numerical model will enable a variable trend throughout the model to allow for spatial variations – e.g. associated with changing depositional environments.

As the best model domain and methodologies of averaging (upscaling) properties of K_H within numerical groundwater models depend on the questions being asked of the model (type of scenario), it is expected that the selection of the inclusion method of these datasets within numerical groundwater modelling may depend on the question being explored. For example, an additional K_H model was created (*KH_initial_base1*) for use within the Bridge Pa GW model due to the specifics of the construction of that numerical model.

Further datasets relating to the full 500 HS model realisations have been provided to enable potential further testing of methods to utilise these data within numerical models.

Table 3.1   Summary of 3D model names and descriptions.

| Attribute	Description	Type	Comments
X	Easting in NZTM of the centre of the model cell	Numerical	100 m horizontal cell resolution
Y	Northing in NZTM of the centre of the model cell	Numerical	100 m horizontal cell resolution
Z	Elevation (m ASL) in NZVD2016 of the centre of the model cell	Numerical	2 m vertical cell resolution
top_elev_HU	Elevation (m ASL) in NZVD2016 of the centre of the highest Z cell at this X,Y location that has HU data.	Numerical	See Section 2.1.2
res	Resistivity (ohm.m)	Numerical	See Section 2.1.1
resvar	Kriging variance of the resistivity model	Numerical	See Section 2.1.1
HU	Major hydrogeological units	Categorical: 1–4	See Section 2.1.2
HS_unclipped	Deterministic hydrostratigraphic model – not clipped by basement	Categorical: 0–6	See Section 2.1.3
HS	Deterministic hydrostratigraphic model – clipped by basement	Categorical: 0–6	See Section 2.1.3
facies	Resistivity facies model	Categorical: 1–14	See Section 2.1.4
AP	Aquifer potential model	Categorical: 1–28	See Section 2.1.5
aq	Simplified aquifer potential model	Categorical: cl, cm, ch, ul, um, uh	See Section 2.1.5
CC	Coarse-fraction classification model	Numerical: >0.02–1 Categorical: 0.001–0.014	See Section 2.1.6
K_CC	Horizontal hydraulic conductivity (m/day) estimate from the CC model	Numerical	See Section 2.1.7
K_res	Horizontal hydraulic conductivity (m/day) estimate from the res model	Numerical	See Section 2.1.7
K_min	Horizontal hydraulic conductivity (m/day) estimate, min(*K_CC*, *K_res*); where facies ≤4, *KH_min* = *K_CC*	Numerical	See Section 2.1.7
KH_initial	Horizontal hydraulic conductivity (m/day) estimate of initial value (*K_min* and 5×10^{-4} assigned to all consolidated sediments)	Numerical	See Section 2.1.7
KH_initial_ basehigh	Horizontal hydraulic conductivity (m/day) (*K_min* and higher values assigned to likely sandstone and limestone)	Numerical	See Section 2.1.7
KH_initial_ base1	Horizontal hydraulic conductivity (m/day) (*K_min* and all consolidated sediments with a minimum value of 1)	Numerical	See Section 2.1.7
KH_unc	Estimate of areas of higher uncertainty (*KH_unc* = 1) for horizontal hydraulic conductivity estimates	Categorical: 0–1	See Section 2.1.7

This page left intentionally blank.
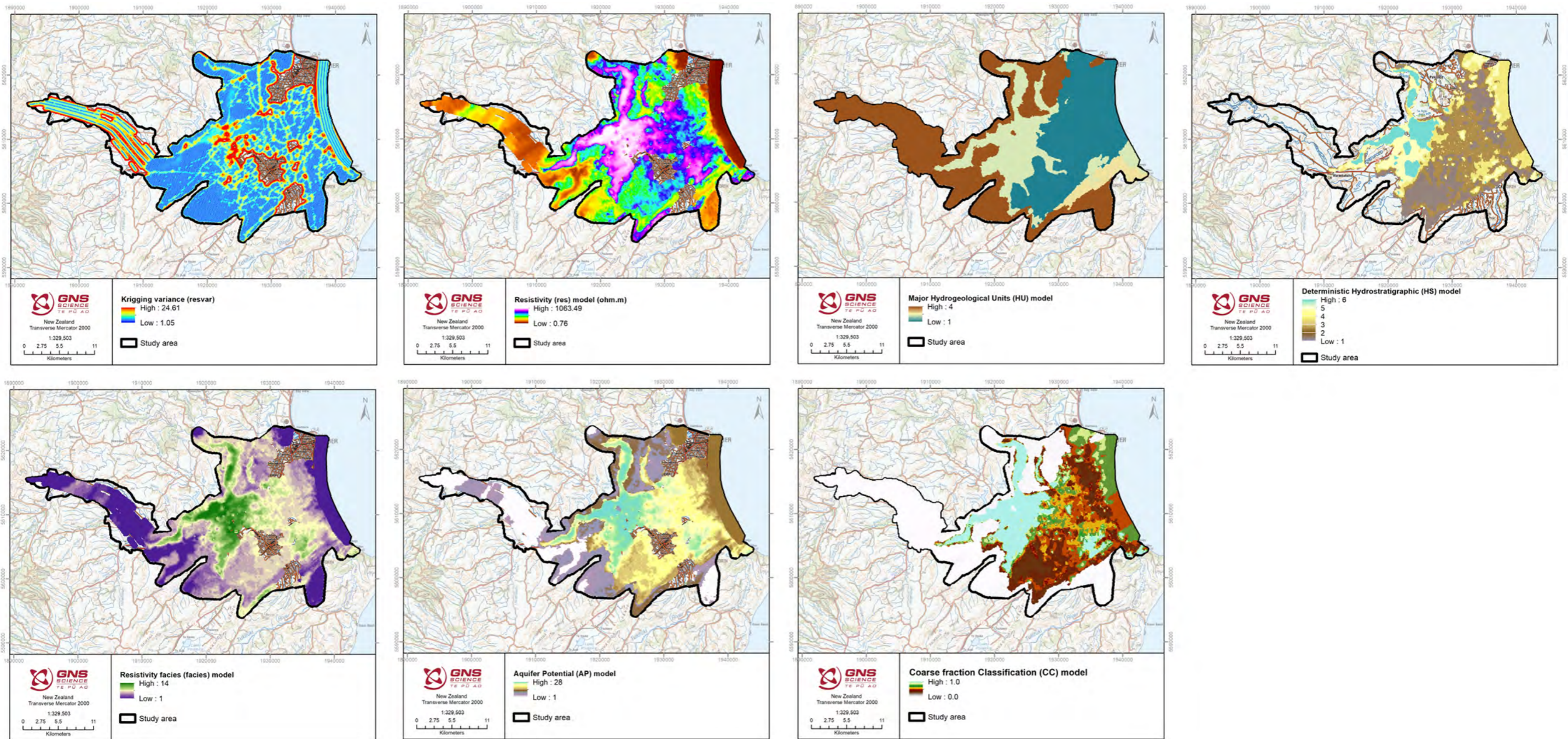
Figure 3.1   Three-dimensional models, map view at -10 mASL. See Sections 2.1.1–2.1.6 for model details.
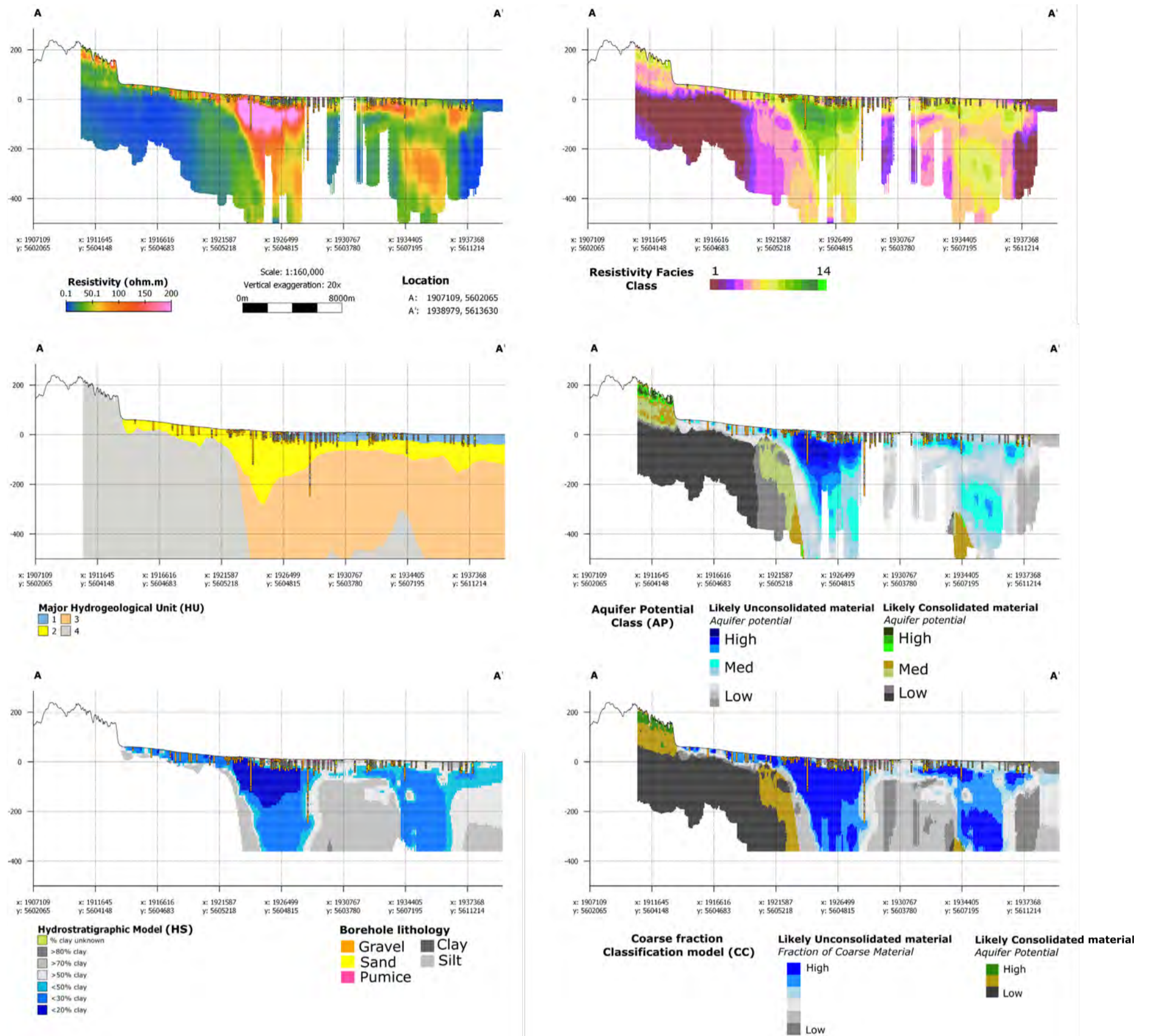
Figure 3.2   Three-dimensional models and borehole lithology shown across profile A–A'. Cross-section location is shown in Figure 2.1. See Sections 2.1.1–2.1.6 for model details.
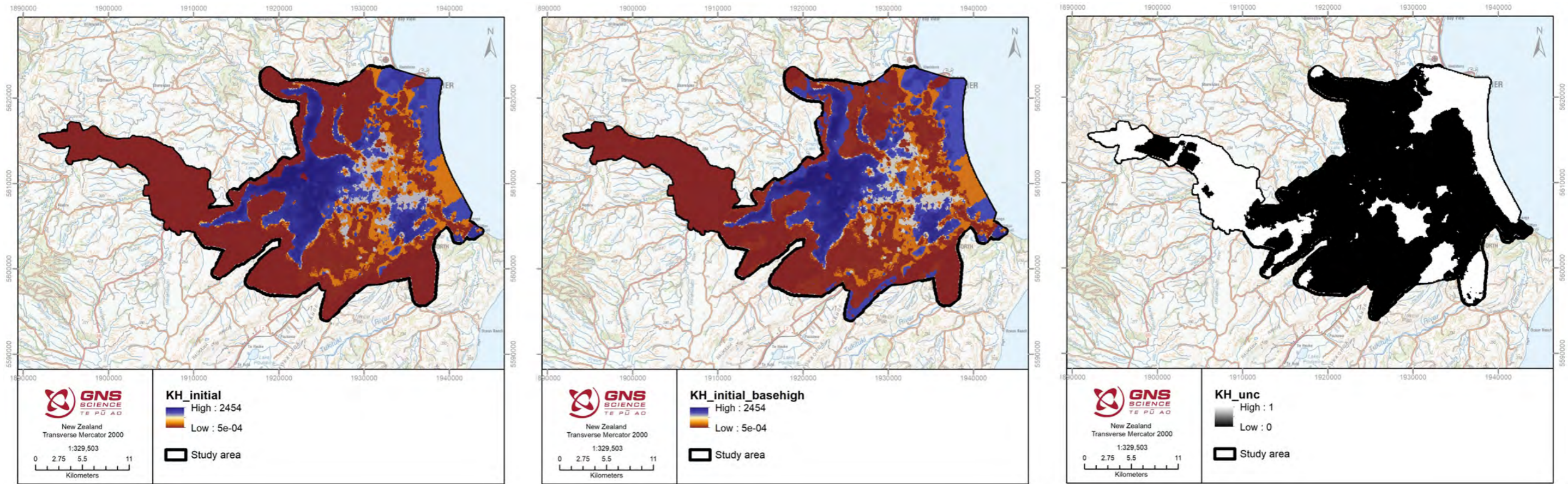
Figure 3.3   Three-dimensional models of horizontal hydraulic conductivity, map view at -10 mASL. See Section 2.1.7 for model details.
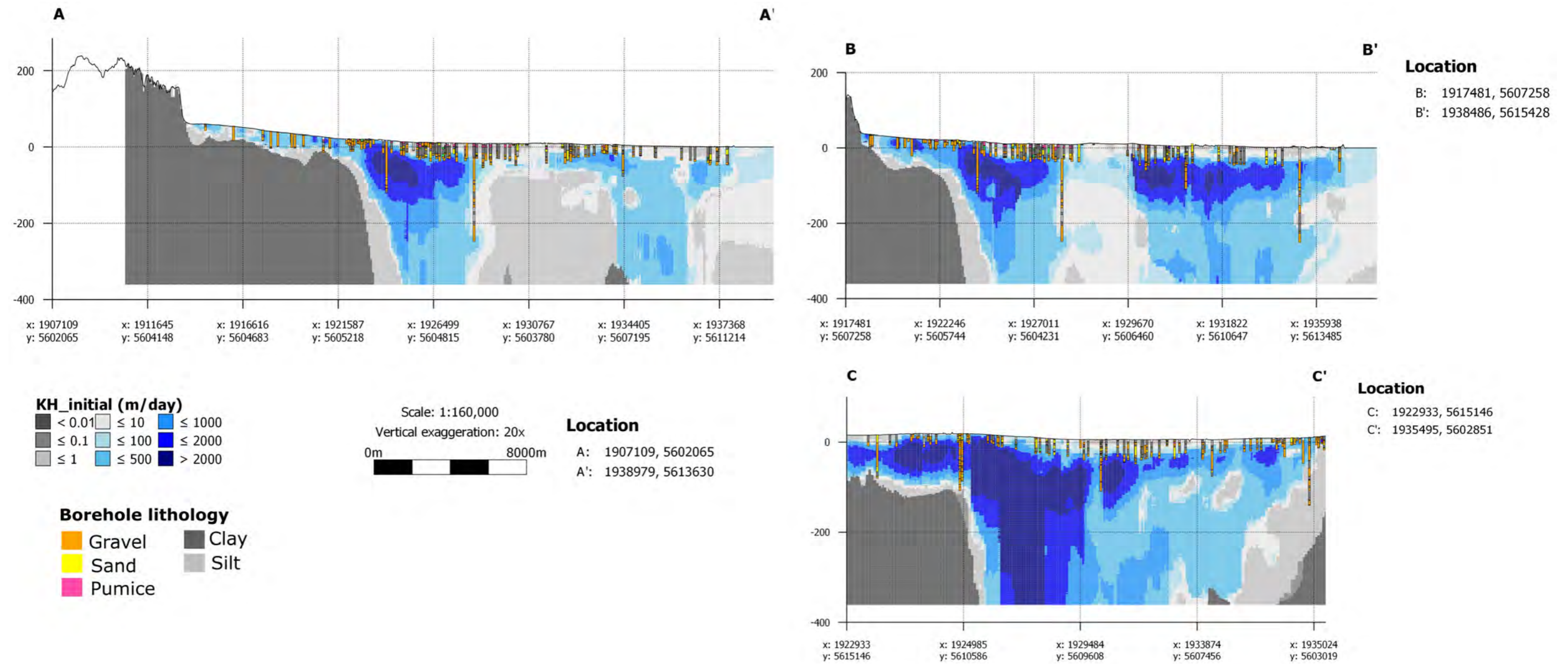
Figure 3.4   Estimates of initial values for horizontal hydraulic conductivity (*KH_initial* [m/day]). Cross-section locations are shown in Figure 2.1. See Section 2.1.7 for model details.

3.2   2D Maps

Simplifications of the 3D models to 2D maps can assist with more readily investigating various aspects of the Heretaunga Plains aquifer system.

Figure 3.5 shows the polygon developed to highlight potential areas in the near-surface (upper 30 m) influenced by salinity and where corresponding map/model products should be treated with additional caution due to a potential breakdown of the underlying assumptions. Facies 1 corresponds to resistivity <8 ohm.m and corresponds to saline-influenced areas (freshwater is classified as >8.3 ohm.m). Facies 2–4 wrap around pockets of facies 1 and may indicate some minor saline influence travelling through permeable paths in the near-surface.

Two-dimensional maps/models derived, primarily using the CC model, include:

- Aquifer thickness maps, separated into surficial, deep, total and total as a percentage of unconsolidated thickness (Figure 3.6). Due to depth limitations of the models, aquifer material is found at the base of the CC model in some areas (e.g. Figure 3.2), and the actual aquifer thickness may be greater than calculated here. This process ignores any complexity of multi-layered aquifers that may be separated by aquitards and highlights only the total thickness of aquifer material.

- Near-surface properties (res, CC and K_H; Figure 3.7) for the upper 5 m, 10 m, 15 m, 20 m, 30 m and 50 m using geometric and harmonic means.

- Aquitard thickness, classified into unconfined, semi-confined and confined (Figure 3.8).

- Geometric and harmonic means of horizontal hydraulic conductivity (K_H) through the full vertical column of unconsolidated sediments and full vertical column of consolidated sediments where these are present at the surface (Figure 3.9).

Aquitard thickness and polygons of aquifer confinement are shown in Figure 3.8. The gap in aquifer thickness over a small part of Hastings (Akina) is likely to be due to the gap in resistivity data in that location and associated high uncertainty of model results. Although this area has been filled in the CC model via previous geostatistical simulations (hydrostratigraphic modelling), the result in this area is a uniform aquitard to full depth (CC = 0.33). The methodology utilised to define aquitard thickness requires some aquifer material to be identified at depth in order to define an overlying aquitard. However, as this requirement was primarily implemented to remove locations where basement may be classified as aquitard, this gap was manually removed as part of the polygon of confinement creation. Although the confinement map derived from aquitard material being defined as CC ≤0.6 best matches the locations of artesian conditions; for the purpose of drinking-water security, the confinement map derived from aquitard material being defined as CC ≤0.5 is considered best. This is based on manual inspections of borehole data through the areas of difference between these two maps. Comparison to bores with flowing artesian water levels highlighted that flowing conditions may be recorded in bores with very localised confinement conditions – this was validated through assessing borehole lithologies in the vicinities – which may vary rapidly between thick clay at the surface to thick sand and intermittent gravel layers. Such localised conditions are not considered to be suitably confined for the purpose of groundwater security due to horizontal flow paths.

There is also ambiguity within the lithological log dataset in these areas, e.g. bores 127 and 2780 are located only 30 m apart; however, one has clay in the upper 15 m, while the other has gravel in the upper 12 m. It is unclear whether this may be due to errors in the database or logging. These areas are near recent river channels and suggest areas of significant re-working and heterogeneity. Thus, CC = 0.5–0.6 represents highly mixed and variable areas with low to medium permeabilities that may be a consequence of, for example, mixtures of silt and sand, and thin gravel within larger clay packages.

The 2016 Havelock North drinking-water contamination at the Brookvale bores is in an area on the edge of the confined area, in a highly permeable unit.
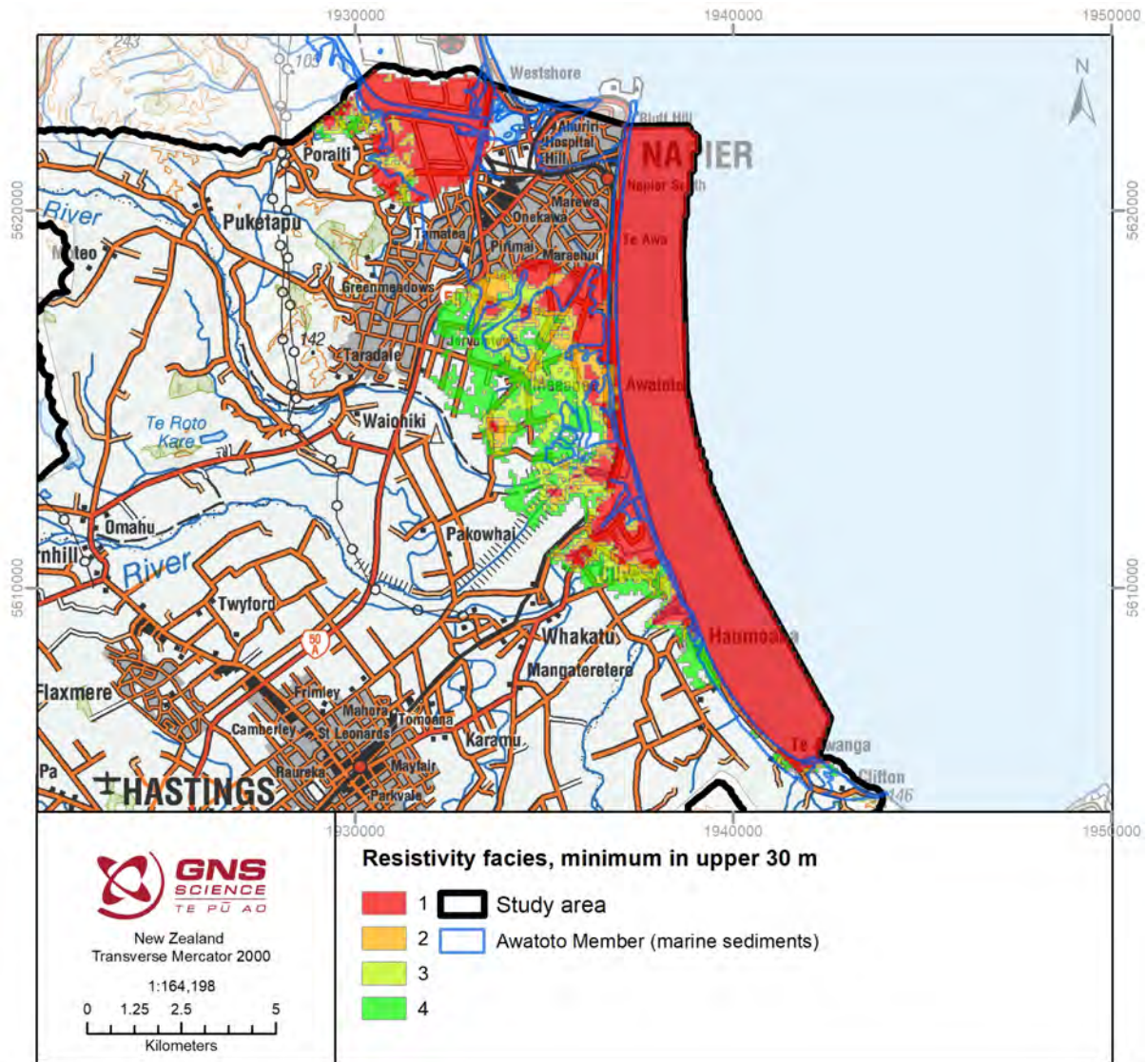

Figure 3.5   Saline influence in the near-surface, as determined by the minimum resistivity facies in the upper 30 m. '1' indicates definite saline influence (resistivity <8 ohm.m), and the likelihood of saline influence decreases as the facies numbers increase. The mapped extent of the Awatoto Member is also shown for comparison, as this fine-grained geological unit is expected to also have a low resistivity character.
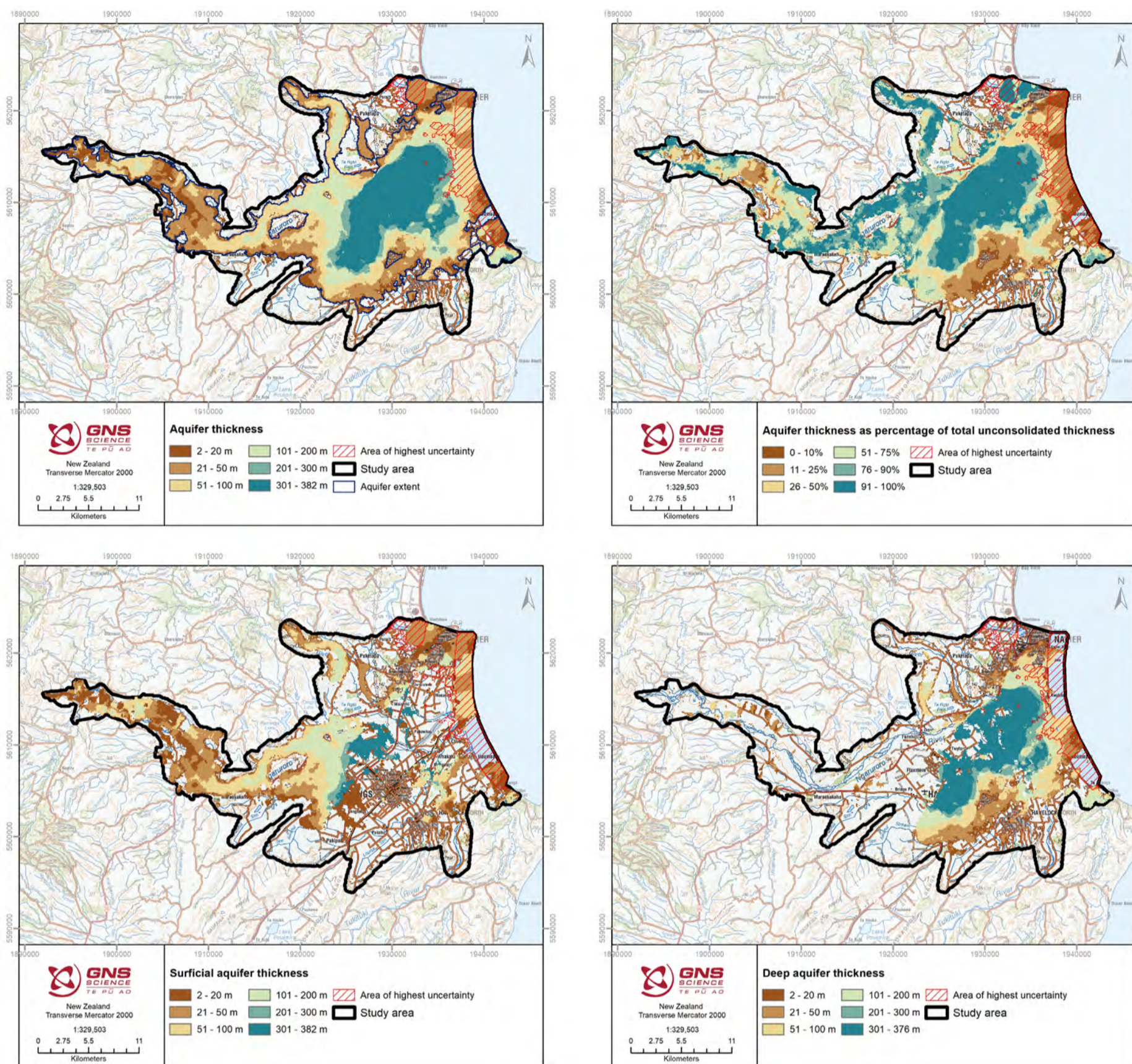
Figure 3.6   (Top left) Aquifer thickness and aquifer extent, (top right) aquifer thickness as a percentage of total unconsolidated thickness, (bottom left) surficial aquifer thickness and (bottom right) deep aquifer thickness. All are calculated from model cells with CC >0.5. See Section 2.2.2 for further details. The area of highest uncertainty displayed is the location of facies = 1 from the saline-influence polygon developed (Section 2.2.1; Figure 3.5). Due to depth limitations of the models, aquifer material is found at the base of the CC model in some areas (e.g. Figure 3.2), and the actual aquifer thickness may be greater than calculated here.
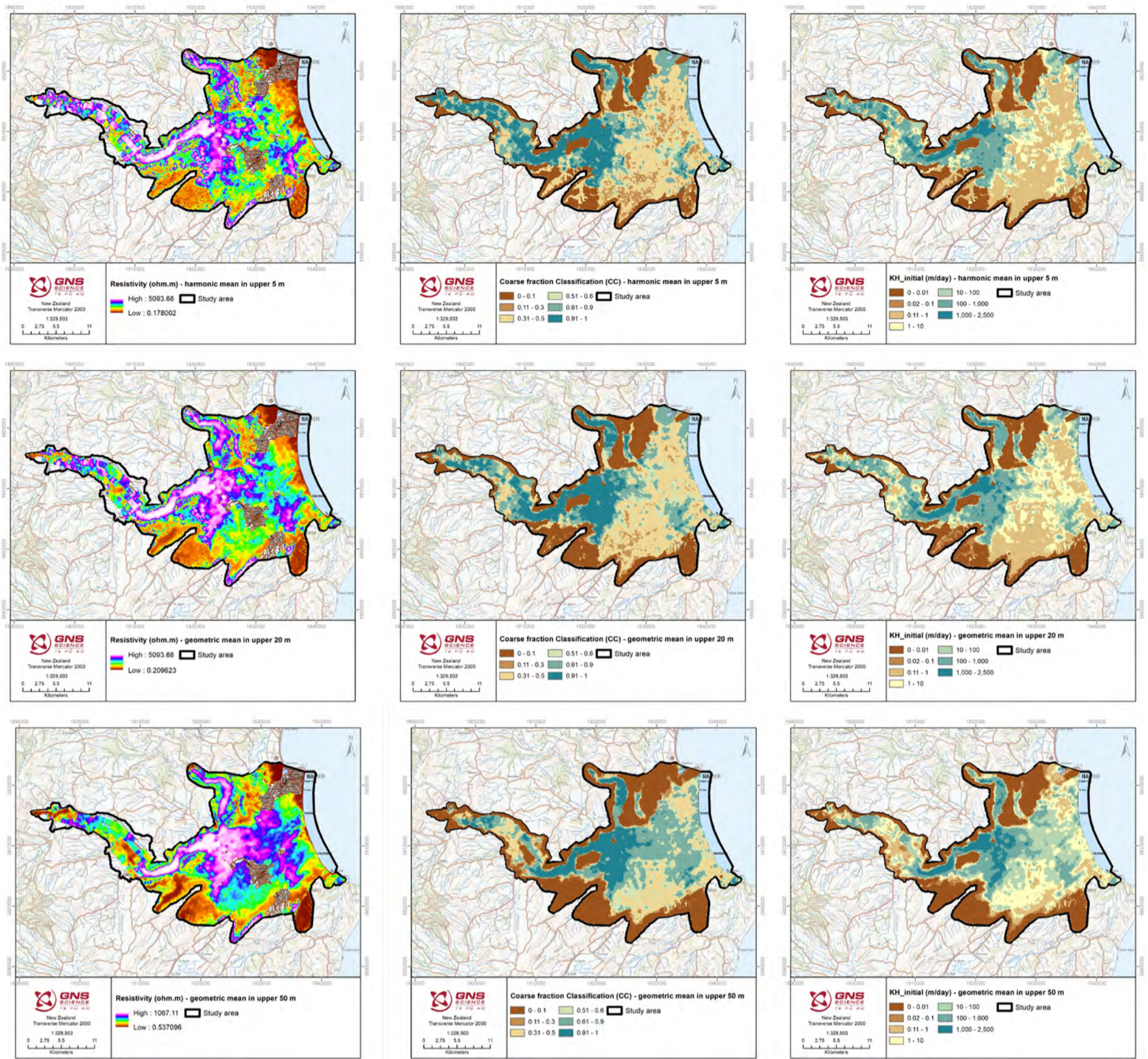
Figure 3.7 A selection of near-surface property estimates. (Left to right) resistivity (ohm.m), coarse-fraction classification and initial horizontal hydraulic conductivity (*KH_initial* [m/day]). (Top row) Harmonic mean of upper 5 m; (middle row) geometric mean of upper 20 m; (bottom row) geometric mean of upper 50 m.
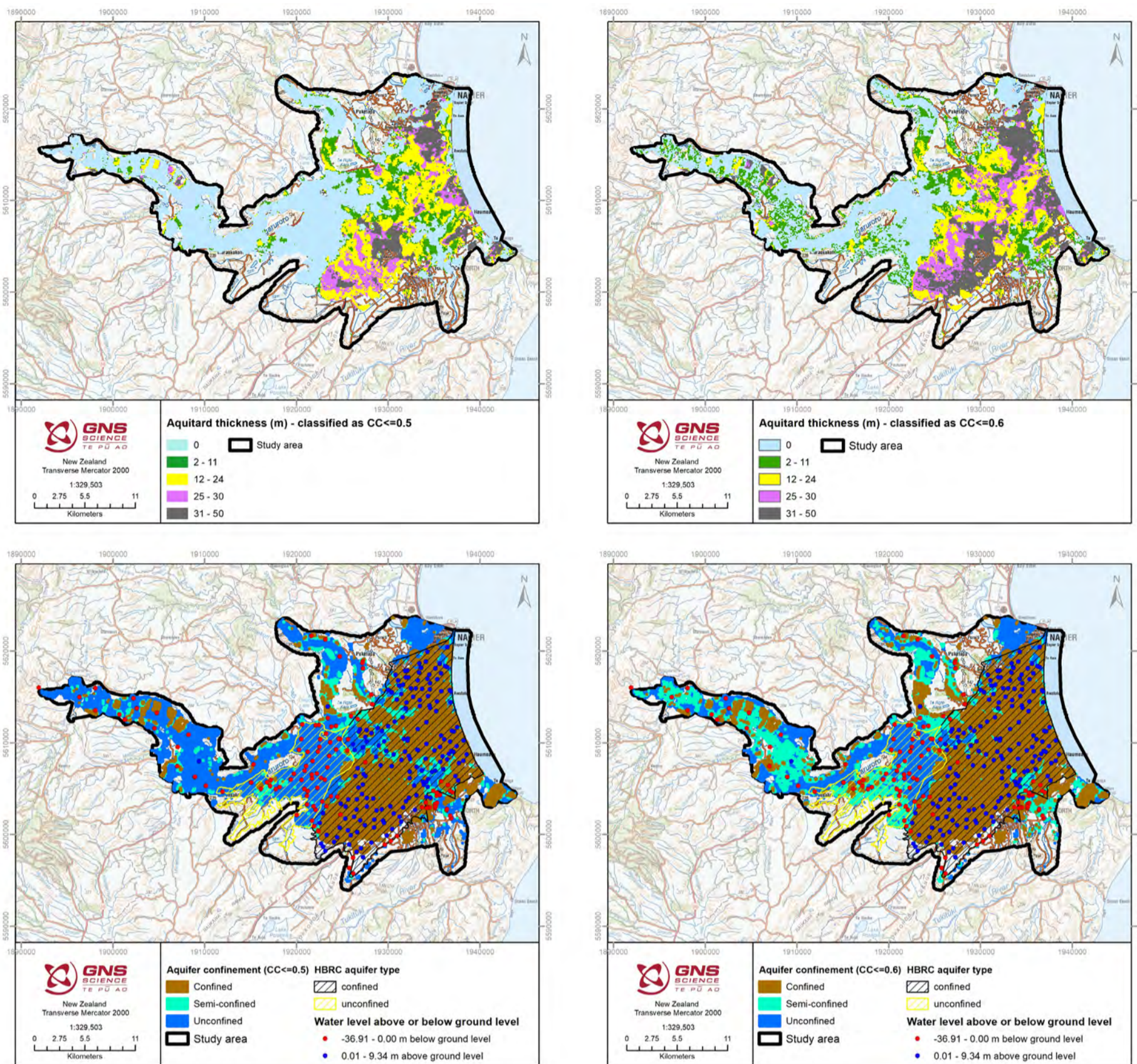
Figure 3.8 Aquitard thickness and confinement status in the upper 50 m. The maps derived through the aquitard definition of CC ≤0.6 (right) match the bores with artesian conditions (Tschritter et al. 2022); however, the maps derived through the aquitard definition of CC ≤0.5 (left) are considered best for any purposes related to drinking-water protection (see text for details). The translation from thickness to confinement requires assumptions of vertical hydraulic conductivity (0.05 m/day), hydraulic gradient (0.039) and effective porosity (0.06). See text for further details.
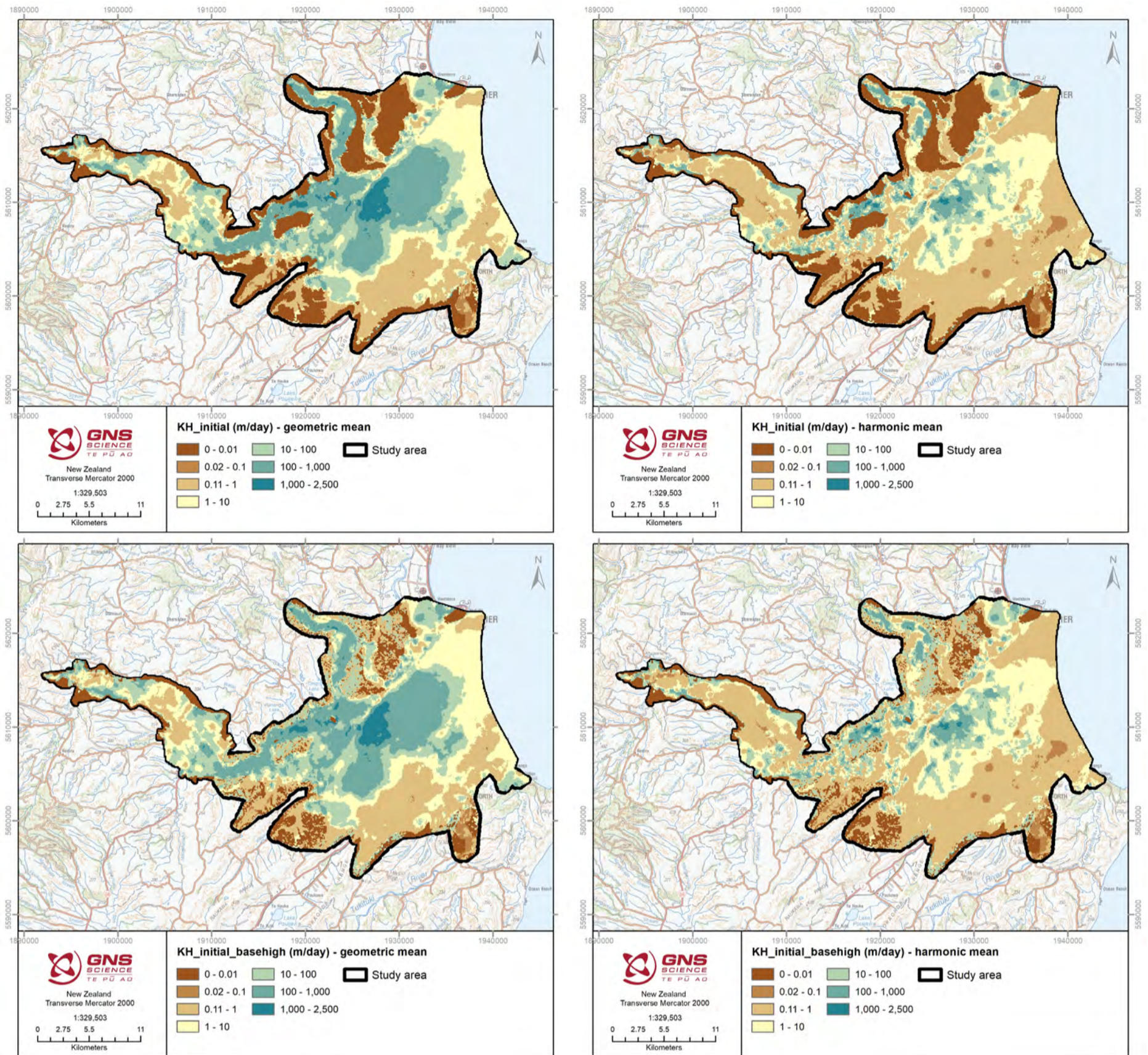
Figure 3.9 Geometric and harmonic mean of *KH_initial* and *KH_initial_basehigh*, calculated through each vertical 3D model column corresponding to unconsolidated and consolidated sediments where these are at the surface.

3.3   Comparison to Previous Investigations

The models and maps developed can assist with further hydrogeological understanding of the Heretaunga Plains aquifer system. Here, a few comparisons are made to previous studies.

The current HBRC aquifer confinement polygons are shown in Figure 3.8 for comparison to the newly derived aquifer confinement polygons. The two datasets largely agree for the CC ≤0.6 defined polygons, although the newly derived datasets highlight a further extent of unconfined conditions where the Tukituki River and Ngaruroro River enter the plains. Comparisons of aquitard thickness to similar maps from Dravid and Brown (1997) and Rakowski and Knowling (2018) are shown in Figure 3.10. There is no clear correspondence between the aquitard thickness maps and the areas of weak confining seal previously identified by Dravid and Brown (1997), and some of the contours are substantially different. For example, the central 35-m-thick contour from Dravid and Brown (1997) appears to have been interpolated across an area identified in this report as much thinner. The extents match well with Rakowski and Knowling (2018), and the difference between the two aquitard thickness maps highlights a strong match to a narrow band outside the flowing boundary that corresponds to thinner (12–24 m) material identified by the map that used CC ≤0.5 to identify aquitards. This supports the supposition that material with the medium permeability of CC = 0.5–0.6 has a character important for understanding small-scale flow patterns.

The CC and *KH_initial* models harmonic mean upper 5 m maps are useful for comparison to groundwater–surface water interactions studies (Figure 3.11). Wilding (2018) identified where the Ngaruroro River had major loss just before Fernhill and variable loss after Fernhill (Figure 3.12); in Figure 3.11, it can be seen that there is very high CC/*KH_initial* in the area of major loss and a significant reduction in CC/*KH_initial* where this loss is variable. Similarly, when compared with the Wilding (2018) map showing losing and gaining reaches throughout the plains (Figures 3.11 and 3.13), it can be seen that areas of loss correlate with areas of high CC/*KH_initial* in the upper 5 m.

The *KH_initial* and *KH_initial_basehigh* geometric and harmonic mean maps across all depths can be useful for comparisons to previous work looking at groundwater chemistry and age. Morgenstern et al. (2018) previously identified areas that appeared to have no flow connection based on age data, as well as flow pathways linked to river recharge or rain recharge (Figure 3.14). These areas are numbered on Figure 3.14 for further discussion, and groundwater sampling locations are also shown on the *KH_initial_basehigh* geometric mean maps for the upper 10 m and 50 m, shown in Figure 3.14. *KH_initial_basehigh* can also assist with considerations related to potential flow connections from consolidated sediments (e.g. Figure 3.14).

1. **Southwest of Roys Hill:** This bore, with a 30–50-year mean residence time (MRT), is 13 m deep. The near-surface KH maps for the upper 5 m, 20 m (Figure 3.7) and 10 m (Figure 3.14) highlight that this bore is situated on the northwest side of a low-permeability band of material (K_H = 0.1–10 m/day) that runs north to south between basement outcrops. However, maps of the upper 50 m (Figures 3.7 and 3.14) highlight that this permeability increases with depth (K_H = 10–100 m/day). This indicates that, although groundwater may be trapped or slow-moving and aging in the upper ~10–20 m where water was sampled, there may be a more permeable pathway beneath this, allowing some flow through from the Ngaruroro River to the Bridge Pa area. Additional drilling and sampling could help verify this, using these maps to assist with location targeting.

2. **North of Fernhill (Moteo Valley):** The bores with young water south of the identified blockage are both ~12 m deep, while the bore north of the identified blockage with old water identified is screened at 38 m depth. Similar to the above assessment, the near-surface property maps identify a region of low permeability (K_H = 0.1–10 m/day) at this location in the upper 5 m, 10 m and 20 m (Figures 3.7 and 3.14). This increases in the upper 50 m map (K_H = 10–100 m/day). This suggests that there may be some deeper flow paths beneath the boreholes sampled, allowing flow through this area. Additional drilling and sampling could help verify this, using these maps to assist with location targeting.

3. **Tutaekuri River at Waiohiki:** Low permeability (K_H = 0.02–10 m/day) is displayed in all maps through this area, supporting the no (or very limited) flow assessment of Morgenstern et al. (2018) (Figure 3.14).

4. **Tukituki River near Havelock North:** This is a question mark in Morgenstern et al. (2018) (Figure 3.14). All KH maps show an area southeast of Havelock North that is low permeability, with permeability increases occurring to the northeast of Havelock North – coincident with an area of river loss shown in Figure 3.13.

5. **Rain recharged pathways:** The KH upper 10 m map in Figure 3.14 shows two areas of higher-permeability material in the near-surface to the north and west of Hastings extending to the southeast. These locations appear to be coincident with the start of the rain-recharged pathways in Figure 3.14 and may result in higher concentrations of rain-recharged groundwater in these areas.

6. **River recharge pathways from the Ngaruroro River:** The KH maps (Figure 3.14) show the highest permeability material (K_H = 1000–2500 m/day) beneath the Ngaruroro River branching at Fernhill – coincident with the start of the two river-recharged pathways identified by Morgenstern et al. (2018) (Figure 3.14)

Overall, the maps and models developed provide useful information to improve understanding of the hydrogeological system in the Heretaunga Plains, support a greater understanding of other datasets (e.g. groundwater age and stream-flow gauging data) and could be used to guide additional data collection with greater precision.
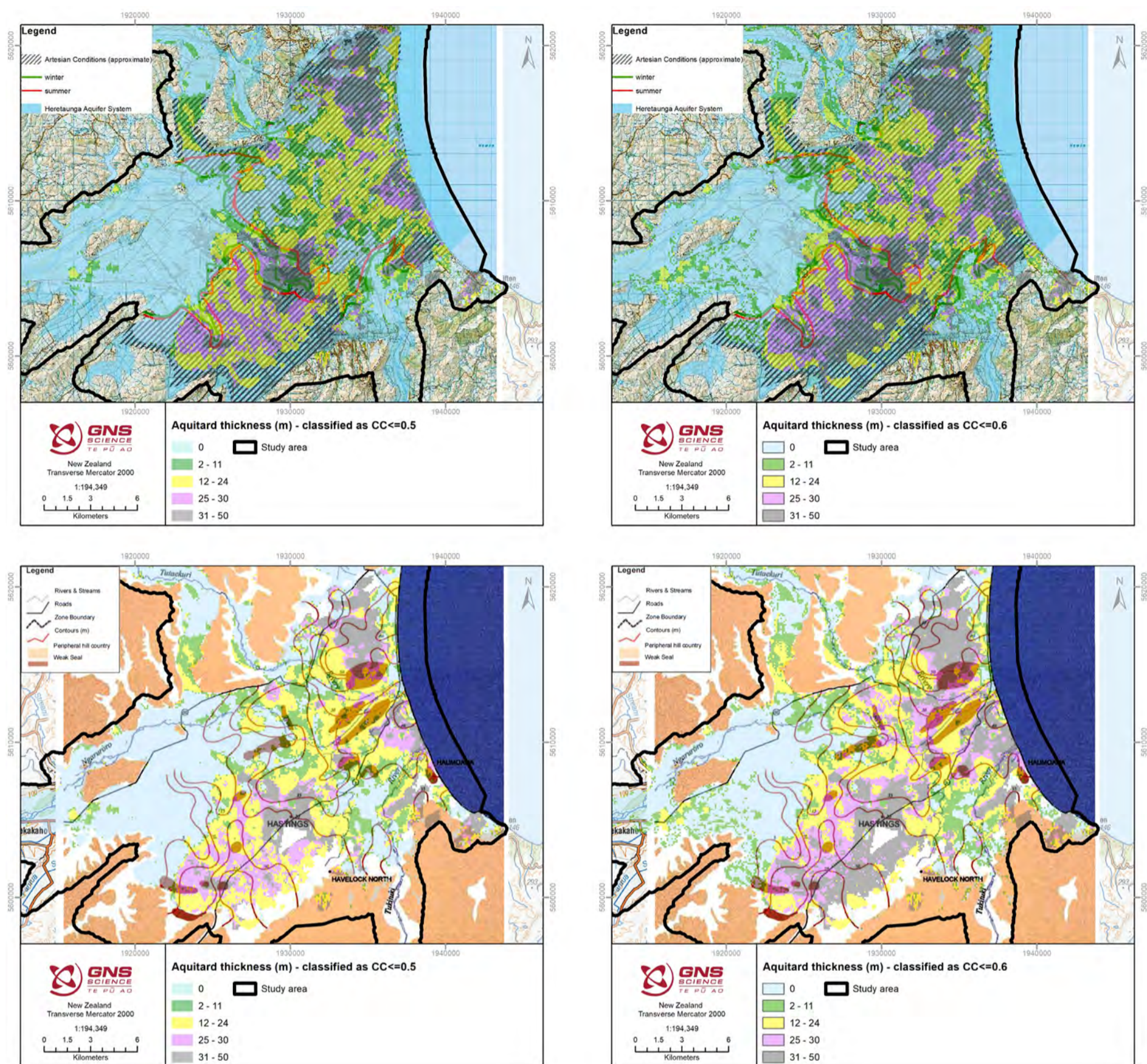
Figure 3.10 (Top) Comparison of aquitard thickness with flowing artesian conditions in the Heretaunga Aquifer in winter (green line) and summer (red line), from Rakowski and Knowling (2018) (figure from Rakowski and Knowling [2018] was georeferenced and placed underneath aquitard thickness maps defined in this work for comparison purposes). (Bottom) Comparison of aquifer thickness with contour map showing the thickness (m) and inland extent of the confining strata overlying the main aquifer system and the areas of weak confining seal (dark brown areas), from Dravid and Brown (1997) (figure from Dravid and Brown [1997] was georeferenced and placed underneath aquitard thickness maps defined in this work for comparison purposes).

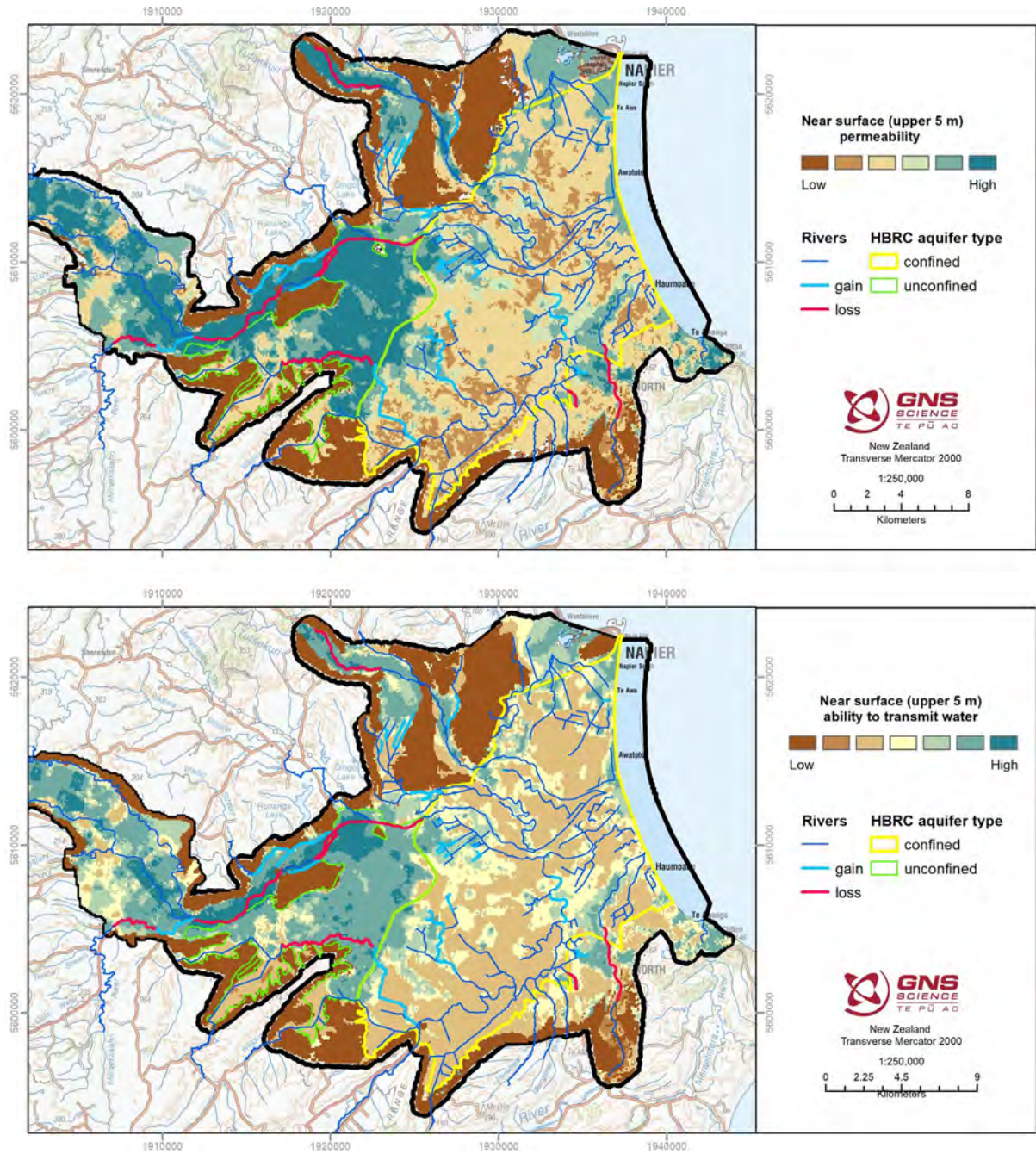This page left intentionally blank.

Figure 3.11   Harmonic mean of CC model (top) and *KH_initial* (bottom) in upper 5 m, with a comparison to river gain and loss locations interpreted from flow gaugings, as well as the existing confined and unconfined HBRC polygons.
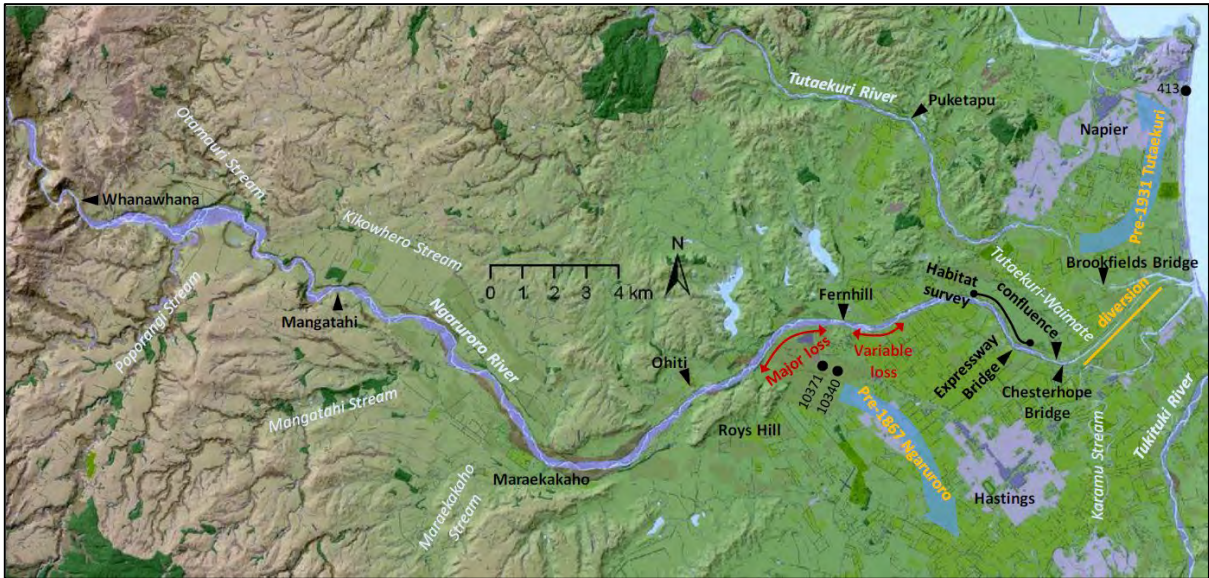
Figure 3.12   Map showing losing reaches and diversions of the Ngaruroro River, as well as historical river flow pathways of the Ngaruroro and Tutaekuri rivers. Figure from Wilding (2018).
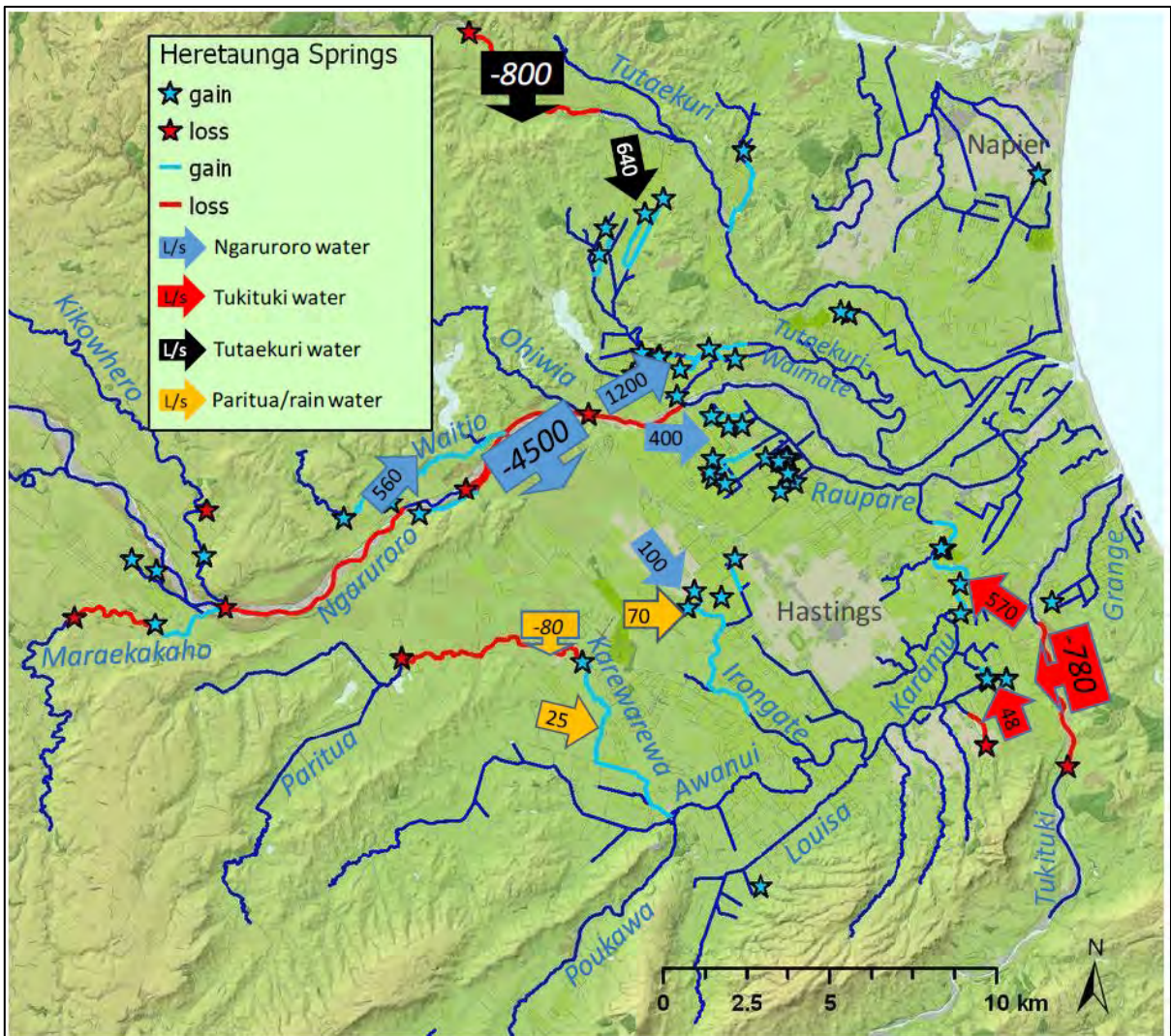

Figure 3.13   Figure from Wilding (2018) showing the losing (red lines) and gaining reaches (blue lines) of rivers and streams, as well as springs in the Heretaunga Plains. Arrows represent the amount of flow gain (positive numbers) or loss (negative numbers) and are coloured by source. The flow losses and gains are shown as static estimates at mean annual low flow.
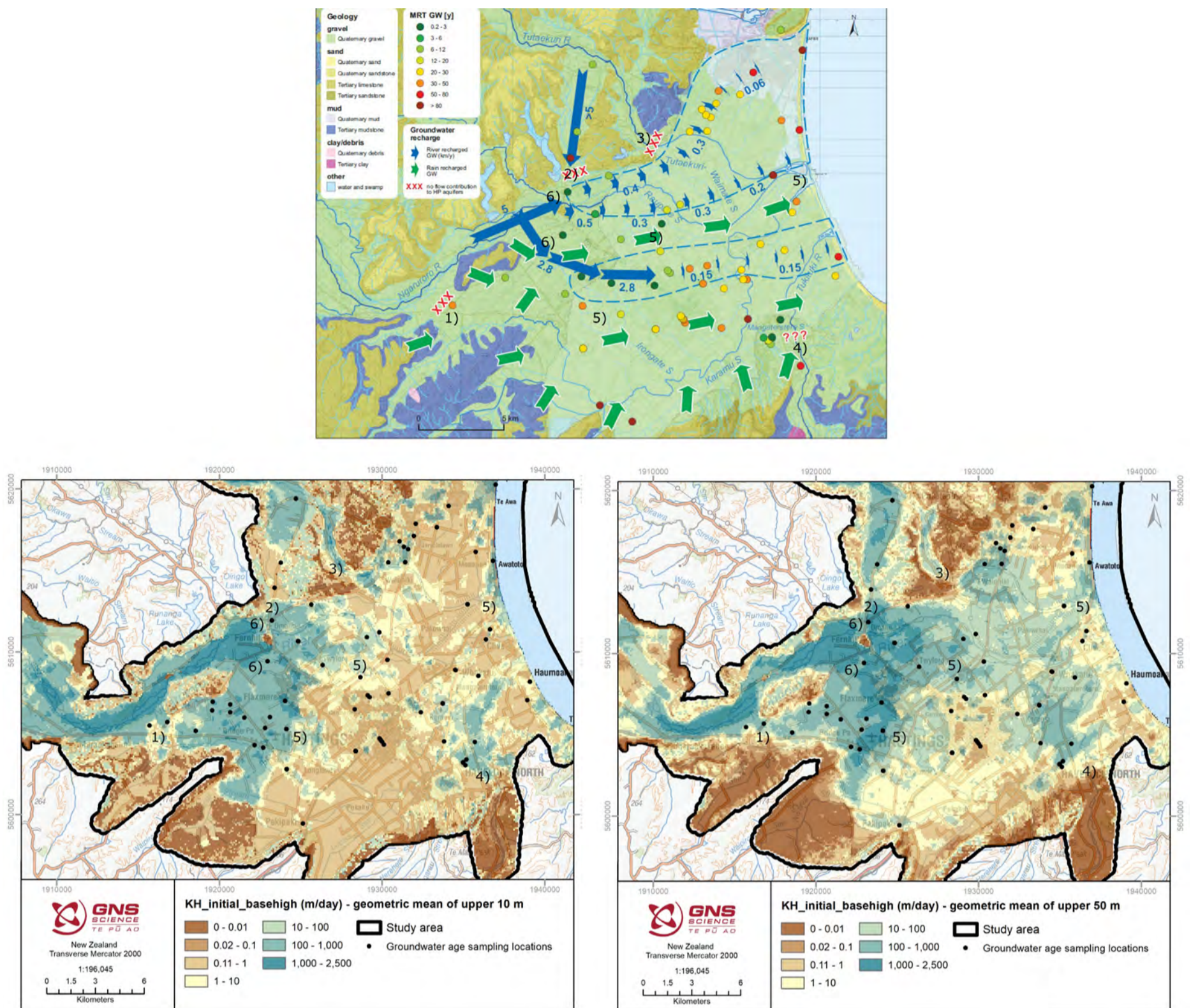
Figure 3.14   (Top) Groundwater age (mean residence time [MRT]) and water dynamics in the Heretaunga Plains hydrologic system inferred from groundwater ages (figure modified from Morgenstern et al. [2018]). The labels 1–6 identify locations discussed in the text. From the Morgenstern et al. (2018) interpretation: the two areas indicated by blue dotted lines are the areas of clear Ngaruroro River recharge signature; the length of the arrows is proportional to the groundwater flow velocity (numbers in km/year). (Bottom) Geometric mean of *KH_initial_basehigh*, calculated for (left) the upper 10 m and (right) the upper 50 m. A zoomed-in view and comparison to groundwater age sampling locations are provided for comparison.

This page left intentionally blank.

4.0   DIGITAL DELIVERABLES

All digital maps and data are geo-referenced to coordinate system New Zealand Transverse Mercator (NZTM 2000) and New Zealand Vertical Datum 2020 (NZVD2016).

4.1   3D-Gridded Products

A *.csv* file with all 3D models (see Table 3.1):

- *3D\Heretaunga_SkyTEM_3Dmodels_V1_2023.csv*

Multi-band raster files for a selection of the 3D models, for numerical groundwater modelling and viewing in GIS. Each multi-band raster contains 441 bands in elevation order, where Band 1 = 286 mASL and Band 441 = -594 mASL, with each band consisting of a 2-m-thick vertical slice referenced to the cell centre. This elevation data is included within the metadata of the files:

- *3D\Heretaunga_SkyTEM_res_V1_2023.tif*
- *3D\Heretaunga_SkyTEM_resvar_V1_2023.tif*
- *3D\Heretaunga_SkyTEM_HU_V1_2023.tif*
- *3D\Heretaunga_SkyTEM_HS_V1_2023.tif*
- *3D\Heretaunga_SkyTEM_AP_V1_2023.tif*
- *3D\Heretaunga_SkyTEM_CC_V1_2023.tif*
- *3D\Heretaunga_SkyTEM_facies_V1_2023.tif*
- *3D\Heretaunga_SkyTEM_KH_initial_V1_2023.tif*
- *3D\Heretaunga_SkyTEM_KH_initial_basehigh_V1_2023.tif*
- *3D\Heretaunga_SkyTEM_KH_initial_base1_V1_2023.tif*
- *3D\Heretaunga_SkyTEM_KH_unc_V1_2023.tif*

4.2   2D Maps

Two-dimensional map products provided in raster and GIS polygon formats.

Model areas:
- *2D\Heretaunga_SkyTEM_modelarea.shp*
- *2D\Heretaunga_SkyTEM_modelarea_onshore.shp*

Saline influence in the near-surface:
- *2D\Heretaunga_SkyTEM_salineupper30m_facies1-4coastal.shp*
- *2D\Heretaunga_SkyTEM_salineupper30m_facies1-4coastal_extent.shp*
- *2D\Heretaunga_SkyTEM_salineupper30m_facies1coastal.shp*

Aquifer thickness:

- *2D\Heretaunga_SkyTEM_aquiferthickness_V1_2023.tif*
- *2D\Heretaunga_SkyTEM_aquiferthickness_V1_2023.shp*
- *2D\Heretaunga_SkyTEM_aquiferextent_V1_2023.shp*
- *2D\Heretaunga_SkyTEM_surficialaquiferthickness_V1_2023.tif*
- *2D\Heretaunga_SkyTEM_aquiferthickness%_V1_2023.tif*
- *2D\Heretaunga_SkyTEM_deepaquiferthickness_V1_2023.tif*

Near-surface properties – '*' corresponds to one of *res*, *resvar*, *CC*, *KH_initial*, *KH_initial_basehigh* or *KH_initial_base1*, and values are provided for both the harmonic mean (*hmean*) and the geometric mean (*gmean*):

- *2D\Heretaunga_SkyTEM_upper5m_hmean_*_V1_2023.tif*
- *2D\Heretaunga_SkyTEM_upper10m_hmean _*_V1_2023.tif*
- *2D\Heretaunga_SkyTEM_upper15m_hmean _*_V1_2023.tif*
- *2D\Heretaunga_SkyTEM_upper20m_hmean _*_V1_2023.tif*
- *2D\Heretaunga_SkyTEM_upper30m_hmean _*_V1_2023.tif*
- *2D\Heretaunga_SkyTEM_upper50m_hmean _*_V1_2023.tif*

Aquifer near-surface vulnerability and confinement:

- *2D\Heretaunga_SkyTEM_aquitardthickness_CC0.5_V1_2023.tif*
- *2D\Heretaunga_SkyTEM_aquitardthickness_CC0.5_V1_2023.shp*
- *2D\Heretaunga_SkyTEM_aquitardthickness_CC0.6_V1_2023.tif*
- *2D\Heretaunga_SkyTEM_aquitardthickness_CC0.6_V1_2023.shp*
- *2D\Heretaunga_SkyTEM_aquiferconfinement_CC0.5_V1_2023.shp*
- *2D\Heretaunga_SkyTEM_aquiferconfinement_CC0.6_V1_2023.shp*

Geometric mean and harmonic mean of horizontal hydraulic conductivity models – '*' corresponds to one of *KH_initial*, *KH_initial_basehigh* or *KH_initial_base1*:

- *2D\Heretaunga_SkyTEM_*_gmean_V1_2023.tif*
- *2D\Heretaunga_SkyTEM_*_hmean_V1_2023.tif*

4.3   Supporting Datasets

A 25 m DEM used for 3D model clipping at the land surface (Sahoo et al. 2023):

- *Supporting\HeretaungaSkyTEM_DEM_25m.asc*

A Leapfrog viewer file containing the DEM, lithological logs and a selection of the 3D models as block models:

- *Supporting\HeretaungaSkyTEM_LeapfrogViewer.lfview*

A corrected hydraulic conductivity dataset utilised for the assessment in Section 2.1.7.

- *Supporting\Heretaunga_SkyTEM_aquifertests_KH.csv*

A colour reference file for webmap display:

- *Supporting\Heretaunga_webmap_colours.csv*

500 hydrostratigraphic realisations (Foged 2022; Section 2.1.3; '*' = 000–499) as multi-band raster files:

- *Supporting\Foged2022_HSrealisations_rasters\Run07_real00*.tif*

The percentage of the 500 realisations for each cluster 0–4 within every model cell (original model grid used for the 500 hydrostratigraphic realisations) (see Section 2.1.8 and Foged [2022]):

- *Supporting\Heretaunga_clusterpercentages_500realisations.csv*

The point datasets underlying the 500 hydrostratigraphic realisations at the SkyTEM data locations (see Section 2.1.8 and Foged [2022]):

- *Supporting\Heretaunga_CF_cluster_SI_raw.csv*

5.0 CONCLUSIONS AND RECOMMENDATIONS

3D model datasets were combined within a .csv file, with x,y,z defining the centre of each grid cell and including the following parameters: *X, Y, Z, top_elev_HU, res*, *resvar*, *HU*, *HS_unclipped*, *HS*, *facies*, *AP*, *aq*, *CC*, *K_res*, *K_CC*, *K_min*, *KH_initial*, *KH_initial_basehigh*, *KH_initial_base1*, *KH_unc*. A selection of these models was converted to multi-band raster format for easy utilisation by numerical groundwater modelling. The 3D models utilise 100 x 100 m grid cells horizontally and 2-m-thick grid cells vertically.

The res and CC models were utilised to provide estimates of K_H. It is important to consider upscaling impacts on K_H and, as such, the best initial values of K_H to use may differ depending on the groundwater model construction. Sufficient datasets have been provided such that the relationship of K_H to the models could be assessed as part of numerical modelling construction, initial prior simulation runs and calibration. As the CC model has near-complete data coverage (includes basement and fills resistivity data gaps) and has been shown to provide a good fit to lab-based grain-size analyses, as well as providing meaningful comparisons to pore-water electrical conductivity and lithological logs, it was selected for deriving 2D maps assessing aquifer and aquitard thicknesses.

Simplifications of the 3D models to 2D maps assisted with more readily investigating various aspects of the Heretaunga Plains aquifer system, and comparisons to previous investigations highlighted the benefits of these datasets. Overall, the maps and models developed provide useful information to improve the understanding of the hydrogeological system in the Heretaunga Plains, support a greater understanding of other datasets and could be used to guide additional data collection with greater precision.

Model formats and types were developed following discussions with numerical groundwater modellers undertaking the next phase of work as to the most useful datasets to refine numerical groundwater models. The next phase of work in 3DAMP will undertake experiments that aim to explore methods for utilisation of SkyTEM data to refine numerical groundwater models and consequences for predictive uncertainty.

Section 2.1.6 compared grain-size analyses made using lab-based equipment, by a geologist on hand samples and by a geologist on lithological log descriptions. Although information for this comparison was only available for a single borehole, the information suggests that the estimates made on lithological log descriptions alone tended to under-estimate the amount of coarse material by approximately 30% within an interval where this coarse material amount was less than 60%. The estimates on the hand samples performed well compared to the lab-based estimates. To provide higher-quality lithological log information in the future without the additional costs of lab-based estimates, geologists could make grain-size estimates on hand samples and provide this information along with the lithological logs. If this information is separated into an additional data attribute and included within a borehole database in a consistent format, it could improve reliability of utilising these data in the future and support greater reliability of information supporting numerical groundwater model developments. The CC model had good agreement with the lab-based grain-size measurements. To further test these comparisons, there is more grain-size information in the Ruataniwha area that can be analysed as part of a subsequent 3DAMP interpretation report.

New data in the future that could be used to refine these models include:

- New resistivity data, for example, from ground-based surveys, could be used to fill gaps within the interpolated resistivity model, which could subsequently result in different interpretive models.

- New borehole data could be used to revise the HU, HS and CC models.

- New grain-size analyses could be used to further validate the HS and CC models.

- Further information on hydraulic properties and grain size could be used to refine the K_H models.

- Further field or lab measurements of effective porosity, vertical hydraulic conductivity and hydraulic gradients could refine one-year travel-time estimates and so further inform considerations of aquifer vulnerability.

- Numerical modelling could be utilised to refine aquifer confinement and aquifer vulnerability estimates.

- All of the above could be used to refine the 2D map products.

It is not considered of significant value to revise models on the arrival of a small amount of additional data; however, it should be considered if any significant data collection campaigns are undertaken. Without significant data collection campaigns, possibly a 10-year review would be a suitable time horizon for sufficient additional data to have been collected for there to be value in reviewing and revising models. Additional information that would be of value to improving the quality of modelling includes GPS-located borehole information with high-quality lithological logs and screen location information.

Local studies could refine models through closer interrogation and refinement of datasets for specific local applications.

6.0   ACKNOWLEDGEMENTS

7.0   REFERENCES

Bouwer H, Rice RC. 1976. A slug test for determining hydraulic conductivity of unconfined aquifers with completely or partially penetrating wells. *Water Resources Research*. 12(3):423–428. https://doi.org/10.1029/WR012i003p00423

Dravid PND, Brown LJ. 1997. Heretaunga Plains groundwater study. Napier (NZ): Hawke's Bay Regional Council. 3 vol.

Duque C, Meyer R, Sonnenborg TO. 2022. Saltwater intrusion in Denmark. *Boletín Geológico y Minero*. 133(1):29–46. https://doi.org/10.21701/bolgeomin/133.1/002

Faunt CC, editor. 2009. Groundwater availability of the Central Valley Aquifer, California. Reston (VA): U.S. Geological Survey. 225 p. Professional Paper 1766.

Foged N. 2022. Hawke's Bay 3D Aquifer Mapping Project: Heretaunga Plains, 3D hydrostratigraphic modelling. Aarhus (DK): Aarhus University HydroGeophysics Group. 27 p. Prepared for Hawke's Bay Regional Council.

Freeze RA, Cherry JA. 1979. Groundwater. Englewood Cliffs (NJ): Prentice-Hall. 604 p.

Good Earth Matters. 2019. Drinking water source water protection: proposed regulatory provisions for TANK catchments. [Wairoa] (NZ): Good Earth Matters Consulting Ltd. 65 p. + appendices. Prepared for Havelock North Joint Working Group on Drinking Water Safety (as a Working Committee of TANK).

Hansen B, Sonnenborg TO, Møller I, Bernth JD, Høyer A-S, Rasmussen P, Sandersen PBE, Jørgensen F. 2016. Nitrate vulnerability assessment of aquifers. *Environmental Earth Sciences*. 75(12):999. https://doi.org/10.1007/s12665-016-5767-2

[HBRC] Hawke's Bay Regional Council. 2006. Hawke's Bay Regional Resource Management Plan (includes Regional Policy Statement). Napier (NZ): Hawke's Bay Regional Council; [updated 2021 Dec 18; accessed 2023 Jul]. https://www.hbrc.govt.nz/our-documents/rrmp/

Heath RC. 1983. Basic ground-water hydrology. Reston (VA): U.S. Geological Survey. 86 p. Water-Supply Paper 2220.

Hemmings B. 2023. Personal communication. Senior Scientist, Groundwater Modelling; GNS Science, Wairakei, NZ.

Kellett RL, Rawlinson ZJ, Griffin AG, Lawrence MJF, Tschritter C, Sahoo TR, Herpe, M. 2022. Hawke's Bay 3D Aquifer Mapping Project: deep borehole interpretation within Heretaunga Plains in the context of SkyTEM data and new Borehole 17137 (3DAMP_Well2). Lower Hutt (NZ): GNS Science. 44 p. Consultancy Report 2022/90. Prepared for Hawke's Bay Regional Council.

Kosinski WK, Kelly WE. 1981. Geoelectric soundings for predicting aquifer properties. *Groundwater*. 19(2):163–171. https://doi.org/10.1111/j.1745-6584.1981.tb03455.x

Lawrence MJF, Kellett RL, Pradel GJ, Sanders F, Herpe M, Rawlinson ZJ, Reeves RR, Brakenrig T, Moreau M, Cameron SG, et al. 2021. Hawke's Bay 3D Aquifer Mapping Project: drilling completion report for Borehole 17137 (3DAMP_Well2), Morley Road, Heretaunga Plains. Lower Hutt (NZ): GNS Science. 90 p. Consultancy Report 2021/40. Prepared for Hawke's Bay Regional Council.

Lawrence MJF, Herpe M, Kellett RL, Pradel GJ, Sanders F, Coup L, Rawlinson ZJ, Reeves RR, Brakenrig T, Cameron SG, et al. 2022a. Hawke's Bay 3D Aquifer Mapping Project: drilling completion report for borehole 17136 (3DAMP_Well1), Ongaonga–Waipukurau Road, Ruataniwha Plains. Lower Hutt (NZ): GNS Science. 156 p. Consultancy Report 2022/31. Prepared for Hawke's Bay Regional Council.

Lawrence MJF, Herpe M, Pradel GJ, Kellett RL, Coup L, Sanders F, Rawlinson ZJ, Reeves RR, Brakenrig T, Cameron SG, et al. 2022b. Hawke's Bay 3D Aquifer Mapping Project: drilling completion report for borehole 17164 (3DAMP_Well3), Burnside Road, Ruataniwha Plains. Lower Hutt (NZ): GNS Science. 76 p. Consultancy Report 2022/15. Prepared for Hawke's Bay Regional Council.

Lee JM, Begg JG, Bland KJ. 2020. Geological map of the Napier-Hastings urban area. Lower Hutt (NZ): GNS Science. 1 map, scale 1:75,000. (GNS Science geological map; 7a).

Lough H, Clemens H, Love M. 2018. Technical guidelines for drinking water source protection zones. Christchurch (NZ): Pattle Delamore Partners. 41 p. + appendices. Prepared for the Ministry for the Environment.

Madarasz-Smith A, Wade O, Wade H, Hicks A. 2016. The estuaries of the TANK catchments: Ahuriri and Waitangi estuaries, values, state and trends. Napier (NZ): Hawke's Bay Regional Council. 118 p. HBRC Report RM 16-20.

Maneewongvatana S, Mount DM. 2002. Analysis of approximate nearest neighbor searching with clustered point sets. In: Goldwasser MH, Johnson DS, McGeoch CG, editors. *Data structures, near neighbor searches, and methodology: fifth and sixth DIMACS implementation challenges*. Providence (RI): American Mathematical Society. (DIMACS series in discrete mathematics and theoretical computer science; 59). p. 105–124.

Meilhac C, Reeves RR, Zemansky GM, White PA, Jebbour N. 2009. Field investigation of groundwater-surface water interactions, Ruataniwha Plains. Lower Hutt (NZ): GNS Science. 127 p. (GNS Science report; 2009/23).

Mele M, Bersezio R, Giudici M. 2012. Hydrogeophysical imaging of alluvial aquifers: electrostratigraphic units in the quaternary Po alluvial plain (Italy). *International Journal of Earth Sciences*. 101(7):2005–2025. https://doi.org/10.1007/s00531-012-0754-7

Minsley BJ, Rigby JR, James SR, Burton BL, Knierim KJ, Pace MDM, Bedrosian PA, Kress WH. 2021. Airborne geophysical surveys of the lower Mississippi Valley demonstrate system-scale mapping of subsurface architecture. *Communications Earth & Environment*. 2:article 131. https://doi.org/10.1038/s43247-021-00200-z

Moore C. 2023. Personal communication. Principal Scientist, Groundwater Modelling; GNS Science, Lower Hutt, NZ.

Moreau M, Nokes C, Cameron SG, Hadfield J, Gusyev MA, Tschritter C, Daughney CJ. 2014. Capture zone guidelines for New Zealand. Lower Hutt (NZ): GNS Science. 47 p. (GNS Science report; 2013/56).

Morgenstern U, Begg JG, van der Raaij RW, Moreau M, Martindale H, Daughney CJ, Franzblau RE, Stewart MK, Knowling MJ, Toews MW, et al. 2018. Heretaunga Plains aquifers: groundwater dynamics, source and hydrochemical processes as inferred from age, chemistry, and stable isotope tracer data. Lower Hutt (NZ): GNS Science. 82 p. (GNS Science report; 2017/33).

Niwas S, Celik M. 2012. Equation estimation of porosity and hydraulic conductivity of Ruhrtal aquifer in Germany using near surface geophysics. *Journal of Applied Geophysics*. 84:77–85. https://doi.org/10.1016/j.jappgeo.2012.06.001

Perwick A, Woodhouse C. 2014. Heretaunga Plains transmissivity and storativity maps. Christchurch (NZ): Pattle Delamore Partners Ltd. 25 p. + appendices. Report RM16-25. Prepared for Hawke's Bay Regional Council.

Ponzini G, Ostroman A, Molinari M. 1984. Empirical relation between electrical transverse resistance and hydraulic transmissivity. *Geoexploration*. 22(1):1–15. https://doi.org/10.1016/0016-7142(84)90002-4

Purvance DT, Andricevic R. 2000. On the electrical-hydraulic conductivity correlation in aquifers. *Water Resources Research*. 36(10):2905–2913. https://doi.org/10.1029/2000WR900165

Rakowski P, Knowling MJ. 2018. Heretaunga aquifer groundwater model: development report. Napier (NZ): Hawke's Bay Regional Council. 182 p. HRBC Report RM18-14.

Rawlinson ZJ, Foged N, Westerhoff RS, Kellett RL. 2021. Hawke's Bay 3D Aquifer Mapping Project: Heretaunga Plains SkyTEM data processing and resistivity models. Wairakei (NZ): GNS Science. 90 p. Consultancy Report 2021/93. Prepared for Hawke's Bay Regional Council.

Rawlinson ZJ, Sahoo TR, Kellett RL, Cameron SG. In prep. Hawke's Bay 3D Aquifer Mapping Project: hydrogeological interpretation of the SkyTEM-derived resistivity models within the Poukawa and Otane basins. Wairakei (NZ): GNS Science. Consultancy Report 2021/12. Prepared for Hawke's Bay Regional Council.

Sahoo TR, Rawlinson ZJ, Kellett RL. 2023. Hawke's Bay 3D Aquifer Mapping Project: delineation of major hydrological units within the Heretaunga Plains from SkyTEM-derived resistivity models. Lower Hutt (NZ): GNS Science. 55 p. Consultancy Report 2022/30. Prepared for Hawke's Bay Regional Council.

SkyTEM Australia Pty Ltd. [2020]. Acquisition and processing report: SkyTEM helicopter EM survey, Hawkes Bay, NZ. Malaga (AU): SkyTEM Australia Pty Ltd. 33 p. Report AUS 10056. Prepared for Hawke's Bay Regional Council.

Slater L. 2007. Near surface electrical characterization of hydraulic conductivity: from petrophysical properties to aquifer geometries – a review. *Surveys in Geophysics*. 28:169–197. https://doi.org/10.1007/s10712-007-9022-y

Tonkin & Taylor. 2016. Bacterial contamination investigation. [Place unknown] (NZ): Tonkin & Taylor Ltd. Job 31301.100. Prepared for Hastings District Council.

Tonkin & Taylor. 2018. Source protection zones for public supply bores: Hastings urban area. [Napier] (NZ): Tonkin & Taylor Ltd. 65 p. Report 1005769. Prepared for Hastings District Council.

Tschritter C, Kellett RL, Rawlinson ZJ, Griffin AG. 2022. Hawke's Bay 3D Aquifer Mapping Project: Heretaunga Plains data and model inventory. Wairakei (NZ): GNS Science. 96 p. Consultancy Report 2021/113. Prepared for Hawke's Bay Regional Council.

Urish DW. 1981. Electrical resistivity – hydraulic conductivity relationships in glacial outwash aquifers. *Water Resources Research*. 17(5):1401–1408. https://doi.org/10.1029/WR017i005p01401

Virtanen P, Gommers R, Oliphant TE, Haberland M, Reddy T, Cournapeau D, Burovski E, Peterson P, Weckesser W, Bright J, et al. 2020. SciPy 1.0: fundamental algorithms for scientific computing in Python. *Nature Methods*. 17(3):261–272. https://doi.org/10.1038/s41592-019-0686-2

Wilding T. 2018. Heretaunga Springs: gains and losses of stream flow to groundwater on the Heretaunga Plains. Napier (NZ): Hawke's Bay Regional Council. HBRC Report RM18-13 – 4996.

Wilson SR, Ingham M, McConchie JA. 2006. The applicability of earth resistivity methods for saline interface definition. *Journal of Hydrology*. 316(1):301–312. https://doi.org/10.1016/j.jhydrol.2005.05.004